New Physics Undercover at the LHC

Hou Keong Lou

A Dissertation
Presented to the Faculty
of Princeton University
in Candidacy for the Degree
of Doctor of Philosophy

Recommended for Acceptance
by the Department of
Physics

Advisors: Nima Arkani-Hamed, Mariangela Lisanti

September, 2015

Abstract

With the completion of 7 TeV and 8 TeV data taking at the Large Hadron Collider (LHC), the physics community witnessed one of the great triumphs of modern physics: the completion of the Standard Model (SM) as an effective theory. The final missing particle, the Higgs boson, was observed and its mass was measured. However, many theoretical questions remain unanswered. What is the source of electroweak symmetry breaking? What is the nature of dark matter? How does gravity fit into the picture? With no definitive hints of new physics at the LHC, we must consider the possibility that our search strategies need to be expanded. Conventional LHC searches focus on theoretically motivated scenarios, such as the Minimal Supersymmetric Standard Models and Little Higgs Theories. However, it is possible that new physics may be entirely different from what we might expect. In this thesis, we examine a variety of scenarios that lead to new physics undercover at the LHC. First we look at potential new physics hiding in Quantum Chromo-Dynamics backgrounds, which may be uncovered using jet substructure techniques in a data-driven way. Then we turn to new long-lived particles hiding in Higgs decay, which may lead to displaced vertices. Such a signal can be unearthed through a data-driven analysis. Then we turn to new physics with "semi-visible jets", which lead to missing momentum aligned with jet momentum. These events are vetoed in traditional searches and we demonstrate ways to uncover these signals. Lastly, we explore performance of future colliders in two case studies: Stops and Higgs Portal searches. We show that a 100 TeV collider will lead to significant improvements over 14 TeV LHC runs. Indeed, new physics may lie undercover at the LHC and future colliders, waiting to be discovered.

Acknowledgements

I am very thankful to have been given the opportunitity to be part of the Princeton graduate physics program. There are numerous people who have helped me along the way. First and foremost, I would like to thank my advisors, Mariangela Lisanti and Nima Arkani-Hamed. Mariangela has provided me guidance throughout my graduate career and also helped me form many fruitful collaborations. She helped me get started on my first paper, and many projects have followed since. She also gave me many insights in academia and kept me moving forward when I hit road-blocks and errors. Meanwhile, Nima provided me much inspiration for studying fundamental physics and showed me the proper ways to think about many physics problems. He gave me a lot of useful advice in academia and helped me through my application process. Both of my advisors helped foster a vibrant phenomenology community here at Princeton, from which I have benefited greatly.

Secondly I would like to thank all the friends, colleagues and collaborators who helped and taught me a great deal over the years. I am especially grateful to Tim Cohen, who worked with me on numerous projects. He taught me many collider physics insights and tools of the trade. He helped me become a more confident and independent researcher, and showed me how to ask the right questions. I want to thank Nathaniel Craig, who worked with me on several theoretical projects, and stayed patient when I got stuck on calculations. I am also thankful to Herman Verlinde, who was my first advisor. Despite the fact that I did not end up doing research in formal theory, I had many valuable dicussions with Herman. I also thank Valerie Halyo, who helped me with my experimental projects and taught me many things about the CMS experiment. I want to thank Pratima Jindal,

Paul Lujan and Jeremy Werner, who also helped me with my experimental projects and early work on the CMS experiment. I am grateful to have the opportunity to work with my other collaborators, including Raffaele Tito D'Agnolo, Mike Hance, Eder Izaguirre, Martin Jankowiak, Matthew McCullough, David Pinner, Arun Thalapillil, and Jay Wacker; it was a pleasure working with all of them.

I also want to thank my colleague, Michael Park, whom I have known since my undergraduate years. He was patient enough to listen to my crackpot ideas and keep me sane when I needed someone to discuss phenomenology with. I also want to thank Simon Knapen, with whom I had many fun and useful physics discussions. I also want to thank all my friends and colleagues at Princeton, including Aris Alexandradinata, Farzan Beroz, Phil Hebda, Andras Gyenis, Matt Hernandez, Vedika Khemani, Jeffrey Nguyen and my academic brother Siddharth Mishra Sharma and many others for keeping Princeton an interesting and enjoyable place.

Lastly I want to thank my other friends and family members. I am grateful to Yifan Lin, Pawan Harvu, Gautam Jain and all my friends for their years of support since I was an undergraduate. I am especially indebted to Talia Waltzer, the love of my life, for always supporting me and keeping me company regardless of what mood I am in. Despite how unpleasant I might be, she continues to take care of me and is always a great listener. I am very thankful to the wonderful family I have. My two great sisters were always supportive and have taken care of me as their little brother all these years. Finally, I am forever grateful to my parents, who never had the chance for higher education. Through all these years, they have worked relentlessly so that my family could move to the US and I could have the chance to pursue my dreams. They have worked many long hours to raise a family of three in difficult economic times and have never asked for anything in return. The many research difficulties and challenges in academia seem to pale in comparison. I am dedicating this thesis to my parents, fulfilling the dreams they could never afford to have.

Dedicated to my parents, Lam Seng and Lu Ming Jian

Contents

Part I

Introduction

Fundamental physics saw great advances in the 20th century. By combining quantum mechanics with special relativity, physicists came up with a unifying description of the electroweak and the strong forces and their interactions with matter. All the fundamental particles are organized into quantum fields, and their allowed interactions are summarized into a single Lagrangian. This description of nature is now known as the Standard Model (SM), which has been verified to an astonishing degree of accuracy (see [1] for an extensive summary and review). With the discovery of the Higgs particle in 2012 and the measurement of its mass at the Large Hadron Collider (LHC) experiments by both the ATLAS and CMS collaborations [2–4], the final parameter of the SM is known and it is now a fully predictive theory.

Despite its enormous success, the SM leaves many questions unanswered. What is the souce of electroweak symmetry breaking? What is the nature of dark matter? How does gravity fit into the framework? As a quantum field theory, the SM alone is inconsistent at high energies, and therefore must be viewed as an incomplete effective theory that is only valid for describing low energy physics. This incompleteness means that there must be new physics beyond the SM, and such new physics will likely lead to new particles or new forces.

Chapter 1

The Standard Model

1.1 Forces

The Standard Model is a relativistic quantum field theory described by a renormalizable Lagrangian. It describes three of the four observable forces – the strong, weak, and electromagnetic forces. Classically, these forces are described as analogs of electric and magnetic fields that can propagate through spacetime. These fields can be obtained from gauge fields $A^a_\mu = (\phi^a, \vec{A}^a)$. The various gauge fields in the SM are classified by the symmetries they transform under, which is taken to be $SU(3)_c \times SU(2) \times U(1)_Y$. They are governed by analogs of Maxwell's equation, which can be derived from a Lagrangian obeying gauge invariance.

Mathematically, gauge theories describe fiber bundles of spacetime. Associated with each gauge group is a connection (or gauge field) $A^a_\mu(x)$ that tells us how parallel transport is performed on the fiber bundle, or how different fibers should be compared at neighboring locations. Gauge invariance is then simply a consistency requirement that the fields are describing a consistent fiber bundle. The gauge fields associated with $SU(3)_c$, denoted by G^a_μ, are $\mathfrak{su}(3)_c$ lie algebra valued and describe the 8 gluons of strong interactions. The gauge fields associated with $SU(2)_l \times U(1)_Y$, denoted by W^a_μ, B_μ, describe the $W^\pm, Z^0$ bosons and the photon γ after electroweak symmetry breaking. Associated with each gauge field is a

field strength tensor, which describes the curvature of the fiber bundle. The Lagrangian for the gauge fields is given by

$$\mathcal{L}_{\text{gauge}} = -\frac{1}{4}G^{\mu\nu a}G^{a}_{\mu\nu} - \frac{1}{4}W^{\mu\nu a}W^{a}_{\mu\nu} - \frac{1}{4}B^{\mu\nu a}B^{a}_{\mu\nu} \tag{1.1}$$

where $G^{a}_{\mu\nu}$ are the $SU(3)_c$ field-strength tensors, $W^{a}_{\mu\nu}$ the $SU(2)_l$ field-strengths and $B_{\mu\nu}$ the $U(1)_Y$ hypercharge field-strength. In the SM, these gauge fields are quantized and give rise to the force carriers.

1.2 Matter

In addition to gauge fields, there are additional matter fields that are charged under the three forces. Mathematically, matter fields are extensions of the fiber bundles that parallel transport under the gauge connections. The different matter fields can then be classified by their transformation properties under the SM gauge group, which are shown in Table 1.1, where $q, \bar{u}, \bar{d}$ are the quarks, and $l, \bar{e}$ are the leptons. All the quarks and leptons are

matter	$SU(3)_c$	$SU(2)$	$U(1)_Y$
$q = \binom{u}{d}$	3	2	$\frac{1}{6}$
$\bar{u}$	$\bar{3}$	1	$-\frac{2}{3}$
$\bar{d}$	$\bar{3}$	1	$\frac{1}{3}$
$l = \binom{\nu}{e}$	1	2	$-\frac{1}{2}$
$\bar{e}$	1	1	1
φ	1	2	$\frac{1}{2}$

Table 1.1: Standard Model Matter Content. The Higgs field φ is a complex scalar and all the other matter fields are left-handed weyl spinors. Each lepton and quark comes in three families.

fermionic left-handed weyl spinors, which come in three flavors. φ describes the Higgs field and is the only complex scalar in the SM. Each of the matter fields come with a kinetic term in the Lagrangian. The most general renormalizable Lagrangian given the matter content

is given by

$$\mathcal{L}_{\text{matter}} + \mathcal{L}_{\text{higgs}} = \sum_{\psi \in \{q,\bar{u},\bar{d},l,\bar{l}\}} i\psi^{i\dagger}\bar{\sigma}\cdot D\psi_i + |D\varphi|^2 - V(\varphi)$$
$$- \lambda^l_{ij}(\epsilon\varphi) l_i \bar{e}_j - \lambda^u_{ij}(\epsilon\varphi) q_i \bar{u}_j - \lambda^d_{ij}\varphi^\dagger q_i \bar{d}_j \tag{1.2}$$

Where the indices shown above correspond to the three flavors. $\epsilon h = \epsilon_{ij} h_j$ in $SU(2)_l$ indices, which is necessary for gauge invariance.

1.3 Higgs Mechanism

Given that the matter content does not come in charge conjugate pairs, there are no allowed mass terms of the form $mq\bar{q}, ml\bar{l}$ in the Lagrangian. The same goes for the gauge fields, where terms of the form $m^2 A^a_\mu A^{a\mu}$ explicitly violate gauge invariance. Since the matter fermions and the force carriers $W^\pm, Z^0$ are all massive, these mass-terms must be generated. Fortunately, the Higgs field can resolve all these issues. One can rewrite the general Higgs potential in the following way:

$$V(\varphi) = \frac{\lambda}{4}\left(|\varphi|^2 - \frac{v^2}{2}\right)^2 \tag{1.3}$$

Classically, when $v^2 > 0$, the Higgs will condense into a vacuum expectation value (vev). We can then fix a basis and write, $\langle\varphi\rangle = \langle(\varphi^+, \varphi_0)\rangle = (0, v/\sqrt{2})$. To properly perform perturbation theory calculations, one must substitute and expand $\varphi_0 \to (v + h_0)\sqrt{2}$ into the Lagrangian. The quartic term in the Higgs kinetic term $-|D\varphi|^2$ will give rise to desired gauge boson masses:

$$\mathcal{L} \supset \frac{1}{8}\left|\begin{pmatrix} gA^3_\mu + g'B_\mu & g(A^1_\mu - iA^2_\mu) \\ g(A^1_\mu + iA^2_\mu) & -gA^3_\mu + g'B^2_\mu \end{pmatrix}\begin{pmatrix} 0 \\ v \end{pmatrix}\right|^2$$
$$= \frac{1}{2}\frac{-gA^3_\mu + g'B^2_\mu}{g^2 + g'^2}\left[\left(g^2 + g'^2\right)\frac{v^2}{4}\right] + \left|\frac{A^1_\mu - iA^2_\mu}{\sqrt{2}}\right|^2\left[\frac{g^2v^2}{4}\right] \tag{1.4}$$

Defining $Z^0_\mu = -gA^3_\mu + g'B^2_\mu/g^2 + g'^2$ and $W^\pm = A^1_\mu \mp iA^2_\mu/\sqrt{2}$, one sees that this leads to $m_{Z^0} = \sqrt{g^2+g'^2}v/2$ and $m_{W^\pm} = gv/2$. As for the fermions, a Higgs vev gives rise to mass terms of the form

$$\mathcal{L} \supset \frac{\lambda^l_{ij}v}{\sqrt{2}} e_i \bar{e}_j + \frac{\lambda^u_{ij}v}{\sqrt{2}} u_i \bar{u}_j - \frac{\lambda^d_{ij}v}{\sqrt{2}} d_i \bar{d}_j \tag{1.5}$$

After diagonalizing the Yukawa matrices by choosing a basis for $q, \bar{u}, \bar{d}, l, \bar{e}$, the fermions get masses of the form $m^{e,u,d}_i = \lambda^{e,u,d}_i v/\sqrt{2}$.

1.4 Sensitivity to New Physics

So far the analysis is at the classical level. As a quantum theory, the structure of electroweak symmetry breaking gets modified at loop level by quantum effects. Consider a particle ϕ (fermion or boson) that couples to the Higgs field. The mass of ϕ, M_ϕ, will depend nontrivially on v. Then the classical potential will be modified when interactions with the ϕ field is included. At the one-loop level, we have the Coleman Weinberg formula [5]:

$$\begin{aligned}\Delta V_{\text{one-loop}} &= \frac{(-1)^F}{2}\int^\Lambda \frac{d^4p}{(2\pi)^4}\log(p^2 + M^2_\phi(v)) \\ &= \frac{(-1)^F}{64\pi^2}\left[M^2_\phi\Lambda^2 + M^4_\phi \log\frac{M^2_\phi}{M^2_\phi+\Lambda^2} + \Lambda^4\log(M^2_\phi+\Lambda^2)\right]\end{aligned} \tag{1.6}$$

Where we have neglected M_ϕ independent constants. Equation 1.6 naively diverges from integration over regions with large p^2, or the ultraviolet (UV). Such a divergence is artifical, as we expect new physics to emerge at large momentum and thus regularize the integral. Since we do not know what the new physics is yet, we parameterize our ignorance by cutting off the integration at Λ. For multiple particles that couple to the Higgs, one simply adds the individual contributions together.

Equation 1.6 has the peculiar property that it depends quadratically on Λ^2. If Λ^2 is very large, it could easily alter electroweak symmetry breaking. In order for electroweak symmetry breaking to happen, all these potentially very large Λ^2 terms must cancel each

other to give a potential that has a minimum at around $\sim$ 100 GeV. This unnatural sensitivity is known as the hierarchy problem. One can avoid this situation if Λ^2 is small or the M_ϕ^2 dependence on v is small. In the SM, the top-quark mass already depends strongly on the Higgs vev. This indicates that without some special cancellation between the top quark contribution and other particles, Λ should not be much larger than $\sim$1 TeV. A small Λ indicates that new physics should emerge around this scale, which has not been observed in experiments yet.

The most theoretically appealing way to solve the hierarchy problem is to propose new symmetries that enforce cancellations of the sensitivity to Λ, for example, supersymmetry and little Higgs theories (For a review, see [6, 7]). Supersymmetry imposes a symmetry between bosonic and fermionic degrees of freedom such that fermionic contributions that come with an extra $(-1)^F$ cancel the bosonic contributions. Such a cancelation is valid to all orders and in fact removes all the sensitivity of the electroweak sector to UV physics. Little Higgs theories, on the other hand, extend the electroweak gauge symmetry and require that the vev dependent part of M_ϕ^2 come in equal and opposite contributions. The sensitivity to UV is reduced but not removed entirely, which allows Λ to be significantly above $\sim$ TeV.

1.5 Supersymmetric Standard Model

Supersymmetry (SUSY) postulates that particles come in pairs of bosons and fermions with related couplings and charges. Supersymmetry is also required in string theory, which is the only theory of quantum gravity that may incorporate the SM. Furthermore, the simplest supersymmetric extension of the SM predicts gauge coupling unification. All these appealing features make supersymmetry the leading candidate for solving the hierarchy problem.

One way to realize supersymmetry is by enlarging the concept of spacetime. To do so, the concept of real numbers needs to be extended to include Grassmann variables $\{\eta_1, \eta_2, ...\}$ that anticommute $\eta_i\eta_j = -\eta_j\eta_i$. A general element of the Grassmann algebra is a linear combination of products of arbitrarily many η_i. There is a natural "parity" operator that

decomposes any element of the Grassmann algebra into even and odd pieces:

$$x = x_{\text{odd}} + x_{\text{even}} = \sum_{\text{odd } N} x_{i_1,i_2,...i_N}\eta_{i_1}\eta_{i_2}...\eta_{i_N} + \sum_{\text{even } N} x_{i_1,i_2,...i_N}\eta_{i_1}\eta_{i_2}...\eta_{i_N} \tag{1.7}$$

A super-vector space $\mathbb{R}^{m|n}$ is then an m-tuple of even elements with an n-tuple of odd elements of the Grassmann algebra. $\mathcal{N} = 1$ supersymmetric theories are then theories of fields in $\mathbb{R}^{4|4}$, where spacetime is augmented with 4 extra Grassmann-odd coordinates. We can label the coordinates as $(x^\mu, \theta_\alpha, \bar{\theta}^{\dot{\alpha}}) \in \mathbb{R}^{4|4}$. Fields of space-time are then generalized into super-fields of super-space, or in other words, maps of $\mathbb{R}^{4|4} \to \mathbb{R}^{1|0}$. The usual Poincaré invariance is extended to include superspace translations. The super-translations are parameterized by odd-elements of Grassmann algebra $(\xi, \bar{\xi}) \in \mathbb{R}^{0|4}$, and is given by [1]

$$(x^\mu, \theta, \bar{\theta}) \to (x^\mu - i\theta\sigma^\mu\bar{\xi} + i\xi\sigma^\mu\bar{\theta}, \theta + \xi, \bar{\theta} + \bar{\xi}) \tag{1.8}$$

The concepts of fields are generalized to superfields, which can be decomposed into a finite series of $\theta, \bar{\theta}$ as $\theta^3 = \bar{\theta}^3 = 0$,

$$\begin{aligned}\Phi(x, \theta, \bar{\theta}) = \phi(x) + \theta\chi(x) + \bar{\theta}\bar{\eta}(x) + \theta\sigma^\mu\bar{\theta}V^\mu(x) + \theta^2 m(x) + \bar{\theta}^2 n(x) + \\ \bar{\theta}^2\theta\lambda(x) + \theta^2\bar{\theta}\bar{\psi}(x) + \theta^2\bar{\theta}^2 D(x)\end{aligned} \tag{1.9}$$

Under super-translations, these coefficients will transform into each other. In particular, the shift in x^μ will transform terms with lower powers of $\theta, \bar{\theta}$ into higher ones. Shifts in $\theta, \bar{\theta}$ will transform terms with higher powers of $\theta, \bar{\theta}$ into lower ones. Then, a SUSY transformation on $D(x)$ will solely come from the shift in x^μ, and thus must be in the form of a total derivative $\delta D(x) \sim \partial_\mu J^\mu$, which will vanish when integrated over d^4x. Therefore the $\theta^2\bar{\theta}^2$ component of any superfield integrated over $\int d^4x$ is invariant under super-translation. It is possible to construct additional SUSY invariants by noting that the variables $y^\mu = x^\mu - i\theta\sigma^\mu\bar{\theta}$ transforms into $y^\mu \to y^\mu - 2i\theta\sigma^\mu\bar{\xi} - i\xi\sigma^\mu\bar{\xi}$ under super-translations, which is independent of $\bar{\theta}$. One can then define chiral super-fields as superfields that only depend on (y^μ, θ), which can be Taylor expanded into

$$\Psi = \phi(y) + \sqrt{2}\theta\psi(y) + \theta^2 F(y) \tag{1.10}$$

[1] The relative -1 between ξ and $\bar{\xi}$ translation is necessary to ensure x^μ remains Hermitian when $\bar{\phi} = \phi^\dagger$ and $\bar{\xi} = \xi^\dagger$. The hermiticity requirement is directly related to unitiary and must be enforced.

Through the same argument, we see that $F(y)$ transforms into a total divergence under SUSY, and its integral over $\int d^4x$ is thus SUSY invariant.

Given the extension of spacetime to superspace, the SM can be extended to the Minimal Supersymmetric Standard Model (MSSM). Gauge fields are promoted to vector superfields that satisfy $V^\dagger = V$, and matter fields are generalized to chiral superfields. The MSSM matter content is summarized in Table 1.2. All the gauge bosons now come with fermionic

matter	boson	fermion	$SU(3)_c$	$SU(2)$	$U(1)_Y$
V_G	G^a_μ	λ^a_G	Ad	1	0
V_W	W^a_μ	λ^a_W	1	Ad	0
V_B	B^a_μ	λ_B	1	1	Ad
$Q = \binom{U}{D}$	$\binom{\tilde{u}}{\tilde{d}}$	$\binom{u}{d}$	3	2	$\frac{1}{6}$
$\bar{U}$	$\tilde{\bar{u}}$	$\bar{u}$	$\bar{3}$	1	$-\frac{2}{3}$
$\bar{D}$	$\tilde{\bar{d}}$	$\bar{d}$	$\bar{3}$	1	$\frac{1}{3}$
$L = \binom{N}{E}$	$\binom{\tilde{\nu}}{\tilde{e}}$	$\binom{\nu}{e}$	1	2	$-\frac{1}{2}$
$\bar{E}$	$\tilde{\bar{e}}$	$\bar{e}$	1	1	1
H_u	h_u	$\tilde{\bar{h}}_u$	1	2	$\frac{1}{2}$
H_d	h_d	$\tilde{\bar{h}}_d$	1	2	$-\frac{1}{2}$

Table 1.2: Minimal Supersymmetric Standard Model Matter Content. The gauge fields are grouped into vector superfields, and the matter fields are grouped into chiral superfield.

gaugino parterns. The SM fermions come with a bosonic partner, and the Higgs boson is extended to two Higgs chiral superfields H_u, H_d, which also include the fermionic partners to the Higgses. The Yukawa coupling is generalized to couplings between chiral superfields:

$$\mathcal{L}_{\text{MSSM}} \supset \left(-\lambda^l_{ij}(\epsilon H_u)L_i\bar{E}_j - \lambda^u_{ij}(\epsilon H_u)Q_i\bar{U}_j - \lambda^d_{ij}H_dQ_i\bar{D}_j\right)\Big|_{\theta^2 \text{ component}} \tag{1.11}$$

We see that in addition to fermion-Higgs coupling, the Lagrangian also contains Higgs-scalar coupling of the form $|h_u|^2|\tilde{s}|^2$, where $\tilde{s}$ is any scalar partner of the SM quarks and leptons. This implies that if SUSY is exact, the bosonic partner has the same mass dependence on the Higgs vev as the fermions. Thus the correction to the Higgs potential is zero according to Equation 1.6. This statement is actually true to all loop orders as a result of supersymmetry.

If supersymmetry is true, one should be expected to observe a bosonic (fermionic) counterpart to all SM fermions (bosons). This has not been observed so far, thus SUSY must be spontaneously broken if it were true. A spontaneously broken SUSY will result in residual logarithmic sensitivity to the SUSY breaking scale, implying that super-partners of SM particles cannot be too heavy (otherwise the residual sensitivity will cause another hierarchy problem). The full MSSM Lagrangian involving gauge fields and SUSY breaking terms is rather complicated, and we refer to [6] for a detailed review. The existence of new colored and electroweak charged states not far beyond the electroweak scale gives us hope that they may be produced and disocvered through collider experiments.

1.6 Conclusion

In this chapter, we have reviewed the basics of the Standard Model as a quantum field theory. Using the principles of gauge invariance, masses for the gauge and matter fields are forbidden. We reviewed how the Higgs Mechanism is able to generate the required mass terms through a symmetry breaking potential. However, such a potential gets large quantum corrections, and we saw how successful electroweak symmetry breaking requires fine-tuning. Fine-tuning could be removed or reduced by introducing new symmetry principles, which tend to lead to new physics not far beyond the electroweak scale. This leads to the motivation for building collider experiments to find such new physics, which we will turn to in Chapter 2.

Chapter 2

LHC Collider Physics

The Large Hadron Collider (LHC), currently the largest and most powerful particle collider in the world, is the front runner for discovering new particles. As protons with $\sim$ TeV energies are collided against each other, new particles beyond the SM may be produced and discovered. Many new physics models that explain the electroweak symmetry breaking mechanism predict new particles at the TeV scale and should be accessible at the LHC. Some examples are the stop and gluino in supersymmetry [6] and the top partners in little higgs models [7].

Given the expectations of new physics beyond the Standard Model and its unknown nature, we need a robust and general experimental program for its discovery. The culmination of many efforts in the science communities led to the construction of the ATLAS (A Toroidal LHC Apparatus) and the CMS (Compact Muon Solenoid) particle detector experiments, centered along the Large Hadron Collider (LHC). The ATLAS and CMS experiments open up a new era of experiment driven particle physics, which we will review in the following chapters.

2.1 The LHC as a Discovery Machine

The LHC is a proton-proton collider with center of mass energy $\sqrt{s}$ $\sim$TeV. It is the largest and most powerful particle collider to date. The first round of proton-proton collision data

was gathered in 2010 at $\sqrt{s} = 7$ TeV, delivering close to 50 pb^{-1} of data. The second round of proton-proton collisions started in 2012 at $\sqrt{s} = 8$TeV, delivering slightly more than 20 fb^{-1} of data. Recently, in June 2015, the LHC has starting operation at 13 TeV.

Since nature is quantum mechanical, the number of each type of collision events is random. The expected number of a specific physical process is given by

$$N_{\text{event}} = \sigma \times \epsilon \times \int L dt \tag{2.1}$$

where σ is the production cross section. The integrated luminosity $\int L dt$ measures the total amount of gathered data, and is proportional to the total number of interactions. ϵ is the efficiency of the event selection criterion. Since the proton is a composite particle, the production cross section in general cannot be computed directly. Fortunately, as collisions happen at much greater energies than the composite scale of the proton, the cross sections can in general be approximated through factorization, such that

$$d\sigma(pp \to X) = \int dx_1 dx_2 f_{p\to p_1}(x_1) f_{p\to p_2}(x_2)\, d\sigma(p_1 p_2 \to X) \tag{2.2}$$

where $f_{p\to p_i}(x_i)$, the parton distribution function (PDF), is interpreted as the probability of obtaining a parton p_i from a proton with momentum fraction x_i. The PDF cannot be computed directly, but is universal and can be extracted from previous collider experiments. Figure 2.1 shows an example PDF fit by the MSTW collaboration [8]. The parton level cross section, $d\sigma(p_1 p_2 \to X)$, can then be directly calculated from Feynman diagrams. From Equation 2.2, one sees that the center-of-mass energy of the partons, $\sqrt{\hat{s}} = \sqrt{x_1 x_2}\sqrt{s}$, for a given physical process is always less than the total energy of the collision. In fact, from Figure 2.1, one sees that the PDFs are dominated by small x, hence most of the heavy particles produced will be approximately at rest. Thus we come to two important conclusions:

- p-p collisions scan a wide energy range, and are capable of producing new heavy particles at a variety of masses.

- The total production cross section for new particles with mass M falls sharply as M

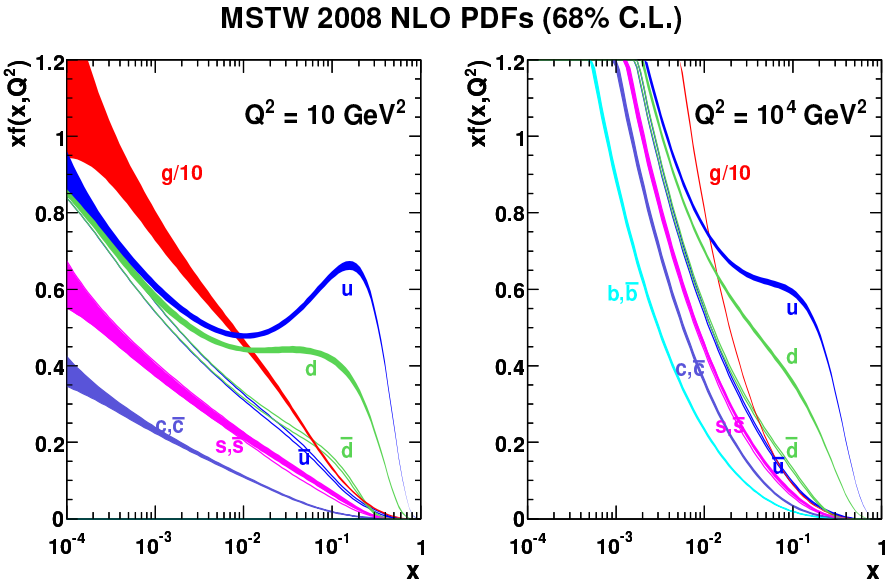

Figure 2.1: The PDFs for various partons at different renormalization scales. Figure taken from [8].

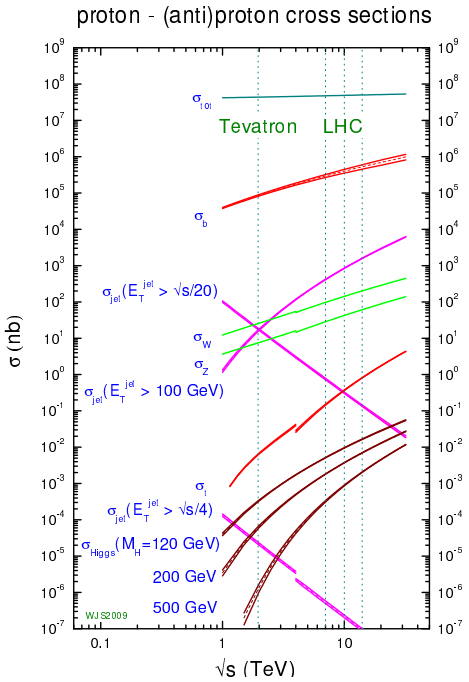

Figure 2.2: The total interaction cross section for various SM processes at the Tevatron and at the LHC. Figure taken from [8].

approaches the beam energy. In other words, the production cross section for a heavy particle increases rapidly as the collision energy increases.

Given the PDFs, one can compute the typical production rates for various processes. Figure 2.2 shows the total cross section for different SM processes. The largest contribution comes from Quantum Chromo-dynamics (QCD) interactions. The next largest contribution comes from electroweak boson $W^{\pm}/Z^0$ productions, and then top quark pair production. Higgs production is many orders of magnitude lower, and many potential new physics processes have even smaller cross sections. Due to the huge amount of data presented at the LHC, physics conclusions would have to be obtained through careful statistical analysis, which we turn to next.

2.2 Exclusion and Discovery

The simplest LHC physics analysis involves counting experiments. Given a set of selection criteria, one computes the predicted observed number of events N_{Model} assuming a particular model is correct. More precisely, since N_{Model} is in general random, one would need to compute (or approximate) the probability distribution of observing N given the selection criteria. If we know all the details of our model with no uncertainties, the probability distribution will be Poissonian:

$$P_{\text{Model}}(N) = \text{Poisson}(N|\lambda_{\text{Model}}) = \sum_{N} \frac{\lambda_{\text{Model}}^{N}}{N!} e^{-\lambda_{\text{Model}}} \tag{2.3}$$

Though, more generally, P_{Model} will be modified when systematic uncertainties are taken into account. In order to make an exclusion, one will then perfrom an analysis on the data, and measure the observed number of events N_{obs}. For models that predict an excess of events, an exclusion can be made at a particular confidence α, when the following condition is satisfied[1] :

$$\sum_{N \leq N_{\text{obs}}} P_{\text{Model}}(N) \leq 1 - \alpha \tag{2.4}$$

In experiments, more sophisticated CL_s test-statistics are employed [9]. But for theoretical studies, Equation 2.4 is often adequate. A discovery of physics beyond the SM would

[1] Typically, $\alpha = 0.95$, or 2σ for exclusion and $1 - \alpha = 3 \times 10^{-7}$, or 5σ for discovery

imply incompatibility of the observation compared to SM at the 5σ level. Significant simplifications can be made when N is large. In theoretical studies, it is often convenient to ignore systematic uncertainty as they are difficult to calculate. Under these simplifications, the Poisson distribution becomes gaussian, and the exclusion condition in Equation 2.4 is simplified into

$$\frac{N_{\text{obs}} - \lambda_{\text{Model}}}{\sqrt{\lambda_{\text{Model}}}} \geq 2 \tag{2.5}$$

Given that we expect the number of observed events to be those predicted by the SM, the expected exclusion for a given model can be roughly computed as

$$\frac{N_{\text{SM}} - N_{\text{Model}}}{\sqrt{N_{\text{Model}}}} \geq 2 \quad \Longrightarrow \quad N_{\text{Model}} - N_{\text{SM}} \gtrsim 2\sqrt{N_{\text{SM}}} \tag{2.6}$$

We see that successful exclusions of any physics model rely on having an analysis where the predicted excess over the SM is significantly higher than $\sqrt{N_{\text{SM}}}$. This requirement is the basis of almost all of the collider searches.

2.3 Kinematics

In order to perform an LHC analysis, one needs to apply stringent selection criteria on observables in order to observe potential signal over background. Below we will go over the standard kinematic variables used in LHC analyses. Typically the coordinate system is aligned such that the two colliding protons are travelling in opposite directions with four momenta $p^{\mu}_{\text{proton 1}} = (E, 0, 0, E)$, $p^{\mu}_{\text{proton 2}} = (E, 0, 0, -E)$. The interaction point is assumed to be at the origin. The four momenta of all the detected final state particles, are then p^{μ}_i. Given that the lab frame is not necessarily the center of mass of the parton interactions, it is useful to decompose p^{μ}_i into components that transform differently under boost in the z-direction. There are two common ways to rewrite a four-vector

$$p^{\mu}_i = \left(\sqrt{m^2 + p_T^2}\cosh y, \vec{p}_T, \sqrt{m^2 + p_T^2}\sinh y\right) = \left(\sqrt{p_T^2\cosh^2\eta + m^2}, \vec{p}_T, p_T \sinh\eta\right)$$
$$\vec{p}_T = (p_T\cos\phi, p_T\sin\phi) \tag{2.7}$$

where y is the rapidity and η the pseudo-rapidity, and $\vec{p}_T$ is the transverse momentum. Under longitudinal boost, the $\vec{p}_T$ is unchanged, and y changes additively. For almost all of the detected final state particles, $m \approx 0$ compared to the collision energy, and $y = \eta$. The pseudo-rapidity has the advantage that it is directly related to the angle with respect to the beam axis, $\sinh \eta = \cot \theta$. The phase space of a single particle becomes

$$\frac{d^3\vec{p}}{(2\pi)^3(2E_p)} = \frac{dyd^2\vec{p}_T}{2(2\pi)^3} = \frac{p_T \cosh \eta d\eta}{2\sqrt{p_T^2 \cosh^2 \eta + m^2}} \frac{d^2\vec{p}_T}{(2\pi)^3} \tag{2.8}$$

We see that the phase space is proportional to dy, which is invariant under longitudinal boost, or $d\eta$ in the massless limit. Loosely speaking, particle production is roughly constant in units of η.

For a $2 \to N$ collision process, the total momentum of all the final state particles is given as $\sum p_i^\mu = ((x_1 + x_2)E, 0, 0, (x_1 - x_2)E)$. Where x_1, x_2 are the momentum fractions of the partons. The rapidity for the entire event is then

$$y = \frac{1}{2} \ln \left(\frac{x_1}{x_2} \right) \quad \Longrightarrow \quad x_1 = \sqrt{r}e^y \quad x_2 = \sqrt{r}e^{-y} \quad r = x_1 x_2 \tag{2.9}$$

we see that the distribution of y is given by

$$\frac{d\sigma}{dy} = \int dr f_{p \to p_1}(\sqrt{r}e^y) f_{p \to p_2}(\sqrt{r}e^{-y})\, \sigma(p_1 p_2 \to N) \tag{2.10}$$

Since the total cross section $\sigma(p_1 p_2 \to N)$, after integration over the phase space, is Lorentz invariant, it only depends on the center-of-mass energy, or $\hat{s} = rs$. We see that the rapidity distribution depends mainly on the PDF. For processes with large r, the PDFs are falling sharply. Equation 2.10 tells us that only regions of small $|y|$ contribute significantly. This implies that for typical processes, the final-state particles will tend to be central, having relatively small $|\eta|$.

Given that the distribution of η for any final-state particle is unknown, the longitudinal boost invariant p_T is used as a measure of the interaction energy. A typical analysis will involve choosing collider objects with modest $|\eta|$ and large p_T. We will review these objects in the next chapter.

2.4 Collider Objects

In order to target specific new physics signatures, it is necessary to identify the type of particles produced in the partonic processes. However, the mapping between particles seen at a detector and the parton processes may not be straightforward:

1. Detectors are imperfect and misidentification of particles does happen.
2. Only stable (sufficiently long-lived) final states that interact with the detectors are observed.
3. Quarks and gluons are not observed in the final states; instead, they hadronize into hadrons and baryons.

The first point is purely an experimental issue and can be mitigated by better calibrations and event selection. The second point forces us to consider the entire decay chains for a given process. This may necessitate multiple analyses for theoretically similar physical processes. For example, top quarks may decay leptonically or hadronically, and each channel requires very different analysis strategies. The third point tells us that all color charged final states will go through showering and non-perturbative hadronization, causing extra complications in their physics interpretations. The most common directly detected particles are: $\gamma, \pi^{\pm,0}, p^{\pm}, n, e^{\pm}, \mu^{\pm}$. These particles are identified by a combination of tracking and calorimeter measurements. Figure 2.3 shows a schematic of what the different final state particles look like in the detector. Given the signature of particles observed at a detector, they can be grouped into several categories. Below we briefly discuss the main detector objects used in traditional searches.

2.4.1 Leptons and Photons

Electrons and muons are among the most well-measured objects at colliders. They are identified by a distinctive high p_T track measured by the tracker. Electrons mainly deposit their energy in the electromagnetic calorimeter. Muons, on the other hand, do not interact

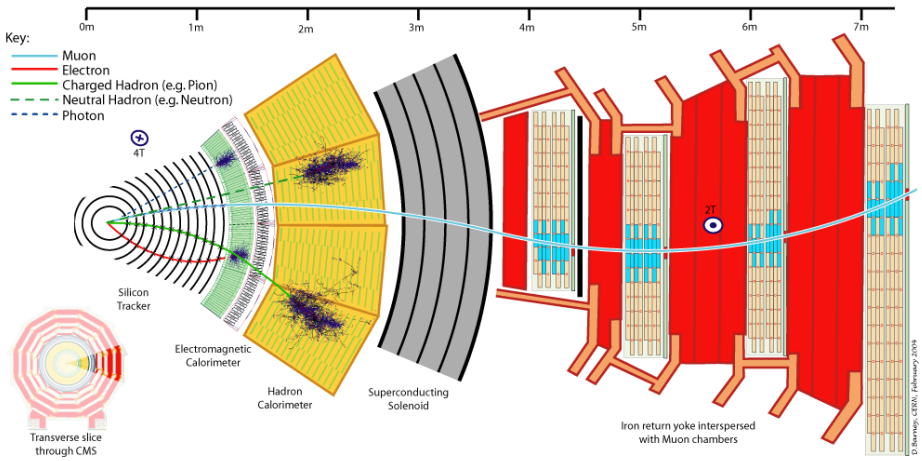

Figure 2.3: Schematic of the CMS detector [10].

significantly with the calorimeter since they are heavier. They travel outward to the muon chambers where their momenta are measured once again. As for tau leptons, or $\tau^{\pm}$, they decay into either hadrons or other leptons together with neutrinos and are not directly measured at colliders. Their identification is still possible, but much more complicated. Therefore, at colliders, decay channels involving $e^{\pm}, \mu^{\pm}$ are much prefereed over those involving $\tau^{\pm}$. Photons are similar to electrons except that they do not leave a distinctive track since they are not charged.

Leptons and photons in an event are often produced through electroweak processes, and thus usually do not come with signifcant extra radiation. Therefore, isolation requirements are typically imposed on them to reject fakes from hadronic activity. In the SM, the production of isolated $e^{\pm}, \mu^{\pm}, \gamma$ largely come from electroweak interactions and thus is strongly reduced. Therefore, new physics involving these objects tends to have much tighter experimental constraints.

2.4.2 Transverse Missing Momentum

Energetic particles that are undetected also offer a robust way to look for a variety of new physics. By momentum conservation, the sum of all the transverse momenta of the particles

must add to zero, i.e. $\sum \vec{p}_{Ti} = 0$. Then one can define the transverse missing momentum

$$\vec{\not{E}}_T = -\sum_{i \in \text{visible}} \vec{p}_{Ti} \tag{2.11}$$

For a detector with perfect coverage and perfect resolution, $\vec{\not{E}}_T$ is the momentum sum of all the invisible particles. In the SM, the only source of real $\vec{\not{E}}_T$ comes from neutrinos, which is produced via electroweak interactions and usually $\not{E}_T$ is of the order of the electroweak scale $\sim \mathcal{O}(100$ GeV). There is also missing momentum coming from mismeasurements, which affect the quality of the $\vec{\not{E}}_T$ variable. Figure 2.4 shows an example event where $\vec{\not{E}}_T$ may have come from a W-boson decaying into an electron and a neutrino. One sees a large momentum imbalance almost back-to-back with the electron.

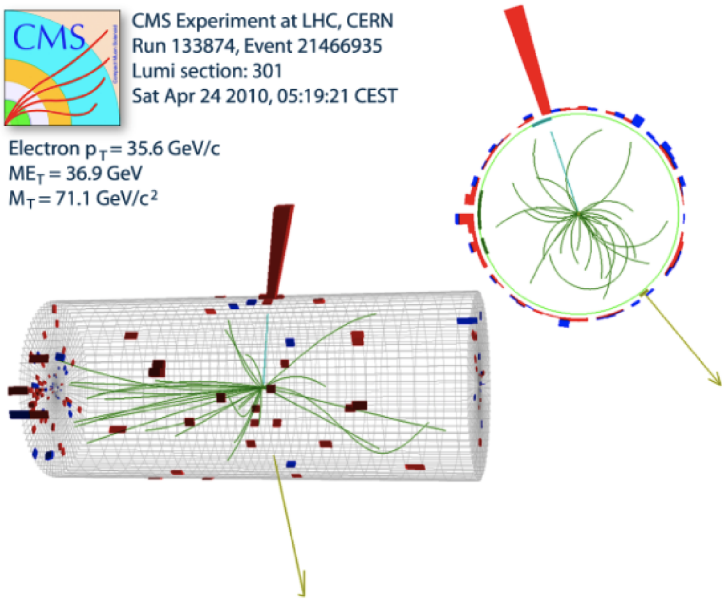

Figure 2.4: A W candidate event decaying into $e + \nu$ as observed by the CMS. The red column indicates energy deposition in the calorimeter. The arrow indicates the $\vec{\not{E}}_T$

In addition to the absolute value of $\vec{\not{E}}_T$, its angular dependence is also useful for searches. New stable particles do not have strong interactions and thus tend to be relatively separated from hadronic activity. Typical searches require a large $\Delta\phi$ separation between $\vec{\not{E}}_T$, and the momenta of other particles. Together with leptons and photons, $\vec{\not{E}}_T$ is among the most well-measured and powerful collider objects for the search of new physics.

2.4.3 Jets

The most common types of fundamental particles produced at hadron colliders are quarks and gluons. However, as the strong coupling gets larger at large distances, quarks and gluons are never seen as final states. Instead, these particles (or partons) shower and hadronize into a large number of hadrons. Individual hadrons can be identified by their tracks (when they are charged) and their energy deposition in the hadron calorimeters. The physics of parton showering can be understood perturbatively, and hadronization can typically be treated as a small effect. Such an assumption is valid as long as the interaction energy is much larger than the scale $\Lambda_{\rm QCD} \simeq 200$MeV, where $\Lambda_{\rm QCD}$ is the scale where the strong force becomes non-perturbative. In physics searches, colliminated hadrons are clustered into jets through recombination algorithms [11, 12]. These jet objects can be simulated through Monte Carlo algorithms [13, 14]. For a detailed discussion, we refer the reader to [15].

In the SM, jets are produced mainly through QCD interactions, and thus have much larger production cross sections than processes involving other collider objects such as leptons and neutrinos. Still, jets are indispensible tools for searches, as any new physics scenarios that involve QCD charged particles will involve the production of jets, which may or may not be accompanied by other objects such as leptons and $\vec{\not{E}}_T$.

2.5 Conclusion

In this chapter, we have reviewed the basics of proton colliders and collider physics at the LHC. We saw how high energy proton-proton collisions can be viewed as collisions of the constituent partons. The collision energies of these partons span orders of magnitude, making the LHC a discovery machine. We also reviewed some common physics objects (leptons, $\vec{\not{E}}_T$ and jets) and various common observables at colliders. We see that collision events in general have unknown boost factors along the beamline, and thus transverse variables are used frequently in physics analysis and object selections. In the following chapters, we will utilize the collider physics outlined here and propose many searches that

could reveal new physics at the LHC.

Part II

New Physics at the LHC

Traditional physics searches at the LHC typically require some combination of collider objects: for example, leptons, jets and $\vec{\not{E}}_T$ with high transverse momentum. In many SUSY searches, it is assumed that the lightest supersymmetric particle (LSP) is stable and thus produces significant $\not{E}_T$. In the following chapters we will study how new physics scenarios may violate these traditional assumptions. For example, in R-Parity Violating SUSY scenarios, the LSP can decay into jets, removing the $\vec{\not{E}}_T$ handle. We will examine a novel way to search for these scenarios in Chapter 3. There are also new physics scenarios that lead to more exotic collider objects such as displaced vertices. In Chapter 4, we will examine a new data-driven way to search for the Higgs boson decaying into long-lived particles that produce displaced vertices. Traditional dark matter searches at the LHC usually assume that the dark matter is isolated from hadronic activity. In Chapter 5, we will examine a class of dark matter models that violate such an assumption. These scenarios produce large $\not{E}_T$, but the $\vec{\not{E}}_T$ is correlated with the jet momenta in the event, which is discarded by traditional searches. We will discuss a new way to search for these signals. Chapters 3-5 are published in [16–18] respectively. The work in Chapter 3 was presented in Phenomenology 2012 Symposium and Boost 2013 Conference. The work in Chapter 5 was presented in Phenomenology 2015 Symposium and an invited seminar at MIT.

Chapter 3

New Physics in Multijets: Accidental Jet Substructure

3.1 Introduction

Our approach to jet physics is undergoing a renaissance. While most LHC studies use the energy and momentum of a jet, there is growing appreciation for the wealth of information that can be extracted by analyzing a jet's internal structure (see [19–21] for reviews). Jet substructure gained traction when it was shown to increase the LHC sensitivity to Higgs boson decays into b-quarks [22]. Since then, jet substructure has been applied by theorists to a variety of scenarios [23–45], and its power has been demonstrated experimentally in Tevatron [46, 47] and LHC [48–54] searches.

In all existing studies, jet substructure has been used to search for boosted resonances with collimated decay products that are reconstructed as a single jet. For a typical event at the LHC, parent particles are produced near threshold; the decay products are boosted for the small fraction of signal events produced with significant transverse momentum,[1] or in the case where the parent particle decays to significantly lighter daughters. In this chapter, we explore a new application for jet substructure techniques that does not rely on having

[1] For example, the signal efficiency when targeting boosted gluinos is roughly $\mathcal{O}$(few %) at the LHC [55,56].

collimated decay products.

We demonstrate that substructure technology is useful in the non-boosted regime for models that yield a high multiplicity of hadronic final states. This strategy relies on the fact that when new particles with $\mathcal{O}(\text{TeV})$ masses are produced at threshold, their decay products tend to be distributed isotropically in the detector. Our proposal requires an event to contain several (specifically, four or more) large-radius jets defined using the anti-k_T algorithm [11] with angular size $R = 1.2$. Because these so-called "fat" jets can cover a large fraction of the effective detector area, several decay partons from a high-multiplicity signal will often get clustered into a single fat jet. Non-boosted final states can therefore manifest "accidental substructure."

Requiring multiple fat jets with non-trivial substructure greatly reduces QCD contamination. For an event to have four fat jets, it must have at least this many well-separated hard partons. The presence of substructure in the remaining QCD sample is most likely to occur when one or more isolated partons undergoes a hard $1 \to 2$ splitting. Because this process is dominated by a soft and/or collinear singularity, the probability decreases as the energy and separation of the final states increases. As a result, QCD events typically have suppressed substructure.

Figure 3.1 illustrates why accidental substructure is useful for distinguishing between a typical signal and background event. These "lego plots" show the spatial distribution of calorimeter activity in the $\eta - \phi$ plane, where η is pseudorapidity and ϕ is azimuthal angle. The left panel is a lego plot for a signal event with up to 18 partons in the final state; the signal is gluino pair production, where each gluino decays to a pair of top quarks and an unstable neutralino that decays to three partons (see the left diagram in Fig. 3.2). The right panel shows the lego plot for a QCD event. The different colors correspond to different fat jets in the event. It is clear that the fat jets from signal have more pronounced substructure than the ones from QCD.

Figure 3.1 suggests that cutting on the number of small-radius ($R \sim 0.4$) jets may suffice to distinguish signal from background. An explicit high jet multiplicity search requires

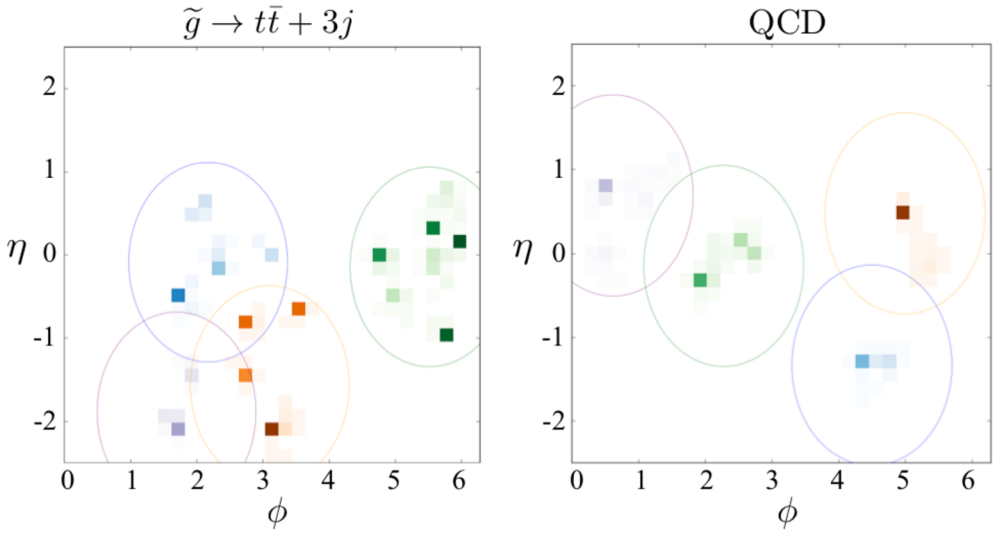

Figure 3.1: Lego plots showing the distribution of calorimeter activity in the $\eta - \phi$ plane. The different colors correspond to different fat jets; within each panel, darker colors signify higher p_T in a given detector cell. Note that the relative p_T scale is different for the signal and background example. The signal (left panel) is pair production of 500 GeV gluinos with $\widetilde{g} \to t\,\bar{t} + 3\,j$, which yields up to 18 partons in the final state. The gluinos have transverse momenta of 120 and 65 GeV, so they are essentially at rest. A QCD multijet event is depicted in the right panel. The circles are centered on the clustered fat jet with a radius of $R = 1.2$ to schematically illustrate the extent of each fat jet. There is significant substructure for the signal and suppressed substructure for the background.

accurate modeling of the QCD background, which has intrinsic theoretical challenges. The current state of the art is tree-level QCD calculations that rely on matrix element-parton shower matching up to six jets. Because additional jets must be generated by the parton shower, these calculations systematically underestimate the p_T spectrum of the high multiplicity tail. Higher multiplicity, matched, next-to-leading order calculations are not anticipated in the near future, implying that precision modifications to the shapes of the QCD distribution will not be known. Finally, even once this has been achieved, there is the computational limitation associated with populating the entire 3-n dimensional phase space for events with n jets. As a result, theorists should validate Monte Carlo background predictions against data to derive plausible limits. There exist studies from the CMS and ATLAS collaborations that present 6 jet [55,57] and 8 jet [58] distributions. However, these do not provide enough information to place cuts on the number of small-radius jets larger

than $\sim$ 6–8. This constrains theoretical investigations of high multiplicity searches with small-radius jets.

An experimental analysis targeting many small-radius jets must obtain the multijet backgrounds from data. Current data-driven methods for determining detailed kinematic features of small-radius jets are limited in that they rely on ad hoc fitting functions to perform background extrapolations. If a search that utilized these procedures yields an excess of events, there is no guidance for investigating the discrepancy because the functions are not derived from an underlying theory.[2]

Searches that use fat jets can implement an alternate strategy to estimate backgrounds. For the substructure analysis proposed here, one can study the internal structure of fat dijets. Because this sample should be signal poor, it can be used to determine the pure QCD dependence of jet mass and substructure on other quantities like jet p_T. These results can then be extrapolated to four fat jet events, and should lead to reasonable background predictions so long as the correlations between fat jets are small. Importantly, the associated systematics for a fat jet analysis differ from those that dominate in a search for many small-radius jets. It is beneficial to have competing searches with different systematics to ensure that new physics is not overwhelmed by large uncertainties.

Finally, we note that our analysis does not rely on the presence of missing transverse energy ($\not{E}_T$), which is typically crucial for discriminating against multijet backgrounds in searches for supersymmetry (SUSY). Missing energy is not a robust prediction of SUSY models, *e.g.* R-parity can be violated, the superpartner spectrum can be squeezed, or SUSY can be stealthy [61, 62]. There are also a number of non-SUSY models that have signatures without $\not{E}_T$, such as [63–66]. To cover these and other $\not{E}_T$-less theories at the LHC, it is imperative to develop new search strategies to efficiently reduce the QCD background. Such a strategy could rely on rare objects in the event, such as b-jets or leptons, to further reduce backgrounds. However, a search that is independent of these extra handles is powerful for its generality. Because our proposal *only* relies on having a final state with many jets, it

[2] For recent theoretical progress on extrapolating jet multiplicity, see [59, 60].

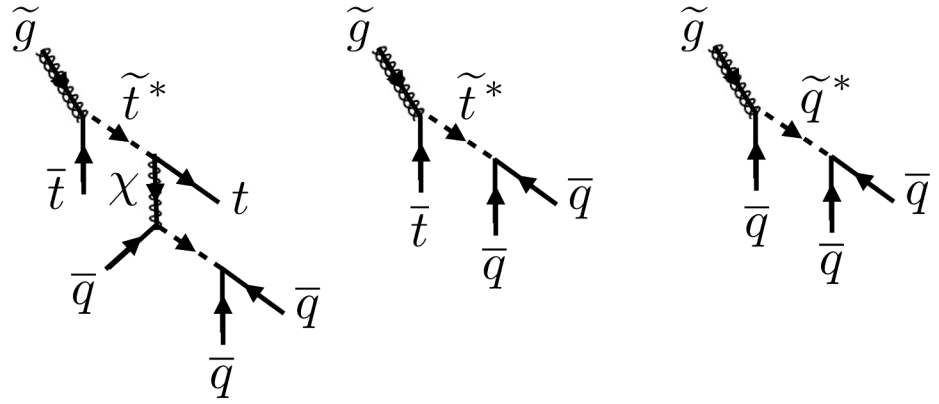

Figure 3.2: Gluino decay diagrams, illustrating topologies that can lead to as many as 18, 10, and 6-parton final states (left to right, respectively) when the gluinos are pair-produced. Note that $\widetilde{g}$ is a gluino, $\widetilde{t}$ is a stop, t is a top quark, $\widetilde{q}$ is a first or second generation squark, χ is a neutralino, and j refers to a final state quark or anti-quark.

can be used to place limits on a wide-range of model space.

We demonstrate that accidental substructure is a powerful discriminator by applying it to three distinct gluino $\widetilde{g}$ decay scenarios when the R-parity violating (RPV) superpotential coupling $U^c\,D^c\,D^c$ is non-zero:

$$\widetilde{g} \to t\,\overline{t} + 3\,j, \qquad \widetilde{g} \to t + 2\,j, \quad \text{and} \quad \widetilde{g} \to 3\,j. \tag{3.1}$$

Here j refers to a final state quark or anti-quark, not to a detector-level jet. When the gluinos are pair-produced, these three topologies can lead to as many as 18, 10, and 6-parton final states, respectively, as shown in Fig. 3.2. The first topology arises when a gluino decays to a pair of tops and an unstable neutralino, which decays to three partons through an off-shell squark via $U^c\,D^c\,D^c$. The other two topologies correspond to the RPV gluino decays into $t\,b\,s$ and $u\,d\,s$ final states. For a review of constraints on these RPV interactions, see [67]. The 18 and 10-parton topologies are particularly well-motivated theoretically because the top quarks in the final state can result from a light stop in the spectrum. This is a plausible scenario with minimal fine-tuning where the non-zero RPV couplings suppress $\not{E}_T$, thereby hiding SUSY from current searches [68]. In particular, the 10-parton topology was the focus

of a recent proposal that used substructure techniques to look for boosted stops [44].

The remainder of this chapter proceeds as follows. In Sec. 3.2, we present the needed variables, jet mass and N-subjettiness, and introduce the concept of "event-subjettiness." In Sec. 3.3, we show how these tools can be combined into a full analysis. After a brief description of the event generation procedure, we present the expected limits for the different gluino decay topologies. We conclude in Sec. 3.4. Sec. 3.5 contains a detailed description of our simulations, including validation plots.

3.2 Quantifying Accidental Substructure

Our analysis relies on two observables: total jet mass and event-subjettiness. The latter is a new variable that we introduce to quantify the amount of accidental substructure in an event. It requires N-subjettiness to characterize the subjet nature of each jet. Jet mass, N-subjettiness, and event-subjettiness form the cornerstone of our analysis, so we introduce them individually here. The full analysis strategy is presented in Sec. 3.3 and the details of our Monte Carlo event generation, detector mock-up, and validation can be found in Sec. 3.3.1 and Sec. 3.5.

For the figures in this section, we select 8 TeV LHC events with at least four jets, clustered using the anti-k_T algorithm [11] with cone size $R = 1.2$. The transverse momenta of the leading and subleading fat jets must satisfy $p_T \geq 100$ GeV and $p_T \geq 50$ GeV, respectively. Although no 8 TeV multijet, $\not{E}_T$-less triggers are publicly available, some 7 TeV examples include: five or more jets ($R = 0.4$) with $p_T > 30$ GeV at ATLAS [55], $\sim$ 500–750 GeV of H_T at CMS [58], and 4, 6, or 8 high-p_T jets ($R = 0.5$) at CMS [69]. We have verified that the first of these triggers is 100% efficient for the QCD background and the gluino topologies we consider after final selection cuts.

3.2.1 Jet Mass

Standard SUSY searches at ATLAS and CMS use a combination of missing energy, $\not{E}_T$, and visible transverse energy,

$$H_T = \sum_{j=1}^{N_j} \sqrt{(p_T^2)_j + m_j^2}, \tag{3.2}$$

where j is a jet in the event with mass $m_j \equiv \sqrt{E_j^2 - |\vec{p}_j|^2}$ and N_j is the number of jets in the event with $p_T > 50\,\text{GeV}$. The total jet mass of an event,

$$M_J \equiv \sum_{j=1}^{N_j} m_j, \tag{3.3}$$

is a more powerful discriminator than H_T in searches for high multiplicity final states [70] because a jet's mass automatically encodes gross kinematic features of its constituents.

Consider a small-radius jet that is seeded from an isolated parton. In the absence of showering, this jet will have zero mass. Non-zero jet mass arises if multiple partons are clustered together and/or from QCD radiation — the former yields a larger jet mass than the latter. As a result, a QCD and signal event with equivalent H_T can have different total jet mass. More quantitatively, H_T can be related to M_J via

$$H_T \;=\; \sum_{j=1}^{N_j} \sqrt{(p_T^2)_j + m_j^2} \;\propto\; \sum_{j=1}^{N_j} \sqrt{\langle m_j^2\rangle((\kappa R)^{-2}+1)} \;\simeq\; M_J \frac{\sqrt{1+(\kappa R)^2}}{\kappa R}, \tag{3.4}$$

where $\kappa \simeq \sqrt{\alpha_s}$ for jets whose mass is generated from the parton shower [19] and $\kappa \simeq 1$ for fat jets that contain multiple hard partons accidentally clustered in the same jet. Figure 3.3 shows the H_T and M_J distributions for background and a signal example. Clearly, a cut on M_J improves sensitivity to the signal as opposed to an H_T requirement.

The authors of [70] proposed a study that took advantage of total jet mass for high multiplicity signals, but which still relied on a missing energy cut. In this work, we demonstrate that accidental substructure increases sensitivity when used in conjunction with total jet mass. This result is especially useful in topologies with $\not{E}_T$ suppression, such as the benchmarks presented in Fig. 3.2. Adding a moderate $\not{E}_T$ cut for other topologies that do contain

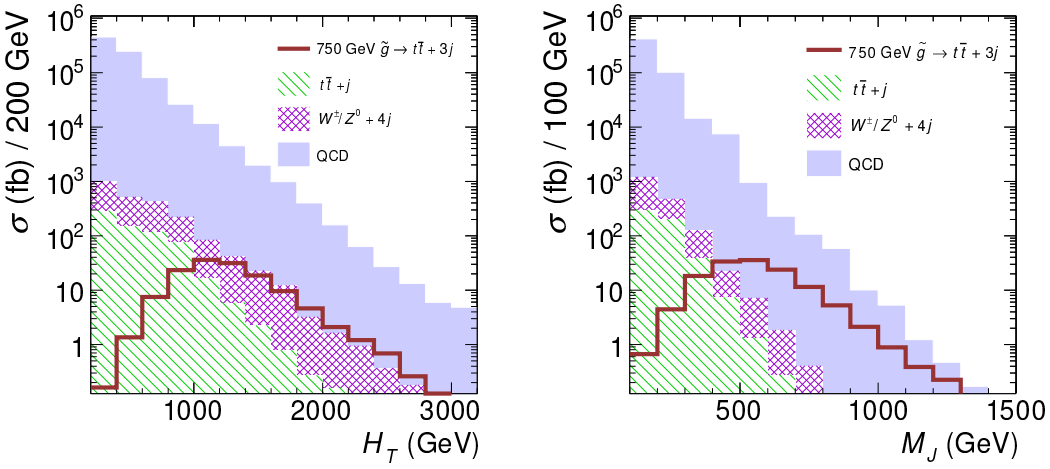

Figure 3.3: The H_T (left) and M_J (right) distributions for the backgrounds and an example signal. The signal (red solid line) is pair production of a 750 GeV gluino with $\tilde{g} \to t\,\bar{t} + 3\,j$. The stacked histogram is for background (QCD in solid blue, $W^{\pm}/Z^0 + 4\,j$ in hatched magenta, and $t\,\bar{t} + j$ in striped green). M_J is a more powerful discriminator than H_T when comparing signal to background.

sources of missing energy, *e.g.* new physics signals with tops in the final state, can provide an additional handle for improving the discriminating power of accidental substructure and jet mass.

3.2.2 N-subjettiness

To quantify accidental substructure, we begin by considering the N-subjettiness variable τ_N [32,37,71]. τ_N is a measure of the degree to which a fat jet has N well-separated subjets. For each jet, τ_N is defined as

$$\tau_N = \frac{1}{d_\beta} \sum_i (p_T)_i \min\left\{\Delta R_{i,1}^\beta, \Delta R_{i,2}^\beta, ..., \Delta R_{i,N}^\beta\right\}$$
$$d_\beta = \sum_i (p_T)_i \, R_0^\beta, \tag{3.5}$$

where the minimization is performed by varying N axes, R_0 is the choice of clustering radius, and $\Delta R_{i,M} = \sqrt{(\Delta\phi_{i,M})^2 + (\Delta\eta_{i,M})^2}$ denotes the angular distance between the i^{th} constituent particle and the M^{th} axis. We take $\beta = 1$ and $R_0 = 1.2$.

To elucidate what N-subjettiness measures, consider τ_3. If the jet consists of three or

fewer well-collimated subjets, $\tau_3 \simeq 0$ because $\min\{\Delta R_{i,1}, \Delta R_{i,2}, \Delta R_{i,3}\}$ vanishes for the i^{th} constituent. If the fat jet contains more than three subjets (or the particles making up the jet are not well-collimated), $\tau_3 > 0$ because at least one subjet is not aligned with an axis.

While the individual τ_N are not typically useful, ratios are [32]. For example,

$$\tau_{NM} \equiv \tau_N / \tau_M \tag{3.6}$$

is efficient at selecting N-subjetty events for $M < N$. For a jet with N well-separated subjets, τ_M is large, τ_N is small, and therefore τ_{NM} is much less than 1. Rejecting events with $\tau_{NM} \sim 1$ selects for jets that are more N-prong like.[3]

Figure 3.4 shows the normalized distributions of τ_{43} for each of the four hardest jets for QCD and the $\widetilde{g} \to t\,\bar{t} + 3\,j$ topology. The jets in each event are ordered by decreasing p_T. The background sample is peaked around $\tau_{43} \sim 0.7$–0.8. In contrast, the distribution for the signal is shifted to lower values, with a tail that extends to lower τ_{43}. These distributions reinforce the general conclusions we drew from the lego plots in Fig. 3.1. Specifically, τ_{43} is shifted towards lower values for the signal relative to the background, suggesting that signal jets typically look more four-subjetty than the background jets.

3.2.3 Introducing Event-subjettiness

N-subjettiness is useful for characterizing the number of subjets in a single jet. However, it would be useful to have a variable that takes into account the relative abundance of jets with substructure in an entire event. To this end, we introduce "event-subjettiness," T_{NM}, which is defined as the geometric mean of the τ_{NM} for the four hardest jets in an event:

$$T_{NM} = \left[\prod_{j=1}^{4} \left(\tau_{NM} \right)_j \right]^{1/4}. \tag{3.7}$$

The more jets with substructure in an event, the more jets with a small τ_{NM}, resulting in a smaller value of T_{NM}. The geometric mean is less sensitive to the presence of a single

[3] Ensuring that the τ_{NM} variables are infrared and collinear (IRC) safe [72] is important for the implementation of our proposed search. $\tau_{N(N-1)}$ is IRC safe if applied to a jet with N hard prongs, which is ensured by requiring a lower bound on $\tau_{(N-1)(N-2)}$. While the results presented here do not include this requirement, we have verified that they are not significantly changed by a naive application of the IRC safety conditions.

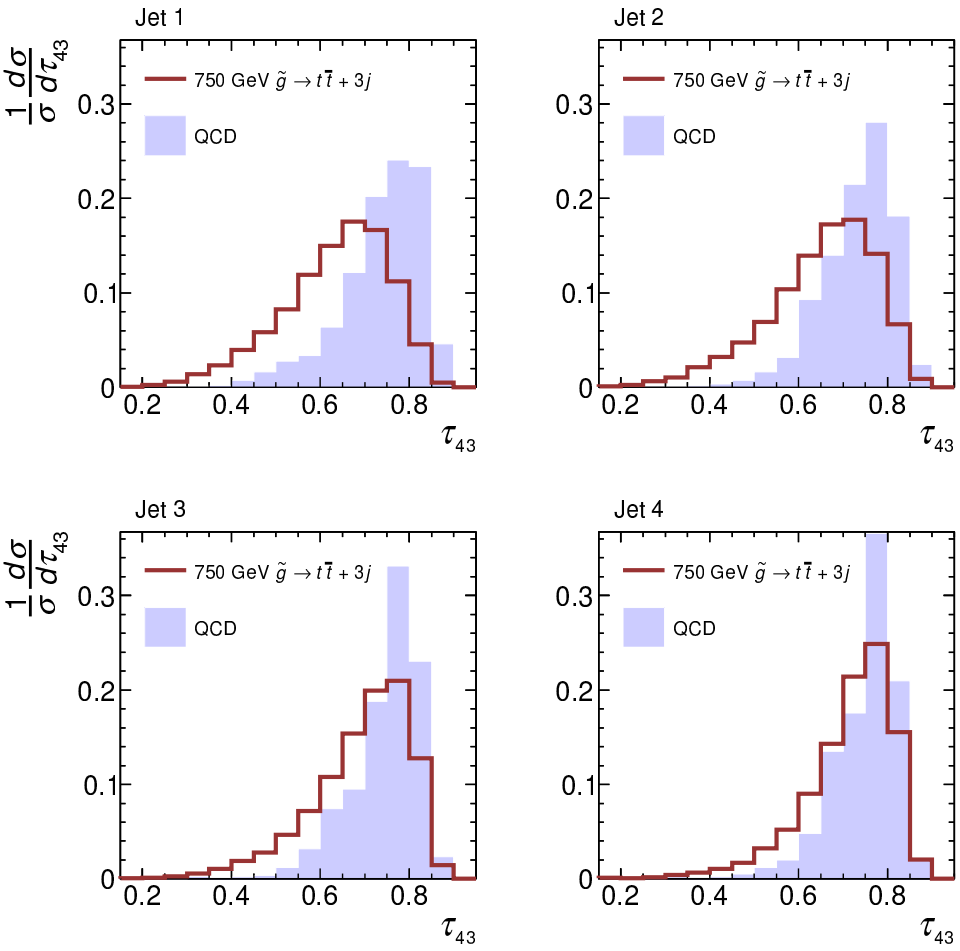

Figure 3.4: Normalized distributions of τ_{43} for background and a signal example. Each plot shows the normalized distribution before a cut on M_J. The signal (red solid line) is pair production of a 750 GeV gluino with $\widetilde{g} \to t\,\bar{t} + 3\,j$. The solid blue histogram is for the QCD background. Each panel is the distribution for the j^{th} jet; the order is by decreasing p_T. Note that the top and electroweak backgrounds are subdominant and are not shown here.

high τ_{NM} in an event than the arithmetic mean. In particular, the arithmetic (geometric) mean tends to result in slightly larger S/B ($S/\sqrt{B}$) than the geometric (arithmetic) mean. This leads to a mild improvement in the reach when using the geometric mean. We also explored placing cuts on combinations of the τ_{NM} for the single two hardest jets; this does not lead to the same level of discriminating power because the amount of substructure is not necessarily correlated with the hardness of a jet. As discussed in Sec. 3.2.1, two jets

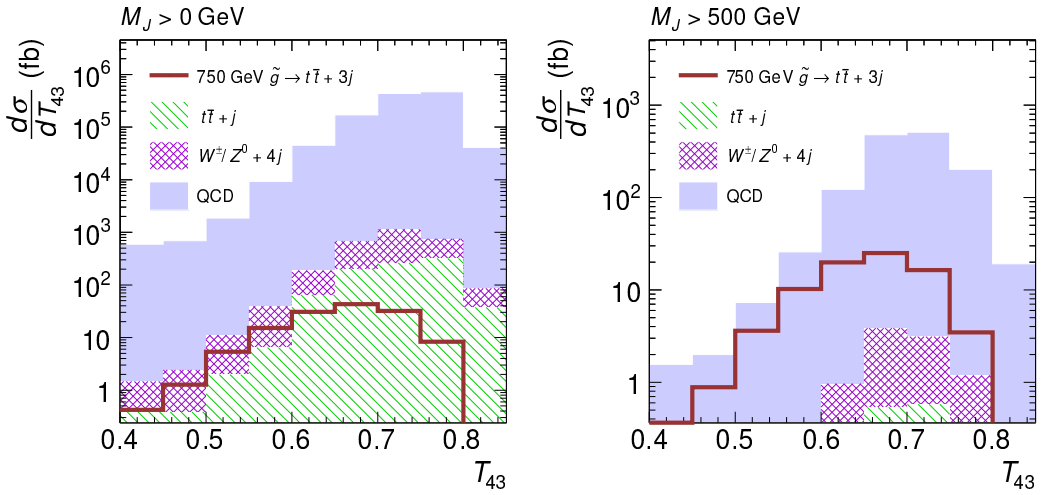

Figure 3.5: Distributions of T_{43} for backgrounds and an example signal, with $M_J > 0$ (left) and $M_J > 500\,\text{GeV}$ (right). The signal (red solid line) is pair production of a 750 GeV gluino with $\widetilde{g} \to t\,\bar{t} + 3\,j$. The stacked histogram is for background (QCD in solid blue, $W^{\pm}/Z^0 + 4\,j$ in hatched magenta, and $t\,\bar{t} + j$ in striped green). A cut on $T_{43} \lesssim 0.6$ helps to distinguish signal from background, after requiring $M_J > 500\,\text{GeV}$.

with equivalent p_T can have a different mass depending on whether the mass arises from accidental substructure or hard-emission.

Figure 3.5 illustrates the distributions of T_{43} for backgrounds and the signal example with $\widetilde{g} \to t\,\bar{t} + 3j$. For this topology, many of the signal fat jets often have four or more subjets, which drives down T_{43} relative to that for the backgrounds. This is evident, for example, in Fig. 3.1 where the signal event has $T_{43} = 0.45$ compared to 0.73 for the QCD event. As Fig. 3.5 shows, after a cut on the total jet mass (right panel), the ratio of signal to background improves relative to no total jet mass cut (left panel). The right panel suggests that the signal and background can be distinguished by applying an additional cut $T_{43} \lesssim 0.6$. We demonstrate the efficacy of this strategy in the following section when we estimate the sensitivity to the signal topologies in Fig. 3.2.

3.3 Analysis Strategy

Having presented the individual components of our analysis, we now combine them and present the complete search strategy. To illustrate the effectiveness of this approach, we compute expected limits for the three different RPV gluino decay chains in Fig. 3.2. Of course, our proposal is quite general and can be applied to any high-multiplicity final-state.

3.3.1 Event Generation

We begin by briefly describing the generation of signal and background events. Sec. 3.5 contains a more detailed description of the detector mockup and Monte Carlo validation.

QCD is the dominant background for a multijet signal with no missing energy. `Sherpa` 1.4.0 [14, 73–76] is used to generate and shower ~ 400 million inclusive $p\,p \to n\,j$ events, where $n \in (2, \ldots, 6)$. Matrix elements for up to 6 partons are generated, which are then matched to the parton shower using the CKKW procedure [77]. All Sherpa events are generated using the default CTEQ 6.6 parton distribution function [78] and include the effects of underlying event. We generated a sample of weighted events in order to increase the statistical power of our finite sample. The Monte Carlo error, ϵ_{MC}, after cuts is

$$\epsilon_{\mathrm{MC}} = \frac{\sqrt{\sum_i w_i^2}}{\sum_i w_i}, \tag{3.8}$$

where w_i is the weight of the i^{th} event in the sample. We verify that the Monte Carlo error is less than the systematic error for the signal regions of interest.

For consistency, `Sherpa` is also used to generate additional subleading background contributions. In particular, we generate ~ 25 million matched and weighted $t\,\bar{t} + n_t\,j$ events, where the tops are forced to decay hadronically. We also simulate ~ 25 million matched and weighted data sets for each electroweak background: $W^+ + n_W\,j$, $W^- + n_W\,j$, and $Z^0 + n_Z\,j$, where the gauge bosons are forced to decay to quarks. Here, $n_t \in 0, 1$ and n_W, $n_Z \in 1, 2, 3, 4$. Table 3.1 shows that these non-QCD backgrounds are subdominant. This would not be the case if a $\not{E}_T$ cut were also applied.

The matrix elements for gluino pair production are generated in `MadGraph5` 1.4.8.4 [79] for the $\widetilde{g} \to t\,\bar{t} + 3\,j$ topology. Those for the $\widetilde{g} \to t + 2\,j$ and $\widetilde{g} \to 3\,j$ topologies are generated directly in `Pythia` 8.170 [13,80,81], where the RPV gluino is allowed to hadronize before decaying. All three signal topologies are generated using the default CTEQ6L1 PDF set [82, 83] and are showered and hadronized in `Pythia` including the effects of underlying event. Because the gluinos are produced at threshold and decay to several fairly hard jets, it is not necessary to perform matching.

Both signal and background events are passed through our own detector mockup, which only includes the effects of detector granularity. `FastJet` 3.0 [84, 85] is used to cluster events into anti-k_T [11] jets with $R = 1.2$. Variables such as jet mass and substructure are sensitive to soft, diffuse radiation that results from underlying event and pile-up. The ATLAS study in [51] explicitly demonstrated that the mean jet mass for anti-k_T jets with $R = 1.0$ and $p_T > 300\,\text{GeV}$ is constant with respect to the number of pile-up vertices for 35 pb^{-1} of 7 TeV data, after a splitting/filtering procedure is applied. For variable multiplicity fat jets, which is quite typical for accidental substructure, filtering is not the optimal grooming technique because it places a fixed requirement on the number of subjets within the fat jet [22]. Instead, to reduce the contamination due to soft radiation resulting from underlying event, we apply the trimming procedure of [29] to the jets before applying any kinematic cuts. We require any subjets of radius $R = 0.3$ to have a p_T greater than 5% of the fat jet's transverse momentum. This choice of parameters is motivated by a recent ATLAS analysis [50]. We find that trimming eliminates the dependence on the different underlying event models used by the generators.

`Prospino` 2.1 [86] is used to obtain the NLO production cross section for the gluinos. For the QCD background, we use a K-factor of 1.8, obtained by comparing distributions of the generated QCD Monte Carlo with published distributions in [51, 87] (see Sec. 3.5 for details on validation). All other backgrounds are subdominant and our analysis is therefore insensitive to the exact choice of their cross sections. We use the `Sherpa` leading order predictions for these backgrounds.

Requirement	QCD	$t\bar{t}+j$	$W^{\pm}/Z^0+4j$	$\widetilde{g}\to t\bar{t}+3j$	$\widetilde{g}\to t+2j$	$\widetilde{g}\to 3j$
(1) $N_j = 4$	5.8×10^6	4500	1.0×10^4	680	7200	4800
(2) $M_J > 500\,\text{GeV}$	6800	8.4	40	400	990	640
(3) $T_{43} < 0.6$ *or*	180	0.61	1.5	**75**	**110**	(48)
$T_{21} < 0.2$	77	0.047	1.1	(1.7)	(27)	**39**

Table 3.1: Event yields from our Monte Carlo simulation, assuming 5 fb^{-1} of 8 TeV data and taking the gluino mass to be 750 GeV for $\widetilde{g}\to t\bar{t}+3j$ and 500 GeV for the other two topologies. The table shows the number of events after requiring (1) four fat jets with $m_j > 20\,\text{GeV}$ and the appropriate p_T requirements (see text), then (2) a cut on the total jet mass, and then (3) a cut on event-subjettiness for a given choice of T_{NM}. Yields are shown for two different T_{NM} cuts that are optimized for the 18, 10, and 6-parton topologies; the number of events that corresponds to the best choice for this cut is bolded while the non-optimal choices are in parentheses.

3.3.2 Expected Reach

Now, we are ready to compute the expected reach of our analysis. All events are required to satisfy the following criteria. Each event must have at least four fat jets, where the p_T of the hardest jet is at least 100 GeV and the p_T of the next three hardest jets is at least 50 GeV. To reduce contamination of heavy flavor resonances and high-p_T QCD jets with no hard splittings, only jets with $m_j > 20\,\text{GeV}$ are considered. To further reduce QCD and $t\bar{t}$ background contributions, each event must have at least 500 GeV of total jet mass, M_J. Finally, a cut is placed on event-subjettiness, T_{NM}. The cuts for M_J and T_{NM} were selected to maximize significance, while ensuring that the Monte Carlo error remained below the systematic error. This requirement imposes a significant limitation on our ability to fully optimize the search and is the reason we only present one set of cuts. Table 3.1 summarizes the cut efficiencies on signal and background.

To determine the expected reach for the three topologies in Fig. 3.2, we assume that the probability of measuring n events is given by the Poisson distribution with mean $\mu = B+S$, where B and S are the number of expected background and signal events, respectively. The

probability of measuring up to N_m events is

$$P\left(N_m|\mu\right) = e^{-\mu}\sum_{n=0}^{N_m}\frac{\mu^n}{n!}. \tag{3.9}$$

This expression assumes that there is no uncertainty in the value for B. In the presence of a systematic uncertainty $\epsilon_{\rm sys}$, Eq. (3.9) must be convoluted with the probability distribution of B, which we assume is log-normal because $B \geq 0$:

$$P_{\rm sys}\left(N_m, S, B\right) = \int_0^\infty {\rm d}x\ P\left(N_m|S+x\right)\cdot \ln\mathcal{N}\left(x\right), \tag{3.10}$$

where $\ln\mathcal{N}(x) = \frac{1}{x\sqrt{2\pi}\epsilon_{\rm sys}}\exp\Big[-\frac{(\ln x - \ln B)^2}{2\epsilon_{\rm sys}^2}\Big]$. Note that as $\epsilon_{\rm sys}\to 0$, the log-normal distribution becomes a delta function centered at B and Eq. (3.10) reproduces the standard result for a Poisson distribution. To obtain the expected limit on the signal cross section, we solve Eq. (3.10) for S assuming that $N_m = B$ and $P_{\rm sys} = 0.05$ (95% exclusion). We find that the expected limits are not sensitive to the distribution function chosen for B; a Gaussian distribution gives essentially the same result.

An ATLAS analysis of the full 2011 dataset reported a jet mass scale systematic uncertainty of $\sim$ 4–8% (depending on jet p_T) for anti-k_T trimmed jets with $R = 1.0$ [50]. For four fat jets, this gives at most a 16% systematic uncertainty. To be conservative and to account for additional sources of systematic effects (*e.g.* jet energy scale), we take $\epsilon_{\rm sys} = 20\%$ when computing sensitivities.

We begin by considering gluino pair production with $\widetilde{g}\to t\,\bar{t}+3\,j$. This topology can yield up to 18 partons when the tops decay hadronically. For this final state, the T_{43} event-subjettiness variable is most effective. For a 750 GeV gluino, a cut of $T_{43} < 0.6$ increases S/B from 0.06 to 0.42, and $S/\sqrt{B}$ from 4.9 to 5.6 as seen in Table 3.1. Figure 3.6 shows the expected reach for 5 fb^{-1} of 8 TeV data. The gray line is the NLO gluino pair-production cross section, as evaluated by `Prospino`. The dashed red line shows the expected limit when all cuts are applied, except that on event-subjettiness. With the additional cut on T_{43}, the expected limit improves by $\sim$ 350 GeV, as illustrated by the solid red line. Requiring jets with accidental substructure significantly extends the reach beyond a search that relies on total jet mass alone.

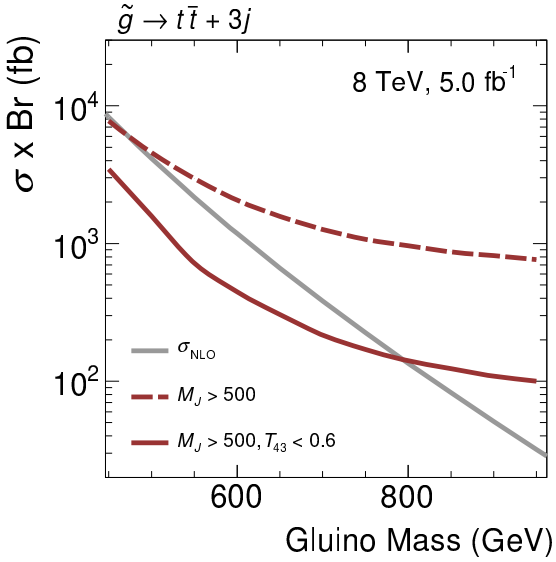

Figure 3.6: The 95% expected exclusion curves for the $\widetilde{g} \to t\,\bar{t} + 3\,j$ topology at the 8 TeV LHC with 5 fb^{-1} of data. The solid grey curve is the NLO prediction for the gluino pair production cross section computed using `Prospino`, the dashed red curve is the expected exclusion including all cuts except the one on event-subjettiness, and the solid red curve is the exclusion when $T_{43} < 0.6$ is imposed. A systematic error $\epsilon_{\text{sys}} = 20\%$ is assumed for the background prediction. Cutting on event-subjettiness improves the reach by ~ 350 GeV.

Event-subjettiness is an effective variable for other RPV gluino decay chains. However, as the number of hard partons decreases, the signature of accidental substructure becomes more subtle. Consider the middle diagram of Fig. 3.2 where $\widetilde{g} \to t + 2\,j$. The 8 TeV, 5 fb^{-1} expected limits on this final state are extended from 400 GeV to 600 GeV when $T_{43} < 0.6$ is required in addition to a jet mass cut. For a 500 GeV gluino, cutting on substructure improves the signal to background ratio from 0.14 to 0.61 as seen in Table 3.1. Due to the smaller number of partons, the improvement in significance is not as dramatic as for the $\widetilde{g} \to t\,\bar{t} + 3\,j$ topology described previously. Here, the main advantage of cutting on substructure is to increase S/B. This provides a significant improvement because systematic uncertainties tend to drive the sensitivity in the signal region when QCD is the dominant background.

Lastly, we consider the 6-parton topology illustrated in the right-most diagram of Fig. 3.2. Of the three decay modes studied in this work, this has the fewest partons and

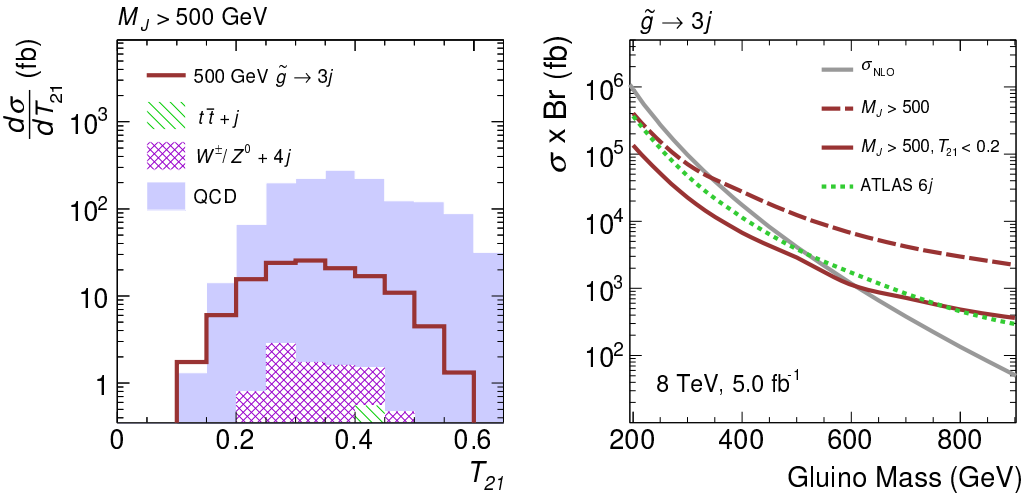

Figure 3.7: The T_{21} distribution for signal and background after requiring $M_J > 500\,\text{GeV}$ (left) and 95 % expected exclusion (right) for the $\tilde{g} \to 3\,j$ topology at the 8 TeV LHC with 5 fb^{-1} of data. **left:** The signal (red solid line) is pair production of a 500 GeV gluino with $\tilde{g} \to 3\,j$. The stacked histogram is for background (QCD in solid blue, $W^{\pm}/Z^0 + 4\,j$ in hatched magenta, and $t\,\bar{t} + j$ in striped green). A cut on $T_{21} \lesssim 0.2$ effectively distinguishes signal from background, after requiring $M_J > 500\,\text{GeV}$. **right:** The solid grey curve is the NLO prediction for the gluino pair production cross section computed using `Prospino`, the dashed red curve is the expected exclusion including all cuts except the one on event-subjettiness, and the solid red curve is the exclusion when $T_{21} < 0.2$ is imposed. For comparison, the green dotted line shows our reproduction of the ATLAS search for this same topology [55]. Our analysis is competitive with the ATLAS reach. A systematic error $\epsilon_{\text{sys}} = 20\%$ is assumed for the background prediction. A cut on event-subjettiness improves the reach by $\sim 250\,\text{GeV}$.

is therefore the most challenging to observe. In particular, T_{21} provides the best discriminating power for this topology. The left panel of Fig. 3.7 shows the T_{21} distribution for background and signal after applying a $M_J > 500\,\text{GeV}$ cut. The background is peaked between 0.35–0.4 and the signal is peaked at 0.25–0.35. The right panel of Fig. 3.7 shows the expected exclusion for the 6-parton final state, assuming 5 fb^{-1} of 8 TeV data. The dashed red line shows that the expected limit is ~ 350 GeV before a cut on event-subjettiness. The expected limit increases to ~ 600 GeV when $T_{21} < 0.2$ is required (the solid red line). As in the last example, the improvement in the limit arises from an increase in the ratio of signal to background after substructure cuts.

The expected reach of our substructure analysis for RPV gluinos is $\sim 600\,\text{GeV}$ and

compares favorably with published limits from CMS and ATLAS. The CMS search for three-jet invariant mass resonances [57] excludes an RPV gluino from 280–460 GeV with 5 fb^{-1} of 7 TeV data. The ATLAS analysis for this final state, published with 4.6 fb^{-1} of 7 TeV data, uses two techniques to provide exclusions [55]. They perform a boosted gluino analysis that makes use of jet substructure and can exclude the gluino in the range 100–255 GeV.[4] A separate "resolved" analysis uses the p_T of the sixth jet (anti-k_T, $R = 0.4$) to separate signal from background, and excludes the gluino from 100–666 GeV.

To provide a direct comparison, we reproduce the ATLAS resolved analysis by reclustering our background and signal into anti-k_T jets with $R = 0.4$ and applying the cuts from [55]. The projected limit for 5 fb^{-1} of 8 TeV data is shown by the green dotted line of Fig. 3.7 and gives a limit of about 550 GeV.[5] This demonstrates that our projected limit, which relies on accidental substructure is competitive to that from the ATLAS resolved analysis.

To emphasize the effectiveness of our approach, we also performed a naive comparison between our method and the ATLAS resolved jet analysis of [55] as applied to the $\widetilde{g} \to t\,\bar{t}+3\,j$ topology. The ATLAS search is not optimized for this signal; in particular, for this topology relying on b-jets and/or leptons may be a more effective strategy. However, it provides a rough guide for a small-radius jet (with $R \sim 0.4$) analysis that one might consider when searching for this multitop topology. We find that there is no bound on the gluino mass for the 6-jet cuts proposed in [55]. In principle, the signal region could be extended to a larger jet count. In that case, however, background estimation can be quite challenging. On the other hand, the accidental substructure analysis outlined in this chapter is broadly applicable to signals with different jet multiplicities.

[4] The recent theory work in [56] finds that the limit on boosted RPV gluinos can be increased by searching for a peak in the jet mass spectrum.

[5] Note that our expected limit of 550 GeV is weaker than that in [55], although it does fall at the edge of the published 1-sigma uncertainty. We can reproduce their limit if we take a K-factor of 1.0 for the QCD background. For consistency with the validation plots from Sec. 3.5, we use the more conservative 1.8 K-factor for Fig. 3.7.

3.4 Conclusion

In this chapter, we introduced the concept of accidental substructure and illustrated its usefulness in searches for high-multiplicity final states and no missing energy. Accidental substructure arises because there is a high likelihood that several final-state partons will be clustered together in the same large-radius jet. These final state partons need not have originated from the same parent particle. QCD is the dominant background. Having several partons in a QCD event that undergo a large-angle, hard splitting is rare enough to make accidental substructure a useful discriminator.

We analyzed three RPV gluino decay topologies with as many as 18, 10, and 6 partons in the final state. The requirement that the total jet mass be greater than 500 GeV, in conjunction with a cut on event-subjettiness, proved to be very effective. We found projected limits of $\mathcal{O}(800\,\text{GeV})$ for the $\widetilde{g} \to t\,\bar{t} + 3\,j$ topology, $\mathcal{O}(600\,\text{GeV})$ for the $\widetilde{g} \to t + 2\,j$ topology, and $\mathcal{O}(600\,\text{GeV})$ for the $\widetilde{g} \to 3\,j$ final state with 5 fb^{-1} of 8 TeV data. These projections assume a 20% systematic uncertainty and a conservative K-factor for the normalization of the QCD background. Our goal was to illustrate the general applicability of a search using accidental substructure and we expect that many aspects of this analysis can be further optimized. One possibility, for instance, is to use a neural network to select the appropriate N-subjettiness variables to include in the evaluation of event-subjettiness. Also, we have not explored how the sensitivity of the search depends on jet radius.

In the case of the 6-parton final state from RPV gluino decays, our expected limit is comparable to that set by the ATLAS small-radius jet analysis [55]. Determining the normalization of the QCD background for a 6 (or more) small-radius jet signal is challenging. As a result, it is important to have a complementary search with independent systematics. Our accidental substructure search is one possible example and is, in addition, sensitive to a broader array of signals than the ATLAS search. In particular, its sensitivity only improves as the number of final-state partons increases, as we showed for the 10 and 18-parton final states.

Events with many tops can lead to many jets in the final state (the scenario we consider here), but other decay channels can give leptons and $\not{E}_T$. Analyses that tag on a lepton and several b-jets can be sensitive in these cases [88]. We also expect our reach to improve significantly when b-tags are included [89]. Alternatively, the total energy S_T may be useful; while it provides the greatest discriminating power in black hole searches [90, 91], the S_T cut must be above several TeV to adequately reduce the multijet background. Tagging on a lepton in addition to six or more jets, could allow an S_T cut down to ~ 1 TeV [92].

The search we proposed here is complementary to these types of analyses. We expect that its potential reach will only increase by adding additional handles. For example, we find that naive cuts on jet mass and event-subjettiness lead to a limit on $\widetilde{g} \to t\,\bar{t} + \not{E}_T$ that is only slightly weaker than the current bounds from CMS and ATLAS. Adding a lepton, a b-tag and/or a small cut on $\not{E}_T$ could make the search even more powerful.

A significant advantage of using fat jets to study final states with many partons is that it is compatible with data-driven determinations of the QCD background. Mapping out the phase-space of high multiplicity QCD with Monte Carlo is currently not possible. For a fat jet analysis, one can use a dijet sample to map out distributions of the internal structure of the jets and to obtain templates for jet mass and substructure as a function of the jet kinematics. Under the mild assumption that the correlations between fat jets are small, one only needs to predict the phase space distribution of the four fat jets, while the internal properties of each fat jet can be modeled using the template functions derived from the dijet events. This simple algorithm allows an extrapolation of the QCD contribution to the four fat jet signal region.

The possibility of using a jet's internal structure to learn about its origin provides exciting opportunities for new physics searches at the LHC. Although jet substructure has only been used for boosted signals thus far, this work demonstrates that it is also applicable in the non-boosted regime. We have shown that accidental substructure provides a robust and powerful new paradigm for new physics searches at the LHC, complementing and extending the reach of current analyses.

3.5 Simulation Details and Validation

In this section, we discuss the details of our simple detector mockup and provide validation plots comparing our QCD Monte Carlo to a number of public distributions from ATLAS. We extract a K-factor to normalize our QCD sample and demonstrate that our Monte Carlo reproduces the measured shapes of substructure and jet mass distributions to reasonable accuracy.

We simulate detector granularity by clustering stable, visible generator-level particles into $\eta \times \phi$ cells of size 0.1×0.1. Electrons, muons, and photons are kept if they fall within $|\eta| < 2.5$, while all other particles are kept if they fall within $|\eta| < 3.0$. Each calorimeter cell is assigned a light-like vector with energy equal to the sum of all particle energies contained therein. `FastJet 3.0` clusters these four-vectors into anti-k_T jets and computes N-subjettiness for the resulting jets using the "min_axes" algorithm, implemented in the N-subjettiness plugin of Thaler and Van-Tilberg [32,37]. Note that leptons are included in jet clustering and when calculating substructure variables. A jet is removed if it is within $\Delta R < 0.2$ of a lepton and its p_T is less than twice the lepton's p_T.

We validate our QCD Monte Carlo by comparing against published kinematic and substructure distributions. No published 8 TeV substructure results are currently available, and so we compare against the published 7 TeV ATLAS results [51, 55, 87]. A weighted sample of $p\,p \to n\,j$, where $n \in (2, \ldots, 6)$, is generated in `Sherpa 1.4.0`. Our 7 TeV sample consists of ~ 50 million events and is generated with the same settings as our ~ 400 million event 8 TeV Sherpa sample, described in Sec. 3.3.1.

To validate the shape of the jet mass and substructure distributions, we follow the analysis in [51] and compare to the unfolded distributions. Particles are clustered into anti-k_T jets with $R = 1.0$. The resulting jets are divided into four equally-spaced p_T bins from 200 to 600 GeV. The jet mass (τ_{21} and τ_{32}) distributions are shown in the top (bottom) of Fig. 3.8 for $p_T \in (200, 300)$. The Monte Carlo predictions are well within the error bands quoted by ATLAS. We checked that the `Sherpa` results for the higher p_T bins, not shown

here, also match the ATLAS results.

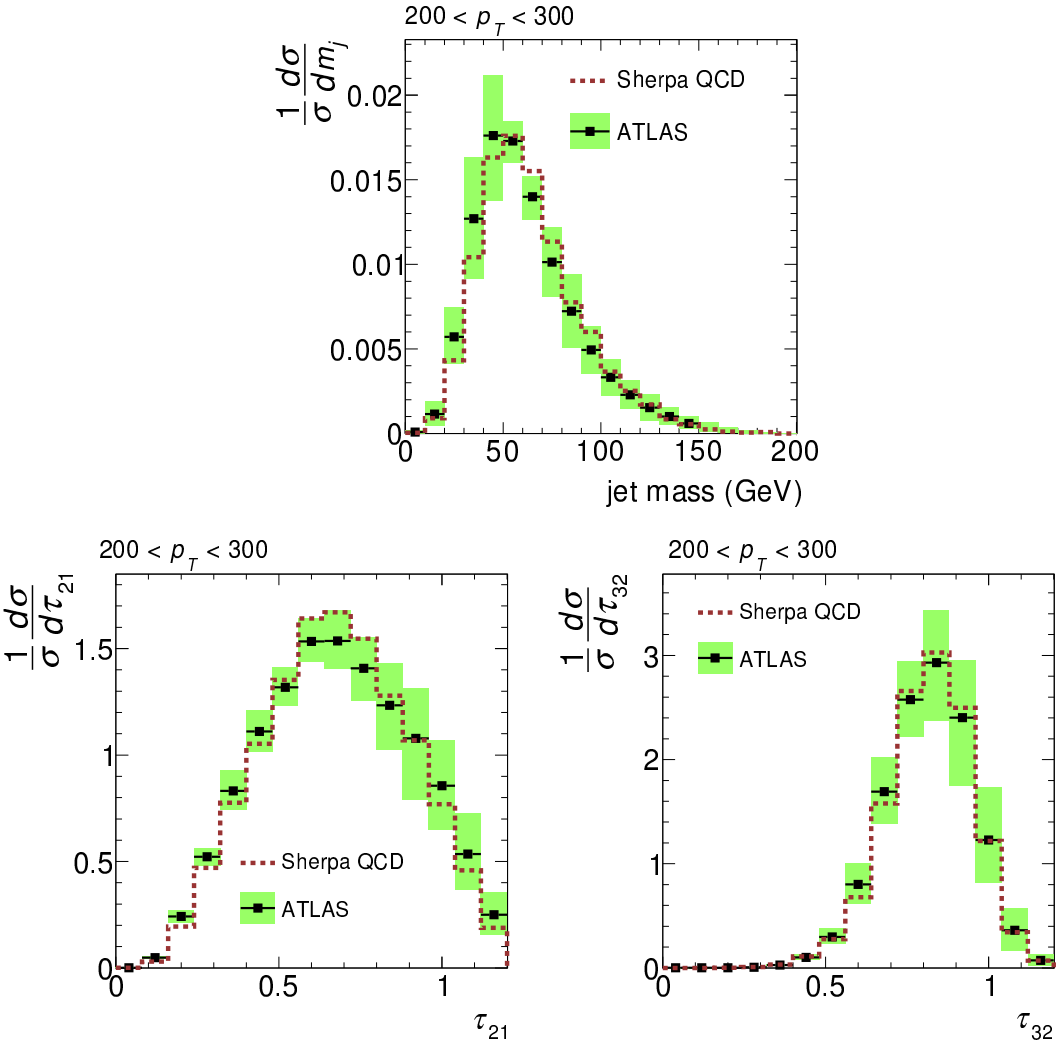

Figure 3.8: Jet mass (top) and N-subjettiness (bottom) comparisons between the `Sherpa` QCD prediction [dotted red] and the ATLAS results [black rectangle] of [51]. The green band is the combined statistical and systematic error in the ATLAS measurement including the uncertainty from the unfolding procedure.

`Sherpa` outputs a leading order (matched) cross section of $\sigma_{\text{QCD}}^{\text{Sherpa}} = 9.6\times10^9$ fb. Because this cross section is enhanced by loop effects, we must find the proper normalization, or K-factor, for the QCD background:

$$\sigma_{\text{QCD}} = K \times \sigma_{\text{QCD}}^{\text{Sherpa}}. \tag{3.11}$$

Using the reported 2-jet inclusive cross-section in [87], we obtain a K-factor of $\sim$ 1.3. Comparing to the 6^{th} jet p_T distribution in [55], we obtain a K-factor of 1.8. Furthermore, by comparing the normalization of the jet mass, τ_{21} and τ_{32} distributions in [51] we obtain a K-factor of 1.8. To be conservative, we assume a K-factor of 1.8 in this work.

Chapter 4

New Physics in Displaced Higgs Decay

4.1 Introduction

Until recently, the Higgs sector was one of the great unknowns in our current understanding of particle physics, and the primary target of the Tevatron and Large Hadron Collider (LHC) programs. The higgs boson discovered at the LHC by the ATLAS and CMS experiments [3, 93] has, so far, been measured to be consistent with a Standard Model (SM) Higgs boson [94, 95]. However, the systematic uncertainties in the measurements still allow for beyond the SM coupling to new physics. In particular, it could have mixing with a singlet, non-standard couplings to the fermions, or other exotic decays. If one assumes a Higgs with SM couplings except additional decay channel to new particles, a branching ratio as large as 20% can be accommodated given the 2012 LHC data [96, 97].

In this article we address an exotic Higgs decay mode that would have escaped existing search strategies. We consider the possibility [98] (see also [99,100] for closely related work) that the Higgs boson h decays to two spin-zero neutral particles X, and the X decays in turn to $b\bar{b}$ with a displaced vertex. More specifically, we will consider the case where the lifetime τ_X of the X puts its decay at a distance from the collision point of order millimeters to a

few centimeters, so that the decay vertex remains within the LHC beampipe. Searches for related signatures have also been made in D0 and ATLAS. In D0, the typical decay to two $b\bar{b}$ pairs in the several to 20 centimeter range has been studied and weakly constrained [101]. In ATLAS, strong limits on final states with a muon and multiple displaced jets have been obtained [102]; however, as the model considered involves an R-parity-violating neutralino decay into a muon and hadrons, the transverse momentum of the muon was required to be higher than 50 GeV/c, which is unlikely to result from the semileptonic decay of the bottom quark used in our model.

It is sometimes argued that searches of this type are not so well-motivated, because the chance of the X having a lifetime that allows for decays inside the detector is low. However, there are both theoretical and experimental considerations in favor. First, long-lived particles are less rare in models [65–67, 98–100, 103–109] than is commonly assumed. In hidden valley models (see [110], for instance), there may be not one but many new particle states with a wide variety of lifetimes, similar to the case of QCD, and this plenitude makes it more likely that one of these particles will have a detectable displaced decay. Second, decays of such particles have such limited SM background that in principle only a few such events might suffice for a discovery, so even a small branching fraction for such particles may lead to a discovery opportunity. That said, detector backgrounds can be a serious issue, and event triggering and reconstruction may be an even larger one if the lifetimes are long enough. Each search strategy has its own features, and some are easier than others.

The Tevatron and LHC detectors were generally not optimized for finding long-lived particles, with the exception of B hadrons, and searches for such particles face numerous challenges. In this chapter we consider the case that, relatively speaking, is the easiest: a search for a new particle that mainly decays before that particle reaches the beampipe. Such decays face little or no background from secondary interactions of hadrons with detector material, and the dominant background is a physics background from real B hadron decays. However, to the extent the X lives longer than the B hadron and is considerably heavier, distinguishing it from SM heavy-flavor backgrounds should be easier. For the specific case

of $h \to XX$, the situation is better still, since there are two X decays per event, and also a mass resonance that may be reconstructable.

The main purpose of this chapter is to suggest a search strategy for $h \to XX$, with X decaying to $b\bar{b}$ before passing through the wall of the beampipe. These events are selected online with a trigger requiring a single muon and two b-jets tagged using an algorithm measuring the secondary vertex displacement. When the mass of the X is heavy, the resulting b-jets typically have low p_T and cannot be triggered efficiently. Hence, we focus on the region where X is light and so the jets from the two b-quarks merge into a single reconstructed jet. Also, as we will describe in this chapter, by merging two b-quarks into one jet, the QCD background can be estimated using data-driven methods. Data-driven techqniues are crucial for low mass signals, where systematic uncertainty can be very large. To extract the signal, we then select X boson candidates by looking for jets meeting a combination of two requirements: first, using the displacement of the individual tracks to identify long-lived particles, and second, using the internal substructure of the jet to further distinguish exotic displaced jets from displaced b-jets. By combining jet substructure with displaced tracks and vertices, it is possible to devise a new exotic jet tagger and propose a data-driven method for estimating the QCD background. Using our technique, it is demonstrated that new long-lived neutral particles originating from a 125 GeV/c^2 Higgs boson may be discovered using 19.5 fb^{-1} of LHC data recorded at $\sqrt{s} = 8$ TeV.

For our studies, we focus on a model with a non-SM Higgs with a mass of 125 GeV/c^2, which then decays into a pair of long-lived neutral bosons X whose mass ranges from 15 to 40 GeV/c^2. For the boson X, we primarily consider the case where the X subsequently decays into $b\bar{b}$. Because of the relatively low mass of the X bosons considered, the $b\bar{b}$ pair is generally reconstructed as a single jet in the detector. We use the anti-k_T [11] algorithm with $\Delta R = 1.0$ in this analysis to capture the hadrons from both b quarks in a single object, which we refer to as a "fat jet". The final topology consists of two fat jets producing a resonance at the expected Higgs mass, with a distinctive two-prong jet substructure in each jet. The predominant background is the QCD production of $b\bar{b}$ pairs. However, since

these pairs are being produced from a single quark, they will tend to have fewer displaced tracks, and will tend to contain only one central hard prong. These properties allow us to differentiate the signal from the much larger background.

The need for using large-radius jets instead of the standard cone size of $\Delta R = 0.5$ is illustrated in Figure 4.1. This figure shows the results of jet reconstruction in a simulated signal sample with $m_H = 125$ GeV/c^2, $m_X = 20$ GeV/c^2, and $c\tau = 2$ mm for two different cone sizes: the standard cone size of $\Delta R = 0.5$, and our enlarged cone size of $\Delta R = 1.0$. In Figure 4.1, we see that even with the standard cone size, in the vast majority of events the $X \to b\bar{b}$ decay is reconstructed as a single merged jet, rather than two separate jets. However, Figure 4.1 shows that the standard cone size is too small to capture all of the radiation from this merged jet, resulting in a significant underestimation of the reconstructed mass. Using a larger cone radius thus offers two advantages: first, the event is nearly always reconstructed with exactly two jets, allowing for more predictable reconstruction; and second, the cone size is large enough to capture all of the merged jet, allowing for more accurate mass reconstruction. We can then use subjet techniques on the merged jets to identify the two constituents.

In this article a variety of proper lifetimes $c\tau$ for the long-lived particle ranging from 1 mm to 10 mm was considered. At very low lifetimes, the displacements of the resulting tracks and vertices become too small to consistently separate the signal events from background, while at high lifetimes the track and muon reconstructions suffer from inefficiencies in the tracking and trigger algorithms, which are not generally designed for highly-displaced particles. However, our simple detector simulation will be unable to take these effects into account and hence we refrain from extending our results beyond 30 mm.

Although our search strategy uses $h \to XX$ as a benchmark for optimization, it is not strongly dependent on the specific initial or final state. Consequently it should be somewhat model-independent, and would be sensitive to a variety of models with two long-lived particles in the events. For example, certain gauge-mediated supersymmetric models with a neutralino [111] decaying in flight to a Z or h might be picked up by our search. One

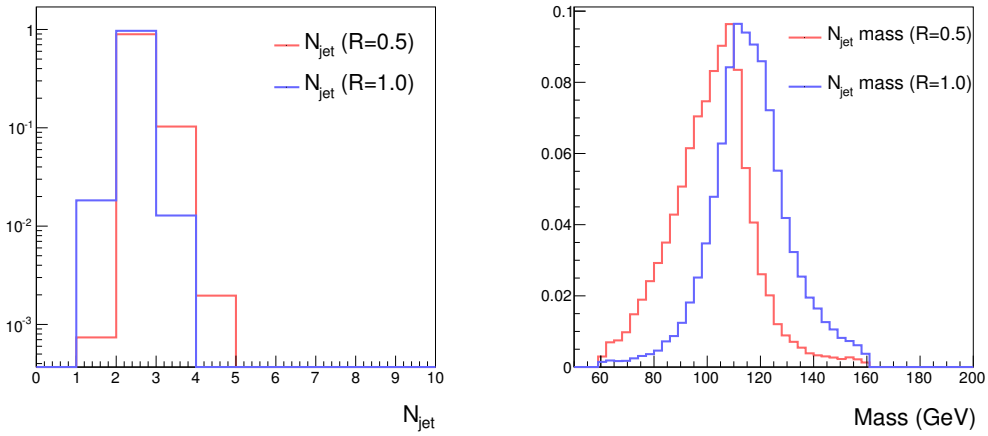

Figure 4.1: Results of jet clustering in simulated signal samples. Left: number of reconstructed jets using the standard cone radius of $\Delta R = 0.5$ (red) and our cone radius of $\Delta R = 1.0$ (blue). Right: Reconstructed two-jet mass for these two different cone radii. The signal model shown is with $m_H = 125$ GeV/c^2, $m_X = 20$ GeV/c^2, and $c\tau = 2$ mm.

point of model-dependence worth keeping in mind is that the heavy-flavor content of the X decay is important for our strategy, as we will base our study on a b-tagger-like trigger.

4.2 Event Generation

At hadron colliders the dominant Higgs production mechanism is via gluon-gluon fusion. In this chapter we study the process $gg \to h \to (X \to b\bar{b})(X \to b\bar{b})$, where the Higgs boson is produced by gluon fusion and then decays into a pair of long lived (pseudo-)scalars which then each decay to a pair of bottom quarks. We consider this in the context of pp collisions at a center-of-mass energy of 8 TeV.

We generate the signal samples for Higgs mass $m_h = 125$ GeV/c^2 and the (pseudo-)scalar mass m_X between 15 and 40 GeV/c^2 with 5 GeV/c^2 steps. Samples were generated for the $c\tau_X$ of the scalar varying within a wide range between 0.1 mm to 30 mm. The signal sample is generated using Pythia 6.4.27 [112]. For the production cross section, we use the NLO cross section for SM $gg \to h$ production, which is 19.3 pb at 8 TeV [113].

The dominant background for this process comes from QCD heavy quark production,

particularly events with one or more $b\bar{b}$ pairs, which represents the most difficult background to remove. Using MadGraph 5 v1.5.7 [79], we generated a sample of 500 million $b\bar{b}$ events matched up to four jets (including $b\bar{b}b\bar{b}$ and $b\bar{b}c\bar{c}$), and showered them through Pythia [112]. Matching is done using the MLM prescription [114]. In order to account for effects that may not be fully modeled in the simulation, a K-factor of 1.6 is obtained by generating another QCD $b\bar{b}$ sample at 7 TeV and reproducing the CMS analysis published in [115] (see Section 4.9 for details and discussion on effects from fake b-tags). We used the CTEQ6L1 PDF for both the signal and the background [82].

To simulate particle flow jets at CMS, the stable particles (except neutrinos) are clustered into large anti-k_T [11] jets with a cone size of $\Delta R = 1.0$ using `FastJet` 3.0.2 [85]. Because our jets use an anti-k_T algorithm with a large cone size to capture as much of the $b\bar{b}$ decay as possible, they are more susceptible to underlying event and pileup effects. In order to overcome these issues, we use jet trimming with $R_{\text{trim}} = 0.3$ and $f_{\text{cut}} = 0.05$ [29]. The resulting jets are then smeared using the momentum resolution given in [116] [1] . To simulate the detector response in the tracker, we associate a track to each charged final state particle with $p_T > 1$ GeV/c. The production vertex of the track is then smeared by an uncertainty σ_{trk}, extracted from [117]:

$$\sigma_{\text{trk}} = a + \frac{b}{p_T} + \left(c + \frac{d}{p_T}\right)\eta^2 \tag{4.1}$$

$$a = 20.4 \quad b = 56.4 \quad c = -0.11 \quad d = 18.2,$$

where σ_{trk} is in units of μm and p_T in units of GeV/c. To avoid complications in finding the vertex location of our event along the beamline, we do not use any tracking information in the longitudinal direction. The QCD background is validated against published CMS results. For details, see Section 4.9.

[1] The values for jets with a cone size $\Delta R = 0.5$ are used; however, as the measured momentum is relatively unimportant to our analysis, this difference should not have a significant effect.

4.3 Displaced Jet Variables

In the following, we discuss the key variables used for identifying long-lived decays. We postpone the discussion on event selection until Section 4.5, where all the analysis strategies and cuts are listed in detail.

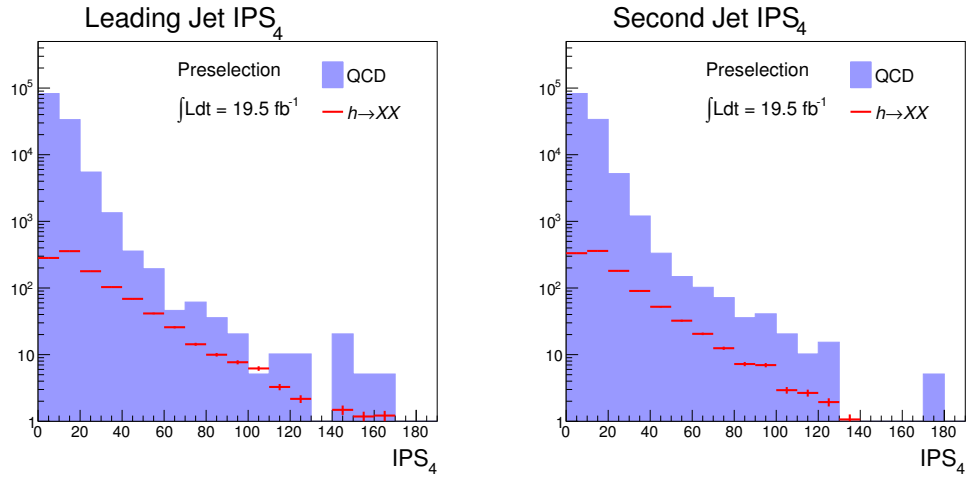

Figure 4.2: Distributions of IPS_4 after preselection. The QCD background is given by the matched $b\bar{b}$ sample, and the signal model shown is with $m_H = 125$ GeV/c^2, $m_X = 20$ GeV/c^2, and $c\tau = 2$ mm. The signal is assumed to have SM gluon fusion production with 100% branching ratio to XX. Left: for the leading jet. Right: for the second-leading jet.

The primary tool we use to measure the displacement of a jet is to examine the displacement of the individual tracks in the jet. For each track, we compute the transverse Impact Parameter (IP) as follows:

$$\mathrm{IP} = \frac{|v_x \cdot p_y - v_y \cdot p_x|}{p_T} \tag{4.2}$$

The computed IP has an associated error $\sigma^2_{\mathrm{IP}} = \sigma^2_{\mathrm{trk}} + \sigma^2_{\mathrm{PV}}$, where σ_{trk} is given by equation 4.1, and $\sigma_{\mathrm{PV}} = 0.025\,\mu$m is the uncertainty associated with the transverse coordinate of the Primary Vertex (PV), as determined in [117]. In an actual detector, the track IP errors are often as large as the measured track IP itself, and it is advantageous to consider the impact parameter significance[2] (IPS) [119]

[2]Our IPS distribution shows good agreement when compared to the CMS results shown in Figure 3 of [118]. For details see Section 4.9.

$$\text{IPS} = \frac{\text{IP}}{\sigma_{\text{IP}}} \tag{4.3}$$

For prompt tracks, the IPS distribution tends to have a strong peak around zero and the spread of the distribution depends on the mismeasurement of the IPS or misalignment. For genuine displaced tracks, the IPS distribution will tend to have a significant tail. Validation of the IPS variable against published data is presented in Section 4.9.

For each jet, we order the associated tracks in decreasing IPS. We then consider the fourth-highest IPS value, denoted by IPS_4. A typical b-jet will tend to only have two displaced tracks, while a displaced $b\bar{b}$ pair will have four, so this variable is expected to have significant discriminating power. Figure 4.2 shows the IPS_4 distributions for signal vs. QCD.

Other variables, such the significance of the decay length of the jet vertex and the fraction of the jet energy carried by prompt tracks, were considered as discriminants for identifying displaced particle decays. However, they did not result in a significant increase in discriminating power, so due to the lack of validation of these other variables and for the sake of simplicity, we do not use these in our analysis.

4.4 Jet Substructure

In this analysis we look for "fat jets" that originate from the decay of the long-lived particle into a $b\bar{b}$ pair, and we expect the "fat jet" to contain a different substructure than jets originating from a single b quark. In order to quantify this substructure, we use the "N-subjettiness" variables defined in [32, 37]. Briefly, one first defines τ_N by fitting N axes to a jet, and computing

$$\tau_N = \frac{1}{d_0} \sum_k p_{T,k} \min\{\Delta R_{1,k}, \ldots \Delta R_{N,k}\}, \tag{4.4}$$

where k runs over the constituents in the jet and d_0 is an unimportant overall normalization factor. τ_N is then minimized over all possible choices of the N subjet axes. τ_N thus shows

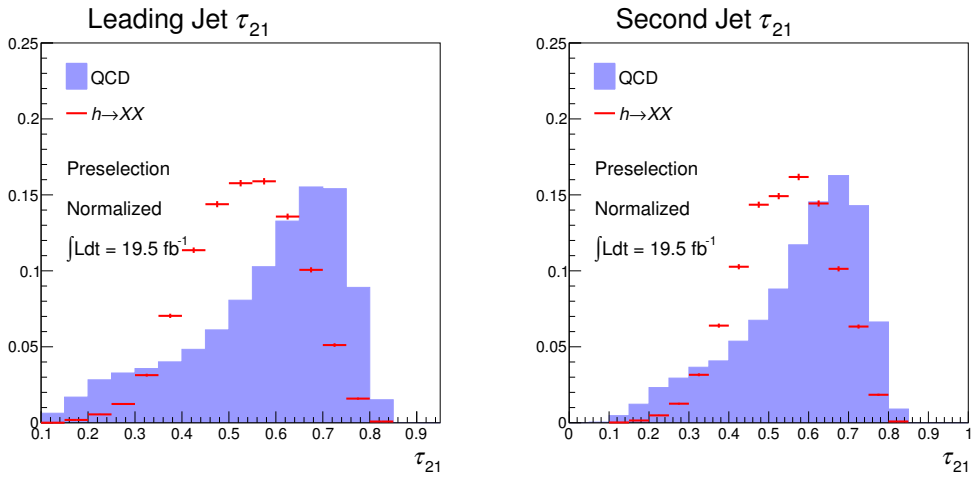

Figure 4.3: Distribution of τ_{21} for the leading jet (left) and the second-leading jet (right) for simulated signal events and $b\bar{b}$ background, for a signal model with $m_H = 125$ GeV/c^2 and $m_X = 20$ GeV/c^2.

to what degree the jet can be viewed as being composed of N individual subjets. For distinguishing jets with two subjets from one, we use $\tau_{21} = \tau_2/\tau_1$. If τ_{21} is close to 0, that indicates that the jet is strongly favored to have two subjets, as we would expect from our signal jets, while a τ_{21} close to 1 indicates that the jet does not have a two-subjet structure, as we would expect from QCD. One can see from Figure 4.3 that the τ_{21} distributions are indeed different between signal and QCD[3] .

4.5 Event Selection

Following the definition of variables of interest to this analysis, we describe the selection criteria devised to select events containing X boson candidates.

4.5.1 Trigger

We simulate one of the High Level Triggers (HLT, purely software-based and with access to the full event information) used in a CMS Higgs search [115]. As it is difficult to achieve a good trigger efficiency and purity with a purely hadronic trigger, we instead focus on events

[3]To combat underlying event and pile-up, jet trimming is applied using $R_{\text{trim}} = 0.3$ and $f_{\text{cut}} = 0.05$

where at least one of the b quarks decays semileptonically to a muon. Thus, we require the events to contain at least one muon with $p_T > 12$ GeV/c and two b-tagged jets with $p_T >$ 40 GeV/c and 20 GeV/c, respectively. Our simulation adopts a slightly simpler method for b-tagging than that used online in CMS, and uses a track counting method [119] which requires a b-tagged jet to have at least two tracks with IPS > 3. This custom selection offers a $\sim$50 % efficiency, comparable to that from CMS. The trigger is fully efficient after preselection.

4.5.2 Selection for $X \to b\bar{b}$

We expect the signature of the $h \to XX \to 4b$ event to be two displaced fat jets, where each displaced fat jet originates from a $b\bar{b}$ pair, and at least one muon produced by the semileptonic decay of a b quark in the event. The selection is applied in two stages. First, we apply a preselection with relatively loose requirements on the displacement of the jets; the primary purpose of the preselection is to eliminate light-flavor background so that only signal and $b\bar{b}$ background remains. The preselection also reduces the correlation between the two jets, allowing us to treat them as uncorrelated. After the preselection is applied, a final selection, using the displacement and the jet substructure, is used to separate the signal from the $b\bar{b}$ background. The various selections, applied sequentially, are described below, and the yields for signal and background are presented in Table 4.1. The preselection consists of the following four requirements:

Cut 1: The event must pass the simulated trigger, as described above.

Cut 2: At least two fat jets, constructed as described previously, satisfying the following quality requirements:

- $|\eta| < 3.0$ and $p_T > 30$ GeV/c
- At least 8 associated tracks per jet

Cut 3: One of the two chosen jets must match to a muon with $p_T > 12$ GeV/c.

Cut 4: Both jets must have $\text{IPS}_4 > 5$.

After preselection, the leading two fat jets are essentially determined to be real b-jets. This reduces the correlation between the two leading jets, which is crucial for the data-driven analysis. Figure 4.4 shows some distributions of the jets after this preselection is applied. Table 4.1 shows the expected efficiency of these cuts in the background and signal simulation.

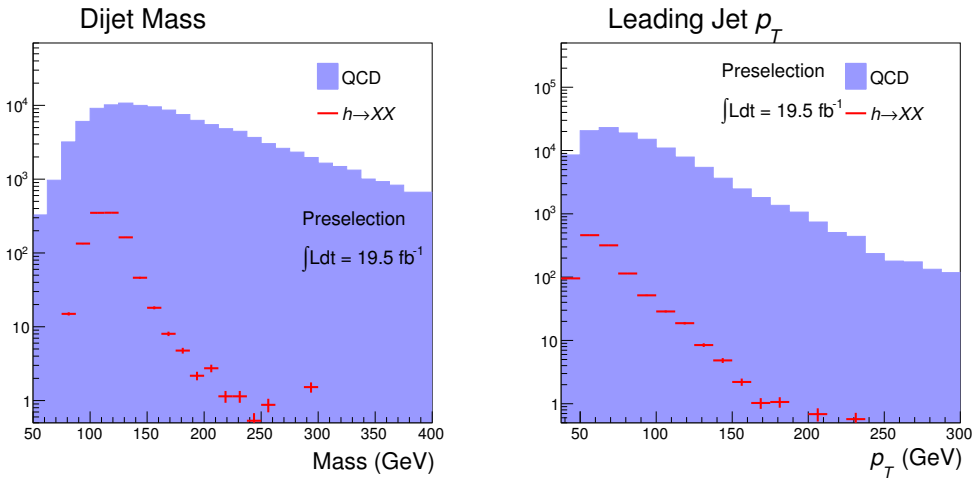

Figure 4.4: Distributions of some kinematic quantities after preselection. Left: m_{jj}, the invariant mass of the two leading jets in the event. Right: p_T of the leading jet in the event. Shown here are simulated signal events and $b\bar{b}$ background, for a signal model with $m_H = 125$ GeV/c^2 and $m_X = 20$ GeV/c^2.

	Background		Signal	
Cut	Number of events	Efficiency (%)	Number of events	Efficiency (%)
Trigger	7.4 x 10^7	—	1.6 x 10^4	—
Jet quality	1.2 x 10^7	15.8	6.7 x 10^3	42.4
Muon match	9.1 x 10^6	78.2	4.7 x 10^3	70.5
IPS_4	2.8 x 10^5	3.1	1.4 x 10^3	28.7
Mass window	6.8 x 10^4	23.8	1.1 x 10^3	80.7

Table 4.1: Efficiency of the various cuts applied in preselection (and the mass window cut). Each row shows the number of events passing the given cut, as well as all of those preceding it, and the relative efficiency of that cut for events which have passed all preceding cuts. All numbers are scaled to the 2012 CMS luminosity of 19.5 fb^{-1}.

In the final selection step, we look for properties of the jets which can be used to separate signal from the $b\bar{b}$ background. In general, the jets originating from our signal model have two key differences from the QCD background: first, they are expected to have more displaced tracks, and for these tracks to be more highly displaced (as the lifetimes of both the X and the b contribute to their displacement); and second, we expect the jets to exhibit substructure arising from the presence of the $b\bar{b}$ pair. After pre-selection, we thus apply stringent requirements on the displaced tracks and jet substructure for both jets using the variables described in Sections 4.3 and 4.4. The particular values used are as follows:

Final Cut 1: Dijet mass between (80,140) GeV/c^2

Final Cut 2: $\text{IPS}_4 > 25$ for both jets

Final Cut 3: $\tau_{21} < 0.65$ for both jets

After the final selection, the QCD background is essentially eliminated. Figure 4.5 shows the mass distribution in the final signal region (except the mass window cut). However, since our cuts are selecting out sharply falling tails of the QCD background, Monte Carlo simulations can become very unreliable. At the LHC, data driven methods must be employed to obtain a reliable background estimate. We propose such a data-driven estimate in the next section.

4.6 Background Estimation

We adopt a data-driven approach to estimate the expected background, in order to minimize the dependence on quantities which may not be well-modeled in the Monte Carlo simulation. We use a standard "ABCD" approach in order to estimate the expected amount of background in the signal region. Specifically, we take advantage of the fact that the two fat jets in an event, as they shower and decay independently, should have uncorrelated values for the displaced track and substructure variables.

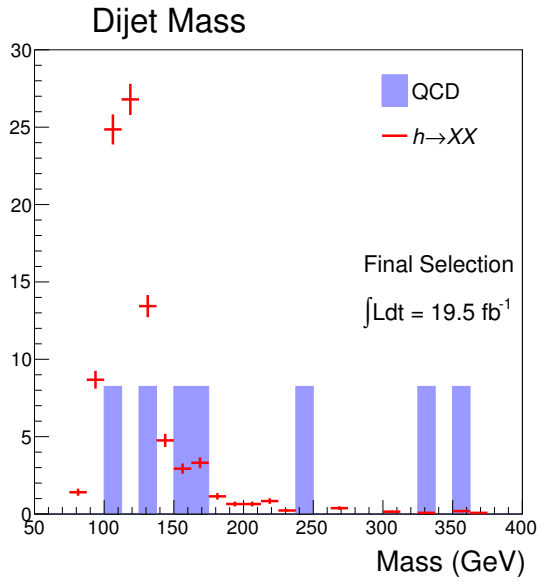

Figure 4.5: Distribution of m_{jj}, the invariant mass of the two leading jets in the event after final selection. All but the mass window cuts are applied. Shown here are simulated signal events and $b\bar{b}$ background, for a signal model with $m_H = 125$ GeV/c^2 and $m_X = 20$ GeV/c^2. The signal is clearly visible as a prominent peak over the background.

We thus define our "signal" region for each individual jet as $\text{IPS}_4 > 25$ and $\tau_{21} < 0.65$, and define our regions (given events that pass our preselection, including the mass window) as follows:

- Region A: both jets fail
- Region B: leading jet passes, second jet fails
- Region C: leading jet fails, second jet passes
- Region D: both jets pass (signal region)

The final background estimate is then obtained from the ratio BC/A. Table 4.2 shows the results of applying this technique to the background and signal simulation. We observe that the final estimate is consistent with the actual number of events in region D in simulation.

Region	Background	Signal
A (fail/fail)	6040 ± 220	22
B (pass/fail)	305 ± 50	47
C (fail/pass)	345 ± 53	38
D (pass/pass)	16 ± 12	77
Final estimate (BC/A)	17.4 ± 4.0	

Table 4.2: The number of events in each region for our ABCD technique, scaled to the 2012 CMS luminosity of 19.5 fb^{-1}. The errors include both the statistical uncertainty (from our limited MC sample size) and the systematic uncertainty derived from comparison to the data sidebands; the latter is the dominant effect.

We can also crosscheck this method in two other ways: first, we can apply the same method but with a different mass window, in order to obtain a sideband selection of events. Using the background simulation, we get consistent results using a mass window of (100,160) or (120,180), although the expected signal in these regions is of course much less.

Another alternative crosscheck is to take advantage of the fact that the IPS$_4$ and τ_{21} variables are relatively uncorrelated,[4] and thus can be used to define another pair of variables for applying the ABCD method. In this case, the statistics in the "B" region are relatively low, thus resulting in a larger systematic uncertainty, so we do not adopt this as our central estimate. However, we obtain an estimate of 20 ± 9 events (statistical uncertainty only), consistent with our previous estimate.

4.7 Results

Applying the efficiency and the expected QCD background numbers shown in Tables 4.1 and 4.2, and using the luminosity collected at CMS in 2012 (19.5 fb^{-1}), we can set limits on the cross-section times branching ratio of the Higgs boson to $X \to b\bar{b}$. The limits are shown in Figure 4.6 and are obtained using CL$_s$ test statistics and assuming a 50% total systematic uncertainty. The systematic uncertainty is conservatively estimated by examining the maximum deviation of the data-driven method when compared to the actual

[4]More specifically, although both of these variables are correlated through the jet momentum, after the preselection criteria and the dijet mass window cut are applied, the variation in the jet momentum is reduced, thus decreasing the correlation between these variables arising from the jet p_T.

number of QCD events in different mass windows (which is limited by our QCD statistics in the higher mass windows). As seen from the figure, for the SM NLO cross-section and a branching ratio of 20%, we can exclude down to $c\tau > 3$ mm for $m_X = 20$ GeV/c^2. The limits for higher m_X are worse due to softer jets and muons. For lower m_X, the tracks become more collimated and the τ_{21} variable becomes less effective. However, a 20% $h \to XX \to b\bar{b}b\bar{b}$ branching ratio can be consistently excluded for $m_X \in (15, 25)$ GeV/c^2 at $c\tau > 3$ mm. Further optimization for different mass points may be possible and we leave a detailed study to the experimental collaborations to properly take detector effects into account.

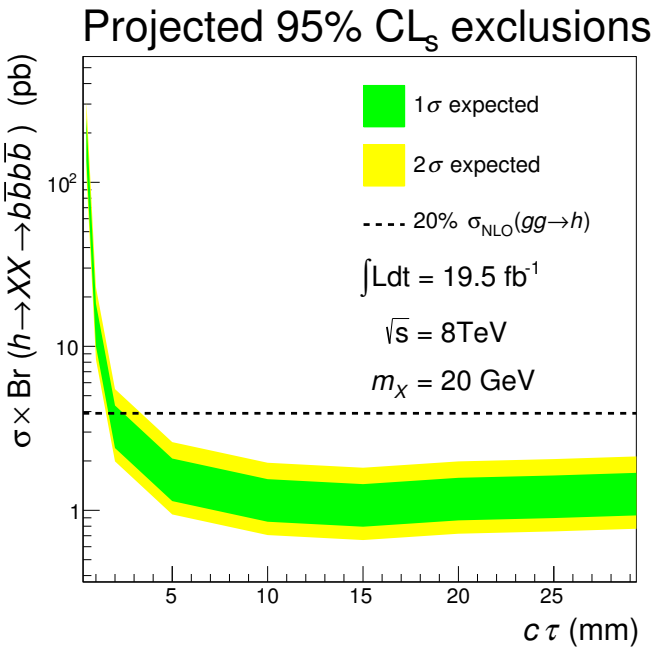

Figure 4.6: Expected limits on the cross-section times branching ratio of the process $h \to XX \to 4b$ given 19.5 fb^{-1} of data, with 50% total uncertainty on the background. Systematic uncertainties on the luminosity and efficiency are not considered.

In Figure 4.7 we also consider the discovery potential for $h \to XX \to 4b$ decay. For a branching ratio of 20%, this new decay mode may be discoverable with the current 19.5 fb^{-1} of 8 TeV LHC data for $m_X = 15$ to 25 GeV/c^2.

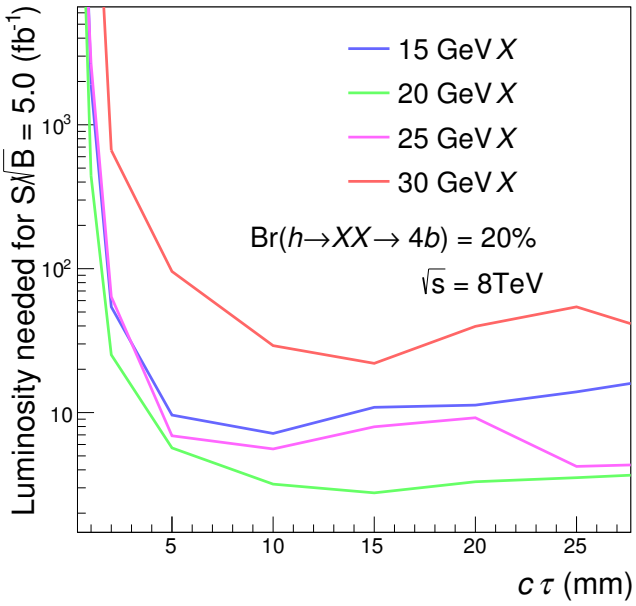

Figure 4.7: Luminosity needed to obtain 5σ significance assuming a 20% branching ratio of $h \to XX \to 4b$. Uncertainities are not included in this plot

4.8 Conclusion

In this chapter we have introduced several powerful kinematic cuts designed to discover a Higgs boson decaying to long-lived neutral particles. The unique features of this channel $h \to XX \to 4b$ are two-fold. First, the highly-displaced vertices resulting from the decay of the long-lived particles, some fraction of which occurs before reaching within the beampipe. The tracks from these vertices will have large IPS. Second, the long lived particles are boosted enough such the $b\bar{b}$ pairs are contained within one "fat jet", removing combinatoric ambiguities and allowing us to take advantage of the jet substructure to distinguish the signal from the QCD background. We have developed a data-driven method to estimate the background and for certain values of the (pseudo-)scalar decay length and masses calculated the expected exclusion (Figure 4.6) and luminosity needed for discovery (Figure 4.7), showing that we have a strong discovery potential in this channel with about 19.5 fb^{-1} of recorded LHC data.

Currently, the primarily limiting factor in this analysis is the trigger selection, as the existing triggers have a relatively low efficiency for the signal considered here. Given the importance of potential new discovery through exotic topologies that include long-lived particles decaying in the silicon tracker, Graphics Processing Unit (GPU) enhancement of the existing High-Level Trigger (HLT) is possible [120]. The proposed new algorithms will allow for the first time the reconstruction of long-lived particles in the tracker system for the purpose of online selection. New ways of enhancing the trigger performance and the development of dedicated custom exotic triggers are the key for extending the reach of physics at the LHC.

As a final note, we re-iterate that this study is optimized on a specific mass point, $m_X = 20$ GeV/c^2. A detailed optimization on the cuts on IPS_4 and τ_{21} could significantly improve the exclusion limits for different X masses. Furthermore, even though we only focused on the $X \to b\bar{b}$ case, our techniques may be sensitive to other channels, such as $X \to \tau^+\tau^-$ or a Higgs boson decaying to a long-lived RPV neutralino χ, which then decays into $\nu b\bar{b}$. With improved triggers for long-lived particles, additional searches for long-lived $X \to gg$ and $X \to qqq$ (for fermionic X) may also be possible. Our search channel also does not have to be limited to a 125 GeV/c^2 Higgs particle. New particles may potentially be discovered through these long-lived decays. We leave a detailed optimization of the different cuts for different decay channels for future work.

4.9 Validations

In this section, we describe how we obtain a K-factor of 1.6 and validate our IPS variables against published results. A separate 7 TeV $b\bar{b}$ sample is generated for this purpose (matched up to four jets). 500 thousand events were generated using MadGraph 5 v1.5.7 with the same settings as those listed in Section 4.2. The final state particles are clustered using anti-k_T algorithm and their momentum smeared with resolution parameters from CMS [116]. We reproduce the CMS analysis in [115] using the quoted b-quark tagging efficiencies and mistag rates. A K-factor of 1.6 is obtained by matching our dijet mass distribution against

Figure 4a in [115]. The resulting distribution is shown in Figure 4.8.

To study the effects of fake b-tags in events without a true b-quark, another 9 million 8 TeV $c\bar{c}$ events were generated using MadGraph 5 v1.5.7 (matched up to 4 jets), and no events passing preselection cuts are found. This suggests that the rate of fake b-tags in our analysis described can be safely neglected. It should be noted that the K-factor obtained from Figure 4.8 also includes the effects of mistags arising from light-quark contamination; since our pre-selection cuts are much more stringent than the analysis in [115], using this K-factor should conservatively include any effects that we might see from fake b-tags, so our ignoring of the light flavor QCD background is justified. The analysis in [115] also indicates that vector boson processes contribute less than 1% of the total background, hence we neglect their contributions to the background as well.

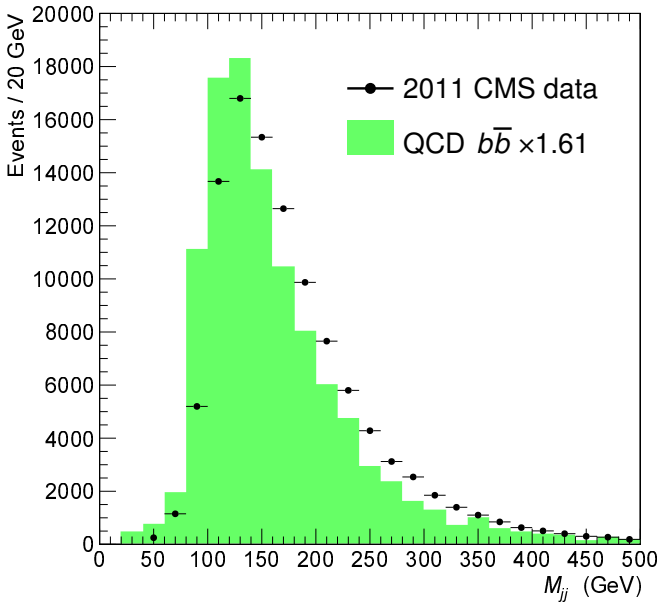

Figure 4.8: The mass distribution of the two leading jets as compared to the CMS analysis in [115]. A K-factor of 1.6 is obtained and serves as a conservative estimate of $c\bar{c}$ and light flavor contaminations.

To validate our displaced jet variables outlined in Section 4.3, we also use our 7 TeV validation sample and compare the IPS distributions to the published results in Figure 3 in [118]. The normalized distributions are shown in Figure 4.9. Modest disagreements are

seen at large IPS. However, the deviations are smaller than our 50% systematic uncertainty. Given the systematic deviations, we also refrain from pushing our IPS_4 cut beyond 25, and our exclusion results are conservative.

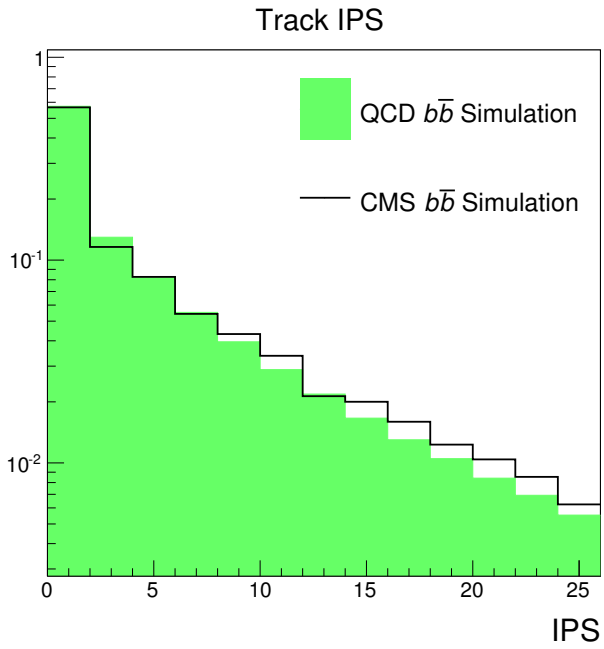

Figure 4.9: The normalized IPS distribution for b-jets when compared to published CMS results in [118].

Chapter 5

New Physics in Semi-visible jets

5.1 Introduction

The existence of dark matter provides one of the strongest motivations for physics beyond the Standard Model, and its discovery is one of the core missions for the Large Hadron Collider (LHC) program. Under the assumption that the dark-matter particle is neutral and stable, it escapes the detector and manifests as missing transverse energy ($\not{E}_T$). The LHC collaborations have developed a comprehensive search strategy to look for signals with significant $\not{E}_T$, accompanied by jets and/or leptons (see *e.g.* [121] for a review). These searches are typically cast in terms of a Simplified Model [122] for supersymmetry or an effective theory of dark-matter interactions [123,124]. Yet if one relaxes the assumption that the dark sector is weakly coupled, a new class of dark-matter signatures emerge that evade this entire suite of analyses. Namely, it is possible that the dark matter has been lurking undercover within hadronic jets. The purpose of this chapter is to propose a straightforward discovery strategy for these "semi-visible" jets.

Semi-visible jets may occur if the dark matter is the stable (or meta-stable) remnant of a more complicated dark sector. The dynamics of non-trivial dark sectors have been explored in many contexts, *e.g.* [65,110,125–137]. In these models, the dark sector contains a dark-matter candidate(s) and possibly new force carriers and/or matter fields. Note that

we are agnostic about how much of the cosmological relic density is accounted for by this dark-matter candidate. Typically, some messenger state exists that couples the dark sector to the Standard Model (SM). If the messenger is accessible at colliders, dark-sector states can be produced, leading to unique signatures such as large particle multiplicities, displaced vertices, multiple resonances, and lepton or photon jets [63, 98, 138–149].

Another possibility is that the final state resulting from strongly coupled hidden sectors may contain a new type of jet object—a semi-visible jet. In this case, the dark matter is produced in a QCD-like parton shower along with other light degrees of freedom that decay hadronically. The result is a multijet+$\not\!\!E_T$ signature where one of the jets is closely aligned with the $\vec{\not\!\!E}_T$. A cornerstone of the standard multijet+$\not\!\!E_T$ searches is to require a minimum angular separation between the jets and $\not\!\!E_T$ to remove QCD background contamination arising from jet-energy mis-measurement [150, 151]. This implies that events containing semi-visible jets have a low acceptance for the currently implemented suite of searches.

To further illustrate this point, Fig. 5.1 compares selected observables for QCD with those for example weakly coupled and strongly coupled dark-matter models. The weakly coupled model is derived from supersymmetric theories and results from pair production of 1.5 TeV scalar quark partners. Each squark decays to a jet and 1 GeV neutral dark-matter particle. The signal from the strongly coupled model, which will be described more fully later, comes from the production of a 3 TeV resonance which then decays to a pair of dark-sector particles that subsequently shower and hadronize, yielding semi-visible jets. Both these examples yield topologies with jets and missing energy. As the left panel shows, the weakly coupled (labeled WIMP) and strongly coupled (labeled semi-visible jet) dark-sector models produce considerable $\not\!\!E_T$, with tails that extend beyond the QCD distribution. However, $\Delta\phi \equiv \min\{\Delta\phi_{j_1\not\!\!E_T}, \Delta\phi_{j_2\not\!\!E_T}\}$, where $j_{1,2}$ are the two hardest jets, is different between these models, as illustrated in the right panel. The $\Delta\phi$ distribution falls relatively steeply for the strongly coupled case, while it remains relatively flat for the weakly coupled scenario. Typical LHC searches require $\Delta\phi \gtrsim 0.4$ [150,151]. For illustration, after requiring $\not\!\!E_T > 500$ GeV and $\Delta\phi > 0.4$, the acceptance of the WIMP (semi-visible) example is ∼40%

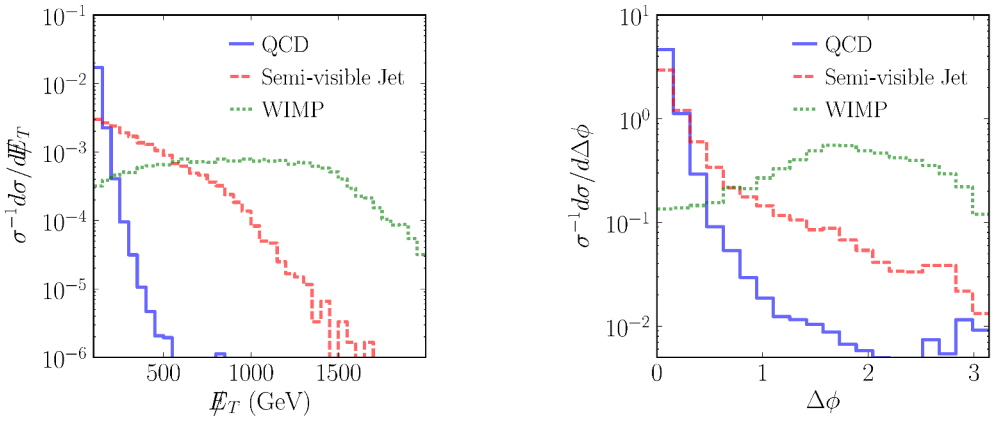

Figure 5.1: *(left)* The distribution of transverse missing energy $\not{E}_T$ for the QCD background (solid blue), as well as the semi-visible jet (dashed red) and WIMP (dotted green) examples. *(right)* The distribution of $\Delta\phi \equiv \min\{\Delta\phi_{j_1\not{E}_T}, \Delta\phi_{j_2\not{E}_T}\}$, where $j_{1,2}$ are the two hardest jets. Typical LHC searches require $\Delta\phi \gtrsim 0.4$ [150, 151].

(1%).

To regain sensitivity to final states containing semi-visible jets, the cut on the angular separation $\Delta\phi$ must be removed. This comes at the expense of an unsuppressed QCD multijet background, which must be eliminated using other techniques. In this chapter, we focus on the case where the dark sector is accessed via a heavy resonance. In such scenarios, one can take advantage of structure in the transverse mass—calculated using the final-state jets and $\not{E}_T$—to distinguish the signal from QCD. The strategy employed is similar to others proposed for semi-visible Higgs decays [152].

5.2 Model

We now introduce example messenger and dark-sector Lagrangians which will enable us to analyze the LHC sensitivity for semi-visible jets. In particular, the example studied below first appeared in the context of "Hidden Valleys" [110]. This example is presented for illustration and concreteness; semi-visible jets will be among the LHC signatures for a vast class of dark-sector models.

The messenger sector is described by a simple phenomenological model for a TeV-scale $U(1)'$ gauge boson. The new leptophobic Z' gauge boson couples to the SM baryon current

$J^{\mu}_{\rm SM}$:

$$\mathcal{L} \supset -\frac{1}{4}\, Z'^{\mu\nu}\, Z'_{\mu\nu} - \frac{1}{2}\, M^2_{Z'}\, Z'_{\mu}\, Z'^{\mu} - g^{\rm SM}_{Z'}\, Z'_{\mu}\, J^{\mu}_{\rm SM}. \tag{5.1}$$

Note that the Z' is treated as a Stueckelberg field—the Higgs sector has been neglected as it is not relevant for the LHC phenomenology discussed below. We also ignore the additional matter that must exist in order to render the $U(1)$ of baryon number anomaly free.

The dark sector is an $SU(2)_d$ gauge theory with coupling α_d and two scalar quark flavors $\chi_i = \chi_{1,2}$ with masses M_i. The scalar quark coupling to the Z' is $g^d_{Z'}$. In general, the couplings $g^d_{Z'}$ and $g^{\rm SM}_{Z'}$ do not have to be comparable; we focus on the case where $g^d_{Z'}$ is large for the Z' to decay frequently into the dark sector.

The $SU(2)_d$ confines at a scale $\Lambda_d \ll M_{Z'}$. A QCD-like dark shower occurs when $M_i^2 \sim \Lambda_d^2$ so that many dark gluons and scalar quarks are produced, which subsequently hadronize. Some of these dark hadrons are stable, while others decay back to the SM via an off-shell Z'. The detailed spectrum of the dark hadrons depends on non-perturbative physics. Nonetheless, some properties of the low-energy states can be inferred from symmetry arguments. There are two accidental symmetries: a dark-isospin number $U(1)_{1-2}$ and a dark-baryon number $U(1)_{1+2}$, where "1" and "2" refer to the χ_i flavor index. For example, the mesons $\chi_1^\dagger\chi_1$ and $\chi_2^\dagger\chi_2$ are not charged under either of these symmetries, and are thus unstable. The other mesons ($\chi_1\chi_2^\dagger$, $\chi_1^\dagger\chi_2$) and baryons ($\chi_1\chi_2$, $\chi_1^\dagger\chi_2^\dagger$) are charged under $U(1)_{1-2}$ and $U(1)_{1+2}$, respectively, and are stable.

By construction, this phenomenological model only contains terms and interactions that have a direct impact on the jet distributions and on the missing transverse energy. The strength of the dark shower, parametrized by α_d, plays a critical role. The coupling α_d controls how many dark hadrons are emitted in the shower as well as their p_T distributions, which has a direct and measurable impact on the jet observables. In addition, the mass scale of the dark quarks is relevant, affecting the jet masses.

The number of dark-matter particles produced in the shower impact $\vec{\not{E}}_T$. It is useful to parametrize these effects in terms of the quantity

$$r_{\rm inv} \equiv \left\langle \frac{\#\text{ of stable hadrons}}{\#\text{ of unstable hadrons}} \right\rangle. \tag{5.2}$$

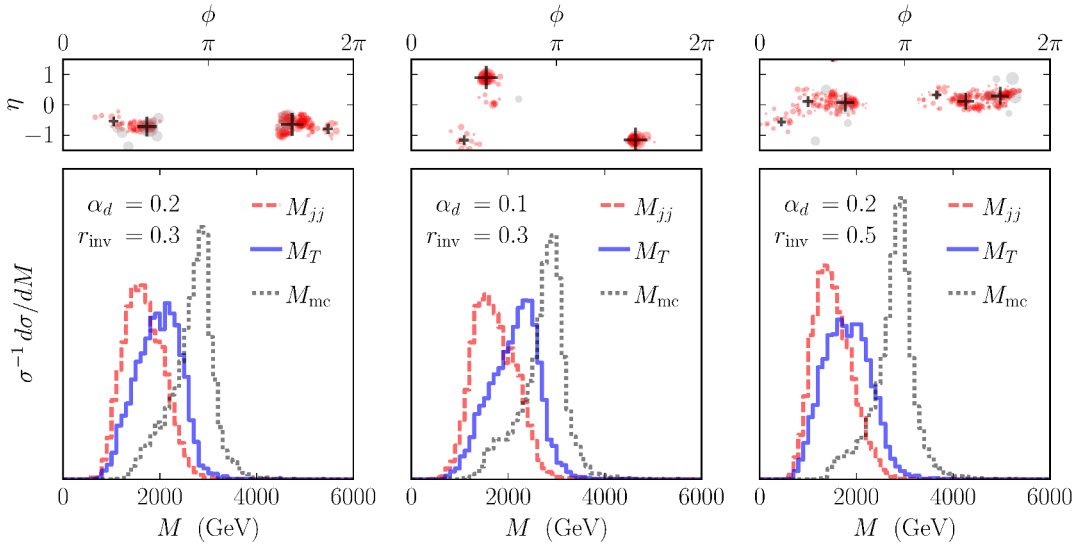

Figure 5.2: Mass distributions for the benchmark model in Table 5.1, for various α_d and $r_{\rm inv}$. M_{jj} is the mass of the two large reclustered jets, M_T the transverse mass, and $M_{\rm mc}$ the reconstructed Z' mass using all the dark-matter particles in the Monte Carlo. The $\eta-\phi$ lego plots show the corresponding energy deposition in the detector. Red circles indicate visible SM hadrons, while the grey circles indicate undetected stable mesons. The crosses indicate the position of anti-k_T $R = 0.5$ jets. The relative size of each circle and cross is set by the $\sqrt{p_T}$ of the object.

The value of $r_{\rm inv}$ depends on the details of the dark-sector model. For the model described above with $M_1^2 = M_2^2$, the average proportion of the stable and unstable hadrons is equal, implying $r_{\rm inv} \simeq 0.5$. This assumes that the hadronization process is flavor-blind and that the dark quark masses are degenerate, and ignores baryon production, which is suppressed by a factor of $1/N_c^2$, where N_c is the number of dark colors.

A mass splitting between the flavors can lead to variations in $r_{\rm inv}$. Assuming $M_2 \geq M_1$, in the Lund string model [153], fragmentation into heavier dark quark pairs is suppressed by the factor

$$T = \exp\left(-\frac{4\pi|M_2^2 - M_1^2|}{\Lambda_d^2}\right). \tag{5.3}$$

Because of the exponential dependence of the fragmentation process, $r_{\rm inv}$ is very sensitive to small splittings of the mass parameters. As a result, fewer stable mesons are produced when $M_2^2 - M_1^2 > \Lambda_d^2$. This decreases the value of $r_{\rm inv}$ below 0.5. To increase $r_{\rm inv}$ above 0.5, one can increase the number of flavors N_f, thereby enlarging the number of stable mesons

	DESCRIPTION	BENCHMARK
$\sigma \times \mathrm{Br}$	cross section $\times$ branching ratio	80 fb
$M_{Z'}$	Z' pole mass	3 TeV
M_d	dark hadron mass scale	20 GeV
$\alpha_d(1\,\mathrm{TeV})$	running dark coupling	0.2
r_{inv}	ratio of stable to unstable	0.3

Table 5.1: Parametrization for semi-visible jet search.

by $N_f(N_f - 1)$, while only increasing the number of unstable mesons by N_f. Clearly, r_{inv} can take on any value between $(0, 1)$.

Table 5.1 summarizes the five parameters that are most relevant for semi-visible jet observables. Three are sensitive to the details of the dark sector: the running dark-sector gauge coupling $\alpha_d(1\,\mathrm{TeV})$, r_{inv}, and the mass scale for the dark mesons M_d. Note that by only including one value of M_d, we are assuming that the LHC will be insensitive to the dark spectrum mass splittings, *i.e.*, $M_{Z'} \gg \Lambda_d$. Additionally, there are two portal parameters: the production cross section times branching ratio into the dark sector $\sigma \times \mathrm{Br}$, and the mass of the Z'.

5.3 Search Strategy

To perform a detailed collider study, $u\bar{u}, d\bar{d} \to Z' \to \chi^\dagger \chi$ events were simulated for the 14 TeV LHC using `PYTHIA8` [154] using the default `CTEQ6` parton distribution functions. The dark-sector shower was simulated using the Hidden Valley `Pythia` module [144, 145], modified to include the running of α_d as was done for [149], with subsequent hadronization into mesons with mass M_d. Each meson had a probability r_{inv} to be a dark-matter particle. The non-dark-matter particles could decay to all four light quarks with equal probability. The possible decays of dark baryons/mesons into each other were neglected. The resulting

particles were processed through `DELPHES3`, with the default CMS settings [155], including particle flow.

Anti-k_T $R = 0.5$ jets [11] were constructed and then reclustered into two large jets [156] using the Cambridge/Achen (CA) algorithm [12] with $R = 1.1$. One could perform a resonance search using the invariant mass $M_{jj}^2 = (p_1 + p_2)^2$, where $p_{1,2}$ are the momenta of the two final large jets $j_{1,2}$. However, the M_{jj} variable degrades when there are a significant number of dark-matter particles. A variable that incorporates the missing momentum is the transverse mass:

$$M_T^2 = M_{jj}^2 + 2\left(\sqrt{M_{jj}^2 + p_{Tjj}^2}\,\not{E}_T - \vec{p}_{Tjj}\cdot\vec{\not{E}}_T\right). \tag{5.4}$$

In a detector with perfect resolution, $M_{jj} \leq M_T \leq M_{Z'}$. Figure 5.2 shows the distribution of M_{jj}, M_T and $M_{\rm mc}$ after event selection. $M_{\rm mc}$ is the reconstructed $M_{Z'}$ computed from all the reclustered jets and truth-level dark-matter four-vectors. M_T can yield a narrower, more prominent peak and be closer to $M_{\rm mc}$ depending on the choice of α_d and $r_{\rm inv}$. The top panels of Fig. 5.2 show sample events for the different signals. The dark-sector particle multiplicity decreases for smaller α_d. As $r_{\rm inv}$ is increased, the signal degrades because more stable mesons are produced and more information is lost. Note that when α_d is large enough, the radiation will not be fully captured unless the jet radius is made larger, perhaps at the expense of increasing the sensitivity to pile-up.

To estimate the reach at the LHC, we simulated 60×10^6 QCD events, 5×10^6 $W^\pm/Z+jj$ events, and 5×10^6 $t\bar{t}$ events. All samples were binned in H_T in order to increase statistics in the high-M_T tails [157], using `Madgraph5` [158] at parton level and `PYTHIA8` for the shower and hadronization. The dominant background after event selection is QCD and $W^\pm/Z+jj$. For the signal, 25000 events were generated for each choice of $M_{Z'}$ in increments of 500 GeV, using the benchmark parameters in Table 5.1. An 8 TeV sample was used to validate the QCD background and limit-setting procedure [159] against the CMS dijet resonance search [160]. The $\not{E}_T$ distribution was also validated [161].

Each event was required to have at least two $R = 0.5$ anti-k_T jets with $p_T > 200$ GeV and $|\eta| < 2.5$, as well as $\not{E}_T > 100$ GeV. These pre-selection cuts model the impact of the

trigger. Then, the following cut-flow was applied:

- Recluster jets into $R = 1.1$ CA jets (j_1, j_2);
- Require $|\eta_{j_1} - \eta_{j_2}| < 1.1$;
- Require $\Delta\phi < 1$, where $\Delta\phi$ is the minimum azimuthal angle between $\vec{\not{E}}_T$ and $\vec{p}_{Tj_{1,2}}$;
- Veto isolated $e^{\pm}/\mu^{\pm}$ with $p_T > 20$ GeV, $|\eta| < 2.4$;
- Require $\not{E}_T/M_T > 0.15$.

The $R = 1.1$ jets capture the wider radiation pattern expected from dark-shower dynamics. The cut on the pseudo-rapidity difference removes t-channel QCD [160, 162]. The lepton veto and $\Delta\phi$ requirements suppress electroweak backgrounds. Finally, the $\not{E}_T/M_T$ cut effectively acts as a missing energy requirement; cutting on the dimensionless ratio avoids sculpting the M_T distribution.

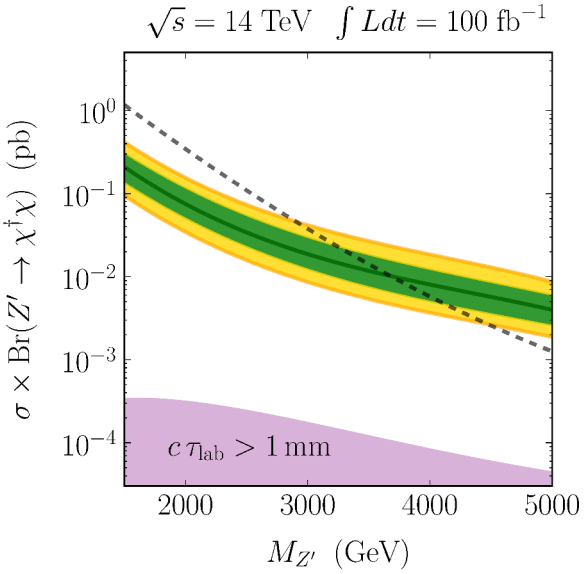

Figure 5.3: Expected $\sigma \times$Br for the signal benchmark in Table 5.1. The shaded green(yellow) band corresponds to $\pm 1(2)$ standard deviations. The dashed black line shows the $\sigma \times$ Br for a Z' with the same coupling to quarks as the SM Z^0. The shaded purple region is where the vertices are displaced, assuming $g^d_{Z'} \simeq 1$.

5.4 Results and Conclusions

After applying the selection cuts, a bump hunt was performed using M_T. At small M_T, the dominant background comes from QCD. When $M_T \gtrsim 3\,\text{TeV}$, the background is dominated by $W^{\pm}/Z + jj$, where the gauge bosons decay leptonically. Following the dijet resonance searches at CMS [160] and ATLAS [162], the resulting background distribution was parametrized using a fitting function.

Assuming the background exactly follows the fit obtained from simulation, the exclusion reach for the signal benchmark can be computed. Figure 5.3 shows the results for 100 fb^{-1} of 14 TeV LHC data as a function of $M_{Z'}$ for the benchmark parameters (Table 5.1). We assume a 10% width for the Z', as computed using the benchmark parameters. The production cross section times branching ratio for a Z' with the same coupling as the SM Z^0 is shown as a reference. A Z' with SM couplings can be probed up to masses of $\sim 3.6\,\text{TeV}$.

We estimate that the dijet limit on $\sigma \times \text{Br}(Z' \to q\bar{q})$ is comparable to the limit obtained for the dark-sector decay mode. For $g^d_{Z'} \simeq 1$, the branching ratio to the dark sector varies from 80% to 50% along the expected exclusion bound as the Z' mass increases. Thus, the model would be discovered in the semi-visible jet channel *before* it would be observed by the irreducible dijet channel; this conclusion only gets stronger for more integrated luminosity.

In the simulations, we assume prompt decays for the dark mesons. For a sufficiently heavy Z' and small couplings, the dark meson decays could yield displaced vertices. Requiring that the lab-frame decay length be $\lesssim \mathcal{O}(1\text{ mm})$ and assuming that the dark meson can decay into all four light quarks, a lower bound on the couplings can be obtained:

$$g^{\text{SM}}_{Z'} \gtrsim 10^{-2} \left(\frac{1}{g^d_{Z'}}\right) \sqrt{\frac{B}{10}} \left(\frac{M_{Z'}}{3\text{ TeV}}\right)^2 \left(\frac{\Lambda_d}{20\text{ GeV}}\right)^{-\frac{5}{2}}, \tag{5.5}$$

where $B \sim 10$ is the average boost factor computed from the benchmark simulation. (5.5) gives the lower purple region in Fig. 5.3. However, it is important to emphasize that modifications of the search strategy can still be effective in this region.

This chapter proposed a new search strategy for the discovery of hidden-sector physics in resonance searches. In particular, the focus was on dark-sector showers that result in novel

semi-visible jets—objects that are composed of SM hadrons and dark matter. We argued that this generic signature could arise from a large class of strongly coupled dark-matter models. Furthermore, we gave a simplified parameterization that allows for a systematic treatment of the signature space. Finally, we provided expected exclusion limits using a bump hunt in transverse mass. A Z' with SM-size couplings to quarks could be probed up to ~ 3.6 TeV.

There are two main extensions that can be explored that may require new strategies beyond the one discussed here. First, one can lift the restriction that the only SM states produced in the shower are quarks, and allow for leptons, photons, and/or heavy-flavor particles. Second, one can consider other production modes. In this case, the semi-visible jets may not be aligned with the $\not{E}_T$ and additional variables using jet substructure, along the lines of [163], displaced vertices, and/or the presence of low-mass resonances may be necessary.

With the LHC Run II starting, it is important to rethink the program of dark-matter searches to guarantee that a wide range of new-physics scenarios are covered. Non-trivial dynamics in the dark-matter sector is one of the many fantastic and unexpected ways that new physics can emerge. We provide a simple approach in preparation for this possibility.

Part III

Future Colliders

While it is important to maximize the physics potential in the upcoming 14 TeV LHC run, it is worthwhile to consider the next generation of colliders that way succeed the LHC physics program. Particularly, there has been strong interest in a 100 TeV proton-proton collider. We examine the physics reach for such a collider in the following chapters. In Chapter 6, we study the physics reach for stop searches at 100 TeV. In Chapter 7, we examine new physics in the Higgs Portal and the expected reach in 14 TeV and 100 TeV colliders. Chapters 6-7 are published in [164, 165] respectively.

Chapter 6

Stop Searches

6.1 Introduction

Exploring the nature of our Universe at the smallest possible scales is the primary goal of the particle physics community. This pursuit will require extending the energy frontier program beyond the 14 TeV LHC.

Recently the idea of building a 100 TeV circular proton-proton collider has gained momentum, starting with an endorsement in the Snowmass Energy Frontier report [166], and importantly followed by the creation of two parallel initiatives: one at CERN [167] and one in China [168]. For some recent studies of the capabilities of a 100 TeV collider see [169–176]. Regardless of what is discovered during the upcoming run of the LHC, data from the 100 TeV machine will still be utilized to push new particle searches to higher mass scales. The existence (or absence) of these states could have a dramatic impact on the way we think about fundamental questions. Of particular interest to this work is the question of weak scale naturalness, and specifically the possibility of TeV-scale top partners. Any discoveries of such particles at the LHC would likely require further study at a higher-energy machine. However, even in the event that the LHC does not find any top partners, this program will continue to be of central importance by pushing the fine-tuning of the Higgs mass into qualitatively new regimes.

Here we focus on the stop in supersymmetric (SUSY) extensions of the Standard Model (for a SUSY status update after Run I of the LHC, see [177]). Naturalness considerations imply that the stops should be light [178, 179] in order to regulate the Higgs mass, while the masses of first and second generation squarks are less constrained. Explicit models that realize the so-called "natural SUSY" spectrum have been constructed [180–186], and often the dominant collider signatures can be reduced to a set of now-standard Simplified Models [122] involving only the third generation squarks, a neutralino, and a gluino [187–189]. A discovery of stops, or at least an understanding of the allowed parameter space of these models, has direct implications for weak-scale naturalness.

We study the stop-neutralino Simplified Model, in which the stops are pair-produced, and each stop decays to a top and a stable neutralino[1] . This signature is well suited to compare the physics implications of different machine parameters such as $\sqrt{s}$ and total integrated luminosity.

Searches for direct stop production have been carried out at both ATLAS and CMS, providing limits on the stop mass of ≈ 800 GeV with 20 fb^{-1} at $\sqrt{s} = 8$ TeV [192–196]. The high-luminosity upgrade of the LHC (HL-LHC) is expected to deliver 3000 fb^{-1} of data at $\sqrt{s} = 14$ TeV, allowing for a discovery reach of ≈ 800 GeV stops and an exclusion reach of ≈ 1.5 TeV [197, 198].

Beyond naturalness considerations, this study is motivated by the exploration of new kinematic regimes in top physics. In 100 TeV collisions, the tops from stop decays are so highly boosted that current LHC analysis strategies, usually based on resolving the individual decay products of the top, become ineffective. This work demonstrates that an analysis that relies on a muon inside a jet can be used to discover (exclude) stop masses up to $\approx 5.5\,(8)$ TeV.

One issue in the specifications of the 100 TeV collider that has not yet been addressed is the integrated luminosity needed to fulfill its physics potential. The baseline integrated

[1] The minimal natural spectrum in the MSSM is slightly more complicated, due to the expectation that both stops, the left-handed sbottom, and the Higgsinos will all be light. The model studied here provides similar reach for the majority of the parameter space of these more complete models [190, 191].

luminosity is taken to be 3000 fb^{-1}, but we also consider scenarios yielding 300 fb^{-1} and 30000 fb^{-1}. We find that 3000 fb^{-1} may be insufficient to saturate the physics reach of a high-energy machine.

The rest of this chapter is organized as follows. Section 6.2 studies generic properties of heavy new physics decaying to boosted tops and compares the sensitivity of jet substructure techniques and muon-in-jet requirements. Section 6.3 presents a cut flow optimized for heavy stops that is based on the presence of a muon inside a jet and shows its sensitivity in the stop-neutralino mass plane; an additional analysis is presented which optimizes the reach for compressed spectra. Section 6.4 summarizes the implications of the analysis on future accelerator and detector design, and discusses the implications of the mass sensitivity for fine-tuning.

The results presented here rely on events generated at parton level with `MadGraph5` [79], showered with `Pythia6` [112], and processed using `Delphes` [155] and the Snowmass combined detector card [199]. The stop signals are normalized to the NLL + NLO cross sections computed in [200]. The Snowmass background samples [157] were used, augmented by a high statistics H_T-binned QCD sample generated for this study.

6.2 Boosted Tops at 100 TeV

Signal events in the stop-neutralino Simplified Model include pair-produced stops ($\widetilde{t}$) that decay promptly into a top quark and a stable neutralino ($\widetilde{\chi}_1^0$). Under the assumption that the stops are produced at rest, the boost of the top quark is given by

$$\gamma_t = \frac{m_{\widetilde{t}}}{2\, m_t} \left(1 - \frac{m_{\widetilde{\chi}_1^0}^2 - m_t^2}{m_{\widetilde{t}}^2} \right) \tag{6.1}$$

and the resulting top jet has a typical size of $\Delta R \sim 1/\gamma_t \sim m_t/p_T^t$.

The left panel of of Fig. 6.1 shows the p_T distribution of the leading top quark for three different stop masses (assuming a massless neutralino). For stops with a mass of a few TeV or higher, the tops from the stop decay are highly boosted with $p_T \gg m_t$. The right panel of Fig. 6.1 shows the mean distance between the W boson and the b from the decay of the

top as a function of $m_{\tilde{t}}$ and $m_{\tilde{\chi}_1^0}$.

Given that the jet radius chosen for this study is $\Delta R = 0.5$, the top will on average be contained within a single jet. Stop searches at a 100 TeV collider will therefore have to probe a kinematic regime not accessible to the 14 TeV LHC, where the top p_T relevant for most searches is less than a TeV.

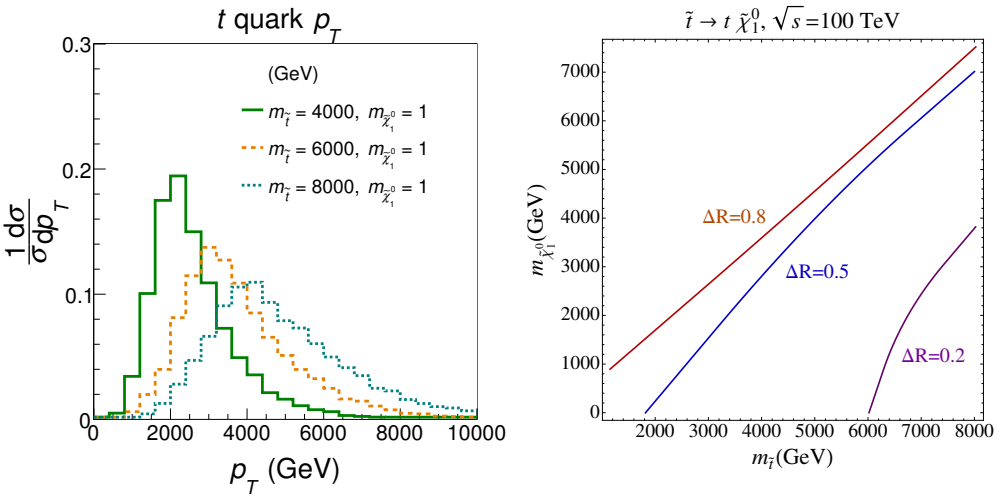

Figure 6.1: The p_T distribution of the leading top quark for $m_{\tilde{t}} = 2, 6, 10$ TeV assuming $m_{\tilde{\chi}_1^0} = 1$ GeV [left]. The average size of top jets from stop decays as a function of $m_{\tilde{t}}$ and $m_{\tilde{\chi}_1^0}$ [right].

One possible tool for separating signal from background is to tag these highly boosted tops. Note that top taggers constructed for LHC energies are optimized for large radius jets with $\Delta R \approx 1.0 - 1.5$ (for a review, see [31]). It is therefore interesting to understand if existing algorithms are suitable for events at 100 TeV. If the top tagger depends on an intrinsic angular scale, for example the Johns Hopkins top tagger [26], then the choices appropriate for tagging boosted tops at the LHC will need to be reconsidered. In contrast, the HEP top tagger [201] does not make any assumption about the angular separation of the top decay products.

Given the magnitude of the boost being considered, separating the individual constituents of the top decay requires detector granularities higher than presently available in hadronic calorimeters. For example, a 5 TeV top jet falls within a cone size of roughly $\Delta R \approx$

0.07, while the typical size of a calorimeter cell at ATLAS is $\Delta\eta \times \Delta\phi \sim \mathcal{O}\big(0.1 \times 0.1\big)$ [202]. In order to understand this effect quantitatively, we generated a sample of $t\,\bar{t}$ and QCD events at $\sqrt{s} = 100$ TeV, with a minimum generator-level p_T cut on the leading top at 500 GeV or 5000 GeV. The hadron-level events were passed through a `FASTJET` [84, 85] based code. This framework was validated against the results in [201] using a sample of 14 TeV events. In order to investigate the impact of finite calorimeter resolution, a simple pixelation was applied by summing particle energies within square cells whose widths were allowed to vary from 0 to 0.1. The events were then clustered using the Cambridge/Aachen algorithm [203, 204], where $\Delta R = 1.5\,(0.5)$ was taken for $p_T > 500\,(5000)$ GeV. The HEP top tagger was applied to the leading two jets in order to determine the efficiency for tagging a top jet and the probability of mis-tagging a QCD jet. The results are shown in Fig. 6.2, where top-tagging is found to be insensitive to the detector granularity for 500 GeV top jets, but with a cell width $\gtrsim 0.02$ is significantly degraded for 5 TeV top jets.

The jet radius changes approximately as the inverse of the top p_T, $\Delta R \sim m_t/p_T^t$, so in most of the parameter space of interest for this simplified model, this toy study demonstrates that a much finer calorimeter segmentation than that used for LHC detectors will be needed to exploit substructure techniques at higher-energy colliders. On the other hand, tracking systems have much finer granularity than is needed by the HEP top tagger, so it would be interesting to explore a Particle Flow or a purely track-based approach. We leave this for future studies.

Instead, we consider an alternative strategy with less sensitivity to the detector response. When a highly-boosted top decays leptonically, or when the resulting b (or even c) quark decay yields a lepton, it is very likely that the lepton(s) will be collinear with the top jet. Requiring a hard lepton inside a jet can therefore be used to tag boosted tops [24]. Tagging a top jet by a muon is similar to leptonic b-tagging techniques implemented at the Tevatron [205–210] and at the LHC [119, 211–213]. By definition these leptons will not be isolated from nearby tracks or calorimeter activity, removing a common handle for rejecting fake leptons. For simplicity we therefore only consider the case where a muon is

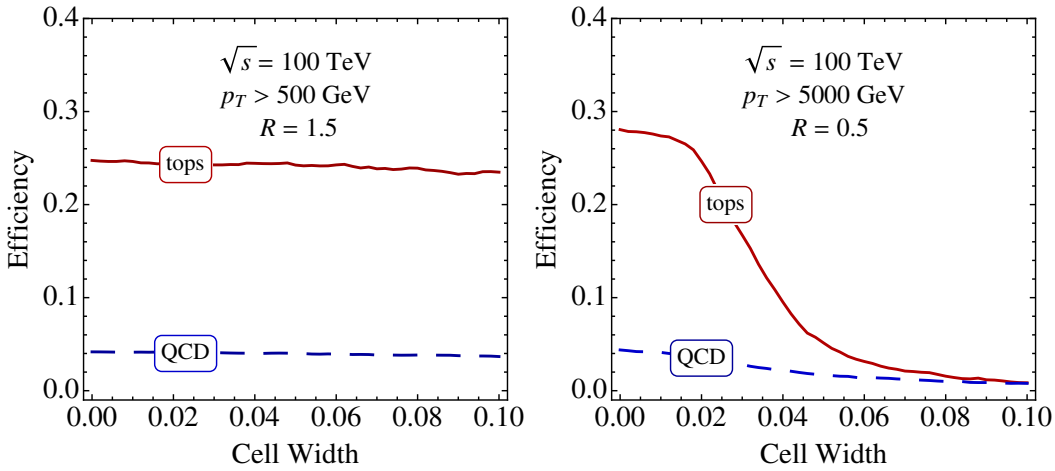

Figure 6.2: HEP top tagger performance for jets with $p_T > 500$ GeV [left] and > 5 TeV [right]. The red solid curve shows the tagging efficiency for top quarks, and the blue dashed curve shows the mis-tag rate for light-flavor QCD jets.

collinear with a jet, and assume that a layered detector design similar to that employed by LHC experiments will provide adequate rejection of fake muons. Rejection of fake electrons without the use of an isolation requirement is more detector-dependent, and is not considered here.

Figure 6.3 shows the probability of finding a 200 GeV muon within a $\Delta R < 0.5$ cone of the leading jet as a function of the leading jet p_T for several signal and background samples.[2] The signal efficiency for this requirement is roughly 15%, compared to $t\bar{t}+W/Z$ efficiencies of 3%, $t\bar{t}$ efficiencies of about 2% and QCD efficiencies around 0.4%.

For the $t\bar{t}$ background, the top quarks constitute only $\sim 60\%$ to the total jet p_T in the highly boosted regime, indicating a significant contribution from additional QCD radiation. This leads to a lower efficiency for $t\bar{t}$ than in signal events, where more of the total p_T is carried by top jets.

Our results in this section ignore the impact of any additional pp interactions (pile-up) in the event. However, we expect pile-up would only degrade the performances of hadronic taggers compared to the muon-in-jet requirement. Furthermore, it has been shown [214,215]

[2]Due to the structure of the Snowmass detector card, we are using generator level muons when computing the muon-in-jet requirement. This procedure was validated against a dedicated sample that was produced with no lepton isolation requirements imposed, thereby giving detector level muons inside jets.

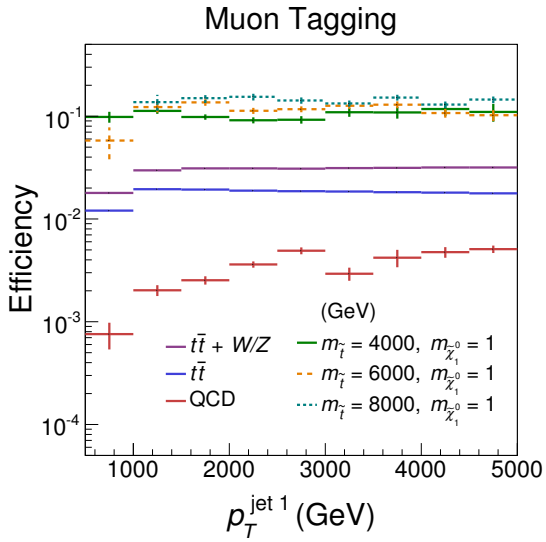

Figure 6.3: Efficiency for finding a $\mu^{\pm}$ with $p_T > 200$ GeV within $\Delta R < 0.5$ of the leading jet for three choices of stop mass, along with the $t\,\bar{t} + W/Z$, $t\,\bar{t}$ and QCD backgrounds.

that minimum bias events do not change dramatically going from ~ 10 TeV to ~ 100 TeV. A larger difference between the LHC and this machine will arise from changes in instantaneous luminosity and/or bunch spacing. If they are within a factor of a few of those at the LHC, it is not inconceivable that a Particle Flow based subtraction scheme could make the performances of substructure techniques (almost) pile-up independent at a 100 TeV collider.

6.3 Search Strategy and Results

In the previous section we discussed some general aspects of searches with boosted tops at 100 TeV. Here we propose a detailed analysis strategy that utilizes the muon-in-jet requirement, and we show the expected discovery reach and 95% C.L. exclusion sensitivity. In addition, we provide an alternative cut-flow that relies on isolated leptons in order to increase sensitivity in the compressed region where $m_{\tilde{t}} - m_{\tilde{\chi}_1^0} \approx m_t$.

6.3.1 Heavy Stops and Light Neutralinos

We make the following requirements:

1. At least two anti-k_T jets [11] with cone parameter $\Delta R = 0.5$ and kinematic cuts: $|\eta| < 2.5$ and $p_T > 1000$ GeV.
2. At least one muon with $p_{T\mu} > 200$ GeV contained within a $\Delta R = 0.5$ cone centered around one of the leading two jets.
3. Events with at least one isolated lepton with $p_T > 35$ GeV and $|\eta| < 2.5$ are rejected. The isolation criterion demands the total p_T of all particles within a $\Delta R < 0.5$ cone around the lepton to be less than 10% of its p_T.
4. $\Delta\phi_{\not{E}_T J} > 1.0$, where $\Delta\phi_{\not{E}_T J}$ is the smallest $|\Delta\phi|$ between $\not{E}_T$ and any jet with $p_T >$ 200 GeV and $|\eta| < 2.5$.
5. $\not{E}_T > 3$, 3.5 or 4 TeV. Out of the three choices, the cut is chosen for each mass point by optimizing the expected exclusion.

After imposing a muon-in-jet requirement on the background, the selected sample is composed mainly of boosted heavy quarks. The neutrinos and muons resulting from their decays will be highly collimated and the total $\not{E}_T$ will tend to be aligned with the jet momenta. Therefore it is useful to impose an angular $\Delta\phi$ cut between the $\not{E}_T$ and all the jets. For $q\,\overline{q}$, the maximum angle between each neutrino and the final q jet will be of order m_q/p_T. After a stringent $\Delta\phi$ cut, the remaining background is then boosted $t\,\bar{t} + X$ events. In particular, $t\,\bar{t} + W/Z$ is the dominant background in the signal region.

The $\not{E}_T$ and $\Delta\phi_{\not{E}_T J}$ distributions after all other cuts are applied are shown in Fig. 6.4. The low $\not{E}_T$ region is mostly dominated by QCD, whereas the high $\not{E}_T$ tail is dominated by $t\,\bar{t} + Z$ ($Z \to \nu\,\overline{\nu}$).

The results of the cut-flow with $\not{E}_T > 4$ TeV for the background and three signal mass points are shown in Table 6.1 without uncertainties. We note that corrections for electroweak radiation of W or Z bosons within high-p_T jets (e.g. in QCD dijets) could lead to muon-in-jet signatures, and at a high-energy machine these corrections can be large [216]. We expect that the $\Delta\phi$ requirement will highly suppress such contributions as it already does in events where the W or Z is produced in the matrix element, but this should be verified in future studies.

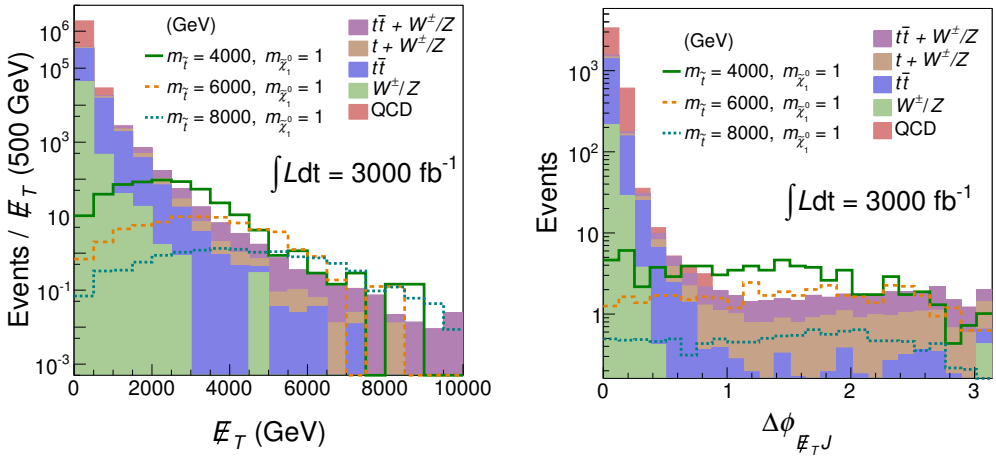

Figure 6.4: The $\not{E}_T$ [left] and $\Delta\phi_{\not{E}_T J}$ [right] distributions after all other cuts described in Section 6.3.1 have been applied, for 3000 fb^{-1} of integrated luminosity.

As a baseline, we choose the relative background and signal uncertainty to be 20%, and an integrated luminosity of 3000 fb^{-1}. However, it is useful to explore the reach of this future collider for different choices of systematics and integrated luminosities, especially to study the impact of potential accelerator and detector designs. In Sec. 6.3.4 we therefore show results for a range of integrated luminosities (with appropriate adjustments to the final $\not{E}_T$ cut for optimization). In Sec. 6.3.5, we present discovery and exclusion reaches for different choices of systematic uncertainties.

Cuts	Signal $(m_{\tilde{t}}, m_{\tilde{\chi}_1^0})$ (GeV)			$t\bar{t} + W/Z$	$t\bar{t} + j$	single t	$W/Z + j$	QCD
	(4000, 1)	(6000, 1)	(8000, 1)					
$N_{\text{jet}} \geq 2$	4.8×10^3	5.3×10^2	8.0×10^1	1.6×10^6	5.1×10^7	5.4×10^6	6.3×10^7	2.8×10^9
$N_\mu \geq 1$	9.1×10^2	1.2×10^2	2.1×10^1	1.6×10^5	4.3×10^6	3.4×10^5	5.3×10^5	2.3×10^7
isolated $l^{\pm}$ veto	9.1×10^2	1.2×10^2	2.1×10^1	1.5×10^5	4.1×10^6	3.2×10^5	5.3×10^5	2.3×10^7
$\Delta\phi_{\not{E}_T J} > 1.0$	5.0×10^2	6.5×10^1	1.2×10^1	7.6×10^3	1.6×10^5	1.4×10^4	3.3×10^4	1.1×10^6
$\not{E}_T > 4.0$ TeV	1.5×10^1	1.7×10^1	7.2	2.9	5.0×10^{-1}	6.1×10^{-1}	1.5×10^{-1}	1.2×10^{-3}

Table 6.1: Background and signal yields for the heavy stops cut-flow in Section 6.3.1, assuming 3000 fb^{-1} of integrated luminosity. Single t includes events with an extra W/Z.

6.3.2 Compressed Spectra

As the neutralino mass approaches the stop mass, both the $\not{E}_T$ and the top p_T are reduced. By relaxing some of the cuts in the previous section and trading the muon-in-jet requirement for an isolated lepton requirement, sensitivity to this region of parameter space can be improved. Our cut-flow targeting the compressed region is:

1. At least two anti-k_T jets with cone parameter $\Delta R = 0.5$. The kinematic requirements $|\eta| < 2.5$ and $p_T > 500$ GeV are imposed.
2. Two isolated leptons (either electrons or muons) with $p_{Tl} > 35$ GeV. A lepton satisfies the isolation cut when the total p_T of all particles in a cone of $\Delta R = 0.5$ around the lepton is less than 10% of its p_T.
3. $\not{E}_T > 2$ TeV.
4. $\Delta\phi_{\not{E}_T J,l} > 1.0$, where $\Delta\phi_{\not{E}_T J,l}$ is the smallest $|\Delta\phi|$ between $\not{E}_T$ and any jet with $p_T > 200$ GeV and $|\eta| < 2.5$, and any isolated lepton with $p_{Tl} > 35$ GeV and $|\eta| < 2.5$

These requirements yield increased sensitivity for $m_{\tilde{t}} \lesssim 3$ TeV close to the diagonal of the $(m_{\tilde{t}},\ m_{\tilde{\chi}_1^0})$ plane. Table 6.2 gives the results of this cut flow for the background and three signal mass points. Note that the $\not{E}_T > 2$ TeV requirement implicitly relies on the presence of extra QCD radiation in association with the signal. This implies some uncertainty on initial-state radiation that we assume is covered by the systematic uncertainties applied on the signal samples. Note that this cut-flow is much more sensitive to detector and machine details than the previous one. We therefore present it only as a a proof of principle that going to higher energies does not necessarily imply sacrificing sensitivity to compressed, i.e. soft, physics.

Including pile-up could have an important effect on the results for the compressed region. An estimate for the energy deposited in a cone of radius 0.5 at $\sqrt{s} = 100$ TeV is ≈ 200 GeV $\left(\frac{L}{10^{34}\ \mathrm{cm}^{-2}\ \mathrm{s}^{-1}}\right)$ [214, 215]. Most of this energy can be subtracted using common pile-up suppression techniques, so it is reasonable to expect small modifications to jet physics given the p_T thresholds relevant for the models considered here. The only possible

exception is the $\Delta\phi$ requirement, which would be affected by resolution effects. We verified that raising the jet p_T threshold to 500 GeV does not considerably impact our reach, giving us confidence that the impact of pile-up on the jet requirements will remain small. However, lepton isolation may suffer more significantly, which would impact the results for the compressed scenarios. Studies of such effects would require detailed assumptions of the detector performance, and thus we leave them for future work.

Cuts	Signal $(m_{\tilde{t}}, m_{\tilde{\chi}_1^0})$ (GeV)			$t\bar{t}+W/Z$	$t\bar{t}+j$	single t	$W/Z+j$	QCD
	$(2000, 1500)$	$(3000, 2500)$	$(4000, 3500)$					
$N_{\text{jet}} \geq 2$	2.0×10^5	2.6×10^4	5.0×10^3	3.9×10^7	1.8×10^9	2×10^8	1.6×10^9	9.4×10^{10}
$N_\ell \geq 2$	1.1×10^3	1.6×10^2	3.6×10^1	4.1×10^5	1.2×10^7	1.1×10^6	1.2×10^4	7.6×10^1
$\lvert\Delta\phi_{\not{E}_T J,\, l}\rvert > 1.0$	4.6×10^2	7.1×10^1	1.7×10^1	4.1×10^5	1.2×10^6	1.1×10^6	5×10^2	0
$\not{E}_T > 2$ TeV	6.8	5.3	2.9	1.2	3.6×10^{-2}	4.5×10^{-1}	0	0

Table 6.2: Background and signal yields for the compressed spectra cut-flow in Section 6.3.2, assuming 3000 fb^{-1} of integrated luminosity. Single t includes events with an extra W/Z.

6.3.3 Results

Figure 6.5 shows the exclusion and discovery potential utilizing the cut-flows discussed in the previous section. Results are presented in the stop-neutralino mass plane assuming systematic uncertainties of 20% on the background and signal yields. The discovery potential and mass reach are shown in Sec. 6.3.4-6.3.5 for different choices of integrated luminosities and systematic uncertainties.

The exclusion is obtained using CL$_s$ statistics, where the background and signal are modeled as Poisson distributions. A signal point is rejected for CL$_s < 0.05$. Alternatively, a signal is discovered when the CL$_s$ for the background only hypothesis is less than $\sim 3\times10^{-7}$, corresponding to 5σ. The expected exclusion limits and $\pm1\sigma$ contours are computed using `ROOSTATS` [217].

Stops with masses up to $\approx$ 5.5 TeV can be discovered when the neutralino is massless, assuming 3000 fb^{-1} of integrated luminosity. The exclusion reach is $\approx$ 8 TeV, which

corresponds to $\sim$ 100 signal events before cuts. Note that this agrees with the estimate obtained by extrapolating the number of excluded signal events at $\sqrt{s} = 8$ TeV [218]. Since we optimized for exclusion as opposed to discovery, there is a gap between the discovery contours of the two different search strategies.

The searches proposed here also have good discriminating power away from the massless neutralino limit. A 1.5 TeV stop could be discovered in the compressed region of parameter space. It is possible to exclude neutralino masses up to 2 TeV in most of the parameter space.

All of the results presented here have been obtained with very minimal cut-flows that do not rely on b-tagging or jet substructure techniques. Additional refinements should increase the search sensitivity, at the price of making assumptions on the future detector design.

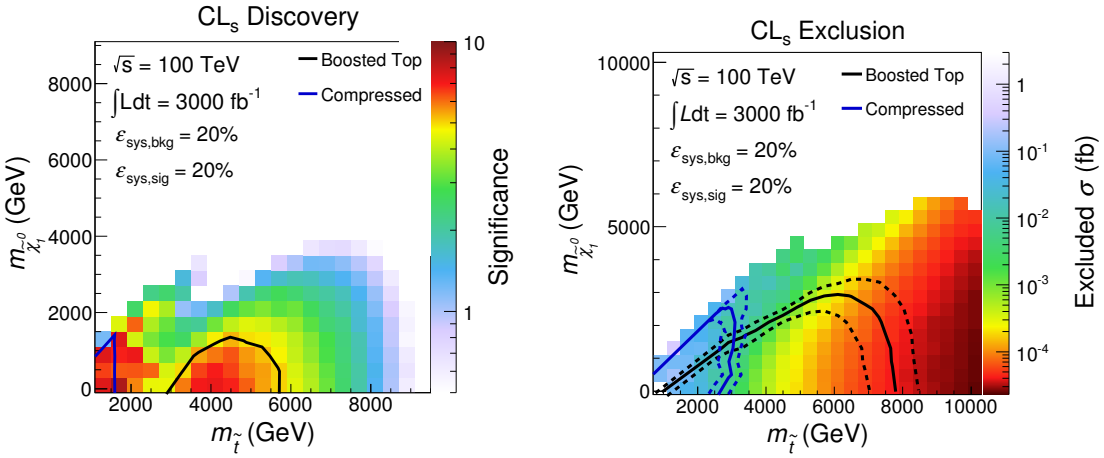

Figure 6.5: Projected discovery potential [left] and exclusion limits [right] for 3000 fb^{-1} of total integrated luminosity. At each signal point, the significance is obtained by taking the smaller CL$_s$ between the heavy stop and compressed spectra search strategies, and converting CL$_s$ to number of σ's. The blue and black contours (dotted) are the expected ($\pm 1\sigma$) exclusions/discovery contours using the heavy stop and compressed spectra searches.

6.3.4 Different Luminosities

An open question in the design for the 100 TeV proton-proton collider is the luminosity that is necessary to take full advantage of the high center of mass energy. As cross sections fall

with increased center of mass energy, one should expect that higher energy colliders require more integrated luminosity to fulfill their potential. The necessary luminosity typically scales quadratically with the center of mass energy, meaning that one should expect that the 100 TeV proton-proton collider would need roughly 50 times the luminosity of the LHC at 14 TeV.

This section shows the scaling of our search strategy as a function of the number of collected events. As the luminosity changes, we re-optimize the $\not{E}_T$ cut. For integrated luminosities of 300 fb^{-1}, a $\not{E}_T$ cut of 3 TeV is chosen. For 30000 fb^{-1}, a $\not{E}_T$ cut of 5 or 6 TeV is chosen, depending on the mass point. Table 6.3 lists the number of background events for the heavy stop search and these two choices of luminosity and $\not{E}_T$ cut. Figure 6.6 (6.7) shows the expected CL$_s$ discovery and exclusion for 300 (30000) fb^{-1} of integrated luminosity. For 300 fb^{-1}, the discovery potential is limited, but we obtain a 3σ evidence in the bulk of the parameter space. With 30000 fb^{-1}, stops of 8 (10) TeV could be discovered (excluded), a clear improvement over the 3000 fb^{-1} result.

Assuming a constant systematics of 20% for both signal and background, if we model the mass reach as a function of luminosity as

$$\frac{1}{n(\mathcal{L})} = \frac{d \log m_{\tilde{t}\ 2\sigma}(\mathcal{L})}{d \log \mathcal{L}} \tag{6.2}$$

then we find $n \simeq 7$ in the 300 fb^{-1} to 3000 fb^{-1} range of luminosities and $n \simeq 10$ in the 3000 fb^{-1} to 30000 fb^{-1} range. This indicates that the 100 TeV collider is still gaining significant reach at 3000 fb^{-1} and running out reach at 30000 fb^{-1}. Reaching a higher integrated luminosity implies running at higher instantaneous luminosity, with potential implications for detector performance that we do not consider here. However, we expect that improvements in detector design and pile-up mitigation strategies will minimize any loss of sensitivity from harsher running conditions.

6.3.5 Different Systematics

This section explores how the exclusion and discovery potential changes as a function of systematic uncertainty. For the results in Sec. 6.3.3 a systematic uncertainty of $\epsilon_{\text{sys}} =$

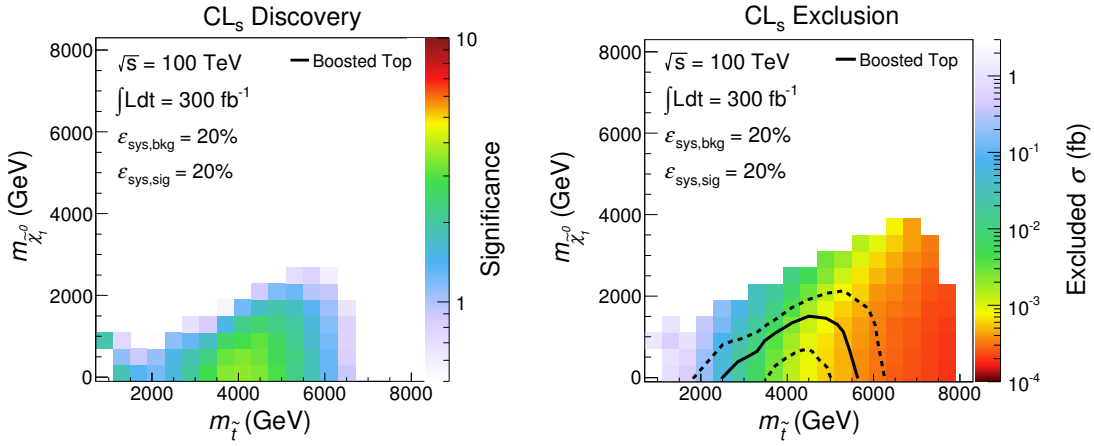

Figure 6.6: Discovery [left] and exclusion [right] limits with an integrated luminosity of 300 fb^{-1}. Only the heavy stop search is shown.

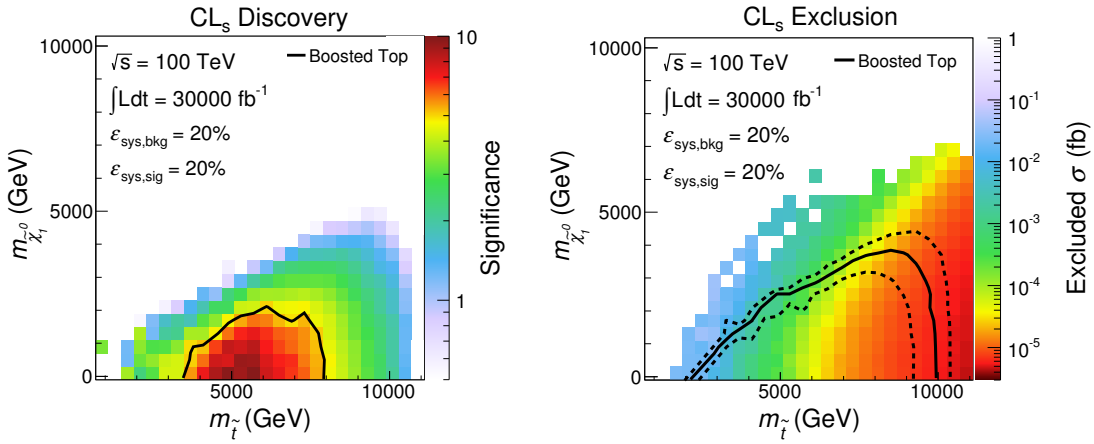

Figure 6.7: Discovery [left] and exclusion [right] limits with an integrated luminosity of 30000 fb^{-1}. Only the heavy stop search is shown.

Luminosity (fb^{-1}), $\not{E}_T$ cut (GeV)	Signal $(m_{\tilde{t}}, m_{\tilde{\chi}_1^0})$ (GeV)			$t\bar{t}+W/Z$	$t\bar{t}+j$	single t	$W/Z+j$	QCD
	(6000, 1)	(8000, 1)	(10000, 1)					
300, 3000	4.5	1.0	2.2×10^{-1}	1.3	3.1×10^{-1}	3.5×10^{-1}	1.5×10^{-2}	1.9×10^{-4}
3000, 4000	2.1×10^{1}	7.2	1.8	3.4	5×10^{-1}	6.1×10^{-1}	1.5×10^{-1}	1.2×10^{-3}
30000, 6000	1.6×10^{1}	2.3×10^{1}	9.3	4.3	1.2×10^{-1}	3.8×10^{-1}	0	6.9×10^{-3}

Table 6.3: Background and signal yields for three different choices of luminosity and three different heavy stop search signal regions. Single t includes events with an extra W/Z.

20% for both background and signal was assumed. The signal regions proposed in this chapter yield $\mathcal{O}(5)$ events for both background and signal when the masses are chosen at the edge of the exclusion reach. Figure 6.8 illustrates how the exclusion changes as the signal (background) uncertainty in the left (right) panel is increased from 20% to 50%. The exclusion is robust against changes in background systematics. A change in signal uncertainty results in a modest shift of the limits, since the signal hypothesis becomes harder to exclude when marginalized over larger systematics.

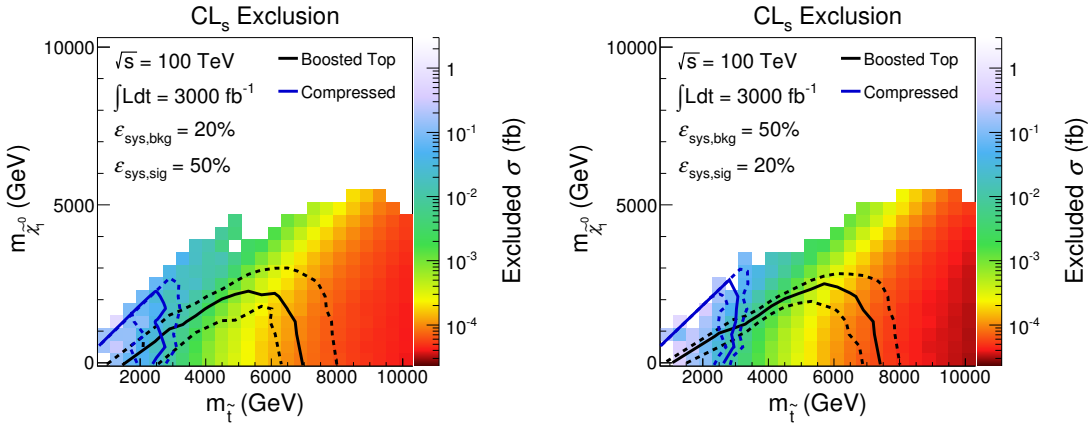

Figure 6.8: Expected exclusion limit with background and signal errors fixed to $(\varepsilon_{\text{sys,bkg}}, \varepsilon_{\text{sys,sig}}) = (20\%, 50\%)$ [left]. Expected exclusion limit with $(\varepsilon_{\text{sys,bkg}}, \varepsilon_{\text{sys,sig}}) = (50\%, 20\%)$ [right].

Figure 6.8 shows the same for the discovery potential. The expected discovery changes modestly as the systematic uncertainty on the signal is increased. However, when the background systematic uncertainty is increased to 50%, discovery becomes impossible with 3000 fb^{-1}; only 3σ evidence is possible in the bulk of the parameter space. A larger background systematic uncertainty implies that it is harder to reject the background hypothesis, so a precise understanding of the backgrounds will be crucial for discovery.

6.4 Conclusions

In this chapter we propose a robust search strategy targeting stops that decay to a top quark and a stable neutral particle at a 100 TeV proton-proton collider. A 5.5 (8) TeV stop

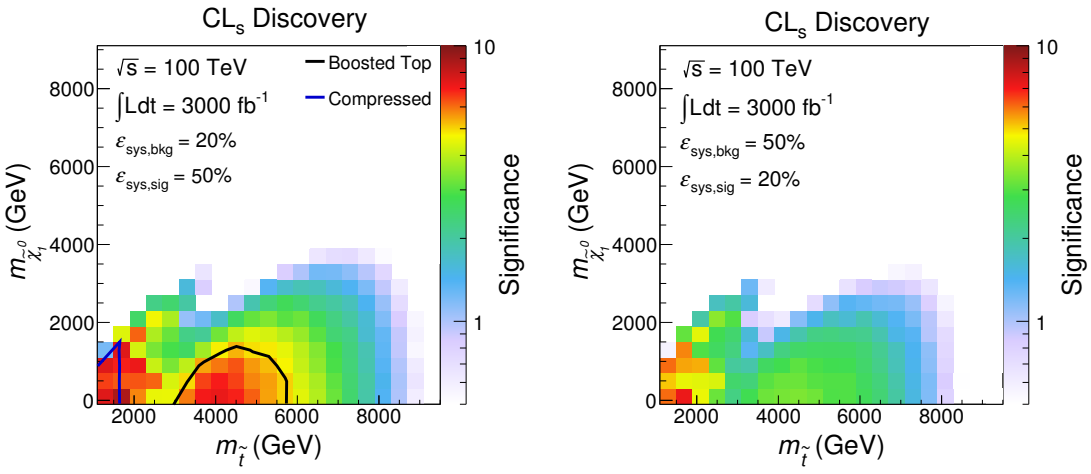

Figure 6.9: Discovery potential with background and signal errors fixed to $(\varepsilon_{\text{sys,bkg}}, \varepsilon_{\text{sys,sig}}) = (20\%, 50\%)$ [left]. Discovery potential with systematics $(\varepsilon_{\text{sys,bkg}}, \varepsilon_{\text{sys,sig}}) = (50\%, 20\%)$ [right].

could be discovered (excluded) at such a machine with 3000 fb^{-1} of integrated luminosity.

Such an exclusion would have a deep impact on our understanding of electroweak fine-tuning. In the Minimal SUSY SM (MSSM), the tuning of the electroweak scale, Δ^{-1}, receives a large contribution from the SUSY breaking parameters in the stop sector. A rough estimate of the minimum contribution to the Higgs mass parameter yields [188]:

$$\left(\frac{\Delta^{-1}}{2\times 10^{-4}}\right) \approx \left(\frac{10\ \text{TeV}}{m_{\tilde{t}}}\right)^2 \sin^2\beta \left(\frac{\log(\Lambda/\ \text{TeV})}{5}\right)^{-1}, \tag{6.3}$$

where Λ is the SUSY breaking scale and $\tan\beta = v_u/v_d$ the ratio of the two Higgs doublets vacuum expectation values. A 100 TeV proton collider clearly has the potential to impact our understanding of electroweak naturalness to an unprecedented degree.

However stop masses approaching 10 TeV are above the typical range motivated by fine-tuning considerations. Nonetheless, this range of masses could be the consequence of the Higgs mass being so far above m_Z. In the MSSM, the Higgs quartic coupling must receive sizable radiative corrections to raise the Higgs boson mass from m_Z to the observed value. The largest of these contributions arise from the top sector and comes in two forms. In the effective theory below the stop mass, the first is the contribution from the top quark and is logarithmically enhanced by the running from the mass of the top squark down to

the top quark. The second contribution is given by the A-terms which at low energies can be viewed as finite threshold corrections. In order to have top squarks with masses in the range accessible by the LHC14, there need to be sizable A-terms. However, many calculable frameworks for coupling a SUSY breaking sector to the visible sector result in suppressed A-terms, *e.g.* gauge mediation [219], anomaly mediation [220, 221], and gaugino mediation [222]. These classes of theories are the ones that have the best solutions for the SUSY flavor problem and hence are amongst the most favored. In the absence of sizable A-terms, only the logarithmically enhanced top quark contributions are left to raise the Higgs mass which results in top squarks with masses in the range 6 TeV $\lesssim m_{\tilde{t}} \lesssim$ 10 TeV at the 2σ level (for large $\tan\beta$ and small values of μ) [223]. These masses are outside the reach of the LHC14, but discoverable at a 100 TeV collider. Frequently the top squarks are amongst the lighter colored superpartners, meaning that it is possible that supersymmetry will be above the reach of the LHC14. This observation provides motivation for building another energy frontier machine, even in the case where no new physics is found at the LHC14.

Beyond the theory motivation, the lessons of this study can be generalized to a wide class of searches for boosted top quarks signatures. In particular, there are important implications for future detector design. For example, a granularity of $\Delta\phi \times \Delta\eta \approx 0.02 \times 0.02$ is needed if hadronic substructure techniques are going to be effective. This requirement might be relaxed by relying on tracking information incorporated into a more complicated reconstruction algorithm such as Particle Flow. On the other hand, requiring a muon within a jet is a simple and robust way to exploit the qualitative differences between new physics and SM backgrounds that does not require detector improvements beyond what the LHC can do today.

Furthermore we have shown that it would be desirable to achieve higher integrated luminosity than presently used in 100 TeV studies. The current benchmark of 3000 fb^{-1} [169–176] does not saturate the physics reach of this machine. The ideal integrated luminosity would be $10000 - 30000$ fb^{-1}.

Designing searches for heavy stops yields a concrete example of how a 100 TeV collider is qualitatively different from the LHC. The new energy regime that this machine will explore is so far above the electroweak scale as to render traditional search strategies ineffective. On the other hand, this makes the analyst's job easier since signals and backgrounds become more qualitatively different. This is exemplified by the sensitivity that can be derived using the simple cut-flows presented in this work.

Chapter 7

Higgs Portal Above Threshold

7.1 Introduction

The discovery of the Higgs boson [3,93] provides unprecedented opportunities in the search for physics beyond the Standard Model (SM). More than any other state in the Standard Model, the Higgs is a sensitive barometer of new physics. Perhaps the most familiar opportunity involves Higgs couplings; the rigidity of electroweak symmetry breaking in the Standard Model uniquely determines the interactions of the SM Higgs, such that any deviations in couplings would be an unambiguous indication of new physics. But the Higgs also provides an entirely new gateway to physics beyond the Standard Model thanks to the low dimension of the operator $|H|^2$: it admits new marginal or relevant operators of the form $|H|^2\mathcal{O}$, where $\mathcal{O}$ is a gauge-invariant operator with $\Delta_{\mathcal{O}} \lesssim 2$. The classic example is $\mathcal{O} = \phi^2$ were ϕ is neutral under the SM but enjoys a Z_2 symmetry [133,224–227]. This *Higgs Portal* provides an entirely new avenue to access physics beyond the Standard Model. Such portals are motivated not only on purely pragmatic grounds as one of only two possible marginal couplings between the SM and SM-singlet states, but also on theoretical grounds in diverse scenarios relating to dark matter, electroweak baryogenesis, and solutions to the gauge hierarchy problem. Now that the Higgs boson has been discovered, the exploration of possible Higgs Portals and their signatures has become a high priority at the LHC and

future colliders.

In this chapter we consider the scalar Higgs Portal consisting of

$$\mathcal{L} = \mathcal{L}_{SM} - \frac{1}{2}\partial_\mu\phi\partial^\mu\phi - \frac{1}{2}M^2\phi^2 - c_\phi|H|^2\phi^2 \tag{7.1}$$

where H is the SM-like Higgs doublet and ϕ is a scalar neutral under the Standard Model.[1] We have taken ϕ to be a real scalar, but it could equally well be a complex scalar and carry charges under additional gauge sectors. The coupling c_ϕ can take arbitrary values, but in Higgs Portals motivated by baryogenesis or naturalness, c_ϕ is often $\mathcal{O}(1)$. The ϕ field may also possess self-couplings relevant for baryogenesis or couplings to additional states in the hidden sector, but these are in general irrelevant to determining how well the portal coupling of (7.1) can be probed directly to discover or exclude the scalar ϕ.

There are many cases in which ϕ is relatively easy to detect. If ϕ acquires a vacuum expectation value then Higgs-singlet mixing can leave direct signals in Higgs couplings and the production and decay of a heavy Higgs state [133], both of which may be probed effectively at the LHC and future e^+e^- machines. Far more challenging is the scenario where the ϕ respects an unbroken Z_2 symmetry, $\phi \to -\phi$, in which case there is no Higgs-singlet mixing and the couplings of the Higgs are unaltered at tree level. After electroweak symmetry breaking the theory consists of

$$\mathcal{L} = \mathcal{L}_{SM} - \frac{1}{2}\partial_\mu\phi\partial^\mu\phi - \frac{1}{2}m_\phi^2\phi^2 - c_\phi v h\phi^2 - \frac{1}{2}c_\phi h^2\phi^2 \tag{7.2}$$

where $m_\phi^2 = M^2 + c_\phi v^2$ in units where $v = 246$ GeV. The Higgs Portal coupling is the only connection between ϕ and the Standard Model, and so the only available production mode at colliders is $\phi\phi$ production via the Higgs boson. By assumption ϕ has no SM decay modes and appears as missing energy in collider detectors. Discovering or excluding such a Higgs Portal at pp machines requires focusing on Higgs associated production modes in order to identify the missing energy signal.[2]

[1] In this work we will neglect other "portal" couplings to fermions or vector bosons neutral under the Standard Model. Such interactions are irrelevant (and in the case of vector bosons, not even gauge invariant) and should often be properly treated by integrating in additional states.

[2] Throughout we will take c_ϕ as a free parameter with values up to rough perturbative bounds at the

When $m_\phi < m_h/2$ this scenario may be very efficiently probed via the Higgs invisible width [108,228–232], since the Higgs can decay on-shell into ϕ pairs and the smallness of the SM Higgs width ensures the rate for $pp \to h + X \to \phi\phi + X$ is large for a wide range of c_ϕ. When $m_\phi > m_h/2$, however, the Higgs cannot decay on-shell to $\phi\phi$, and ϕ pair production instead proceeds through an off-shell Higgs, $pp \to h^* + X \to \phi\phi + X$. The cross section for this process is then suppressed by an additional factor of $|c_\phi|^2$ as well as two-body phase space, leading to a rapidly diminishing rate and extremely challenging prospects at the LHC. Nonetheless, this may be the only avenue for discovering or excluding Higgs Portals above the kinematic threshold for production via an on-shell Higgs boson.

In this chapter we seek to determine the prospects for exclusion or discovery of ϕ at the LHC and future colliders when $m_\phi > m_h/2$. For simplicity we focus on $\sqrt{s} = 14$ TeV at the LHC and $\sqrt{s} = 100$ TeV at a future pp collider; the sensitivity at lepton colliders was studied extensively in [233]. Although the possibility of probing Higgs Portal states via an off-shell Higgs was identified even before Higgs discovery [228, 229], collider studies to date have been somewhat limited. In [234] the state of existing limits was established by reinterpretation of LHC searches for invisible Higgs decays at $\sqrt{s} = 8$ TeV in terms of vector boson fusion, gluon associated production, and Z associated production via an off-shell Higgs, along with limited projections for $\sqrt{s} = 14$ TeV. Sensitivity to the novel H-Higgsstrahlung mode has been studied at $\sqrt{s} = 8$ & 14 TeV [235], while sensitivity at $\sqrt{s} = 100$ TeV has been broached in a limited study of vector boson fusion production [236]. Further study at $\sqrt{s} = 14$ & 100 TeV is strongly motivated, both to help optimize future searches at the LHC and to establish the physics case for a future hadron collider.

The most promising channel at pp colliders is vector boson fusion (VBF) production of ϕ pairs via an off-shell Higgs boson, leading to a signal with two forward jets and missing energy. Ancillary channels sensitive to the missing energy signal include gluon fusion production (ggH) with an associated jet, $t\bar{t}$ associated production (ttH), Z-Higgsstrahlung

relevant scale. However we do not consider RG effects which may also be interesting for constraining large couplings by requiring the absence of Landau poles, as these depend sensitively on additional dynamics in the hidden sector.

(ZH), and the novel H-Higgsstrahlung (HH) channel giving rise to mono-Higgs plus missing energy [235]. Each has relative virtues. The cross section for ggH production is largest at $\sqrt{s} = 14, 100$ TeV but the additional jet requirement and kinematic separation of signal from background reduces signal significance. The ttH cross section is significantly smaller but grows substantially at 100 TeV, and the $t\bar{t} + \not{E}_T$ final state has already proven sensitive to invisible decays of the Higgs boson at 8 TeV [237]. The cross section for ZH production is among the smallest of the modes and not well separated from the $Z + \nu\nu$ backgrounds, rendering it less promising. The $h + \not{E}_T$ signature of HH production is particularly interesting, as it directly probes the Higgs Portal interaction, but preliminary study at $\sqrt{s} = 8, 14$ TeV [235] suggests far less sensitivity than the VBF mode [234].[3] Consequently, the balance of production cross section and background separation provided by VBF render it the most promising of the channels, but for completeness in this work we will consider the prospects of VBF, ggH, and ttH searches at $\sqrt{s} = 14$ and 100 TeV.

Note there is also a complementary, indirect means of probing this scenario through its impact on precision Higgs coupling measurements. The interaction (7.1) leads to shifts in the Higgs-Z coupling relative to the Standard Model that may be probed through measurements of the Zh production cross section at future e^+e^- colliders [238, 239]. Precision on $\delta\sigma_{Zh}$ is expected to approach the level of $\sim 0.32\%$ at 1σ at circular e^+e^- colliders such as CEPC/TLEP [240]. A particularly interesting question is whether significant deviations in σ_{Zh} at an e^+e^- collider may be followed by conclusive evidence for (7.1) at a future pp collider.

This chapter is organized as follows: We begin in Section 7.2 by reviewing three motivated scenarios for physics beyond the Standard Model giving rise to Higgs Portal interactions. This helps to motivate regions of the Higgs Portal parameter space that might be probed by direct searches. In Section 7.3 we outline our procedure for simulating Higgs Portal searches at the LHC and future colliders in vector boson fusion, gluon associated production, and $t\bar{t}$ associated production. In Section 7.4 we present the exclusion and dis-

[3] The interpretation of [235] for $c_\phi > 1, m_\phi \lesssim v$ is also unclear, as in this regime the mono-Higgs final state accumulates comparable contributions from both single and double insertions of the Higgs Portal interaction.

covery reach for searches at $\sqrt{s} = 14$ TeV and 100 TeV and discuss the implications for motivated new physics scenarios. We conclude in Section 7.5 and reserve some of the details of our electroweak baryogenesis parameterization for Section 7.6.

7.2 New physics through the Higgs Portal

Although the Higgs Portal is motivated purely as a leading operator through which generic new physics might couple to the Standard Model, there are a variety of specific scenarios for physics beyond the Standard Model (BSM) in which Higgs Portal couplings feature prominently. These scenarios provide a motivated range of masses and couplings against which we can benchmark the reach of Higgs Portal searches at the LHC and future colliders.

7.2.1 Electroweak baryogenesis

A particularly motivated scenario for Higgs Portal interactions arises in models of baryogenesis aimed at generating the observed asymmetry between baryons and anti-baryons. The Standard Model famously contains the ingredients necessary for baryogenesis to occur *in principle* during the electroweak phase transition, realizing the scenario of electroweak baryogenesis (EWBG). However, while the ingredients are present for electroweak baryogenesis to occur in principle, in practice the parameters of the Standard Model are such that the electroweak phase transition is too weak to realize the necessary departure from equilibrium [241]. The phase transition may be rendered sufficiently first-order if the Higgs couples strongly to additional light degrees of freedom, potentially connecting the Higgs Portal to EWBG.

The general story of electroweak baryogenesis is well known. In the early universe, one expects electroweak symmetry to be restored at high temperature [242,243]. The net baryon number is zero as any deviation will be washed out by electroweak sphalerons, which are unsuppressed in the unbroken phase. As the temperature cools to near the critical temperature T_c, the unbroken and broken phase become roughly degenerate. Bubbles of broken electroweak symmetry begin to form. With sufficient CP violation [244], interactions with

surrounding particles will produce a net baryon number [245–249]. Within the bubble, electroweak symmetry is broken and sphaleron transition rates are highly suppressed, such that the generated baryon asymmetry is maintained. This requires the Boltzmann suppression for the sphaleron to be sufficiently high [250]

$$e^{-\Delta E_{\text{sphaleron}}/T_c} \lesssim e^{-10} \tag{7.3}$$

Since it is generally difficult to compute the sphaleron energy, one typically approximates the baryon asymmetry condition by computing the thermal potential and demanding [243]

$$\frac{\phi(T_c)}{T_c} \gtrsim 1.0 \tag{7.4}$$

where $\phi(T_c) \equiv v_c$ is the vacuum expectation of the Higgs field in the broken phase at the critical temperature. Despite the fact that equation (7.4) is gauge dependent, we will use it as a leading order estimate, since even a careful result will still require two-loop calculations in order to be reliable [250].

In the Standard Model itself, the electroweak phase transition is not strong enough to satisfy the condition (7.4), requiring BSM states [251–257] or corrections to the SM EFT [258] to alter the Standard Model effective potential and render the phase transition strongly first-order. To properly influence the effective potential, the new states must be light (in order to be relevant during the electroweak phase transition) and relatively strongly coupled to the Higgs boson (in order to substantially alter the thermal potential). This raises the tantalizing prospect of discovering or falsifying electroweak baryogenesis through direct searches at colliders. If the new states possess Standard Model quantum numbers, they may be readily detected through either direct searches or indirect effects on Higgs couplings [259, 260]. But singlet scalars coupling through the Higgs portal are also a viable candidate, with correspondingly weaker prospects for direct and indirect probes. In this respect it is particularly worthwhile to study the sensitivity of the LHC and future colliders to singlet-assisted electroweak baryogenesis.

The parameter space of singlet-assisted electroweak baryogenesis was recently considered in detail in [236] (see also [133,259,261–267]), and we will largely follow their discussion here.

There are two possibilities for singlet-assisted electroweak baryogenesis, corresponding to a single-step and a double-step phase transition, respectively. The single-step phase transition proceeds purely along the Higgs direction, where the role of the singlet(s) is to correct the Higgs effective potential to render the electroweak phase transition strongly first-order. Alternately, if $M^2 < 0$, the universe can first undergo a transition to a vacuum along the singlet direction and then proceed to the EWSB vacuum. This amounts to a tree-level modification of the Higgs potential and can lead to an arbitrarily strong first-order phase transition. At the level of the Higgs Portal model in (7.1), $M^2 < 0$ corresponds to a runaway direction, but this may be stabilized by a quartic coupling of the form $\lambda\phi^4$ and the strength of the phase transition dialed by adjusting λ. A third possibility is for a one-step phase transition to proceed via thermal effects as in the MSSM, but this occurs strictly in the two-step regime.

We illustrate the viable parameter space of EWBG in the Higgs Portal model in Fig. 7.1. A two-step transition may occur in the region corresponding to $M^2 < 0$ (i.e., $c_\phi v^2 > m_\phi^2$), with the proper ordering of the singlet vacuum and EWPT vacuum achieved by dialing the quartic λ. For modest negative values of M^2 this two-step transition is under perturbative control, but far in the $M^2 < 0$ region this requires nonperturbatively large λ where we lack control but cannot definitely rule out EWBG. In the region with $M^2 > 0$ we plot contours of v_c/T_c as a function of c_ϕ and m_ϕ, allowing that EWBG may occur in regions with $v_c/T_c \gtrsim 0.6$ given unknown details of baryogenesis during the phase transition. We reserve some details of our calculation in this region for Section 7.6. Our results for this region are in good agreement with the results presented in [236]. This provides a strongly motivated target for direct searches for Higgs Portal states at the LHC and future colliders.

7.2.2 Dark matter

Throughout this work we assume that ϕ is charged under an approximate Z_2 such that it is stable on collider timescales. However if the Z_2 symmetry is exact the Higgs Portal furnishes a dark matter candidate [224–227, 268], adding further motivation to collider searches for

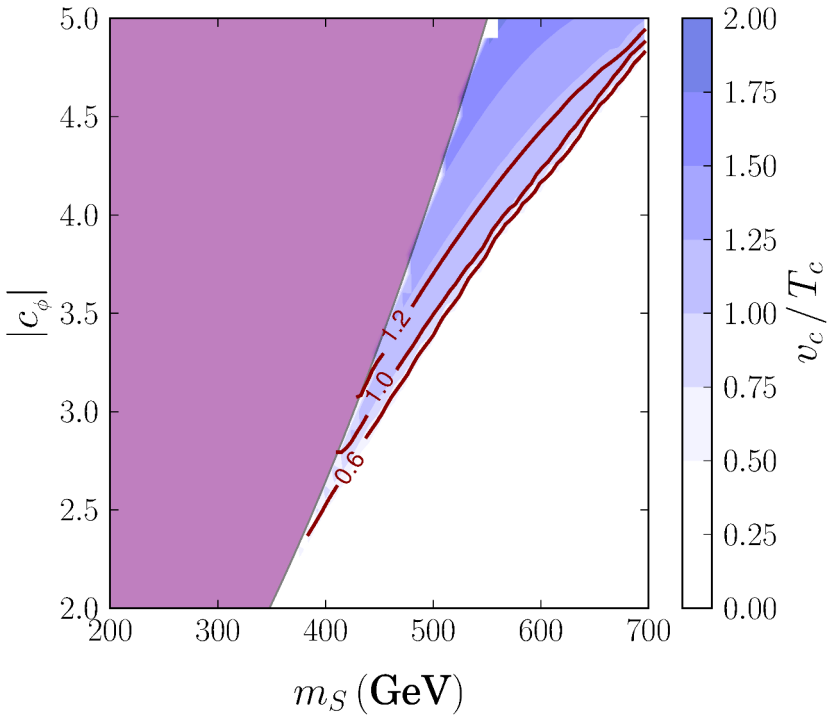

Figure 7.1: Values of v_c/T_c as a function of m_ϕ and c_ϕ for singlet-assisted electroweak baryogenesis. The shaded purple region indicates a runaway for the Higgs Portal model corresponding to $M^2 < 0$, but the runaway can be stabilized by adding a quartic coupling of the form $\lambda\phi^4$. A perturbative two-step phase transition may then proceed in a ~ 50 GeV-wide penumbra at the edge of the shaded purple region, while a two-step transition deeper in the purple region cannot be ruled out but requires nonperturbatively large values of λ to ensure the EWSB vacuum is deeper than the singlet vacuum [236].

the Higgs Portal above threshold. Higgs Portal dark matter is very predictive in the sense that if ϕ is required to provide the entirety of the observed dark matter abundance and this abundance arises thermally, then for a given m_ϕ the required coupling c_ϕ is determined. This is shown in Fig. 7.2, where it can be seen that requiring the observed DM abundance leads to relatively small couplings.[4] If ϕ only accounts for some fraction of the dark matter, or if it is produced non-thermally in the early Universe from e.g. late decays of some other field, then this requires larger couplings.

Although it only communicates with the SM via the Higgs sector, current direct detection experiments are already sensitive to Higgs Portal dark matter. In the dashed line of Fig. 7.2 the current bounds on c_ϕ from the LUX experiment [269] are shown assuming that ϕ comprises the entirety of the observed DM abundance. Such a scenario typically requires either late-time dilution of the DM abundance to ameliorate over-production due to small couplings, or alternatively late-time DM production to counteract the over-annihilation of DM due to large couplings.[5] However, if only a standard thermal history is assumed with no entropy release or DM production below temperatures $T \sim m_\phi/20$ then regions where ϕ under-annihilates and is overproduced are excluded by observations. In regions where it over-annihilates and comprises only some subcomponent of the DM the direct detection constraints must be re-weighted to account for the reduced abundance and it must be assumed that some other field makes up the total of the DM abundance. In this case, with only the assumption of a standard thermal history, the direct detection constraints become weaker, as shown in the solid line of Fig. 7.2.

The complementarity of direct detection and collider probes of Higgs Portal DM can be understood from some simple scaling arguments. For $m_\phi < m_h$ the DM annihilates through an s-channel Higgs. Thus $\langle \sigma v \rangle \propto c_\phi^2$ and $\Omega_\phi h^2 \propto c_\phi^{-2}$. The direct detection cross section scales as $\sigma_n \propto c_\phi^2$. Taking the product of this cross section with the relic density and assuming a standard thermal history in this mass range leads to overall direct detection rates ($R_{DD} = \sigma_n \times \rho_{TH}/\rho_0$) which are largely insensitive to the coupling $R_{DD} \propto c_\phi^0$.

[4] This relic abundance has been calculated using the formulae of [266].

[5] We have used the effective Higgs nucleon coupling $f_N = 0.29$ as found in [270, 271].

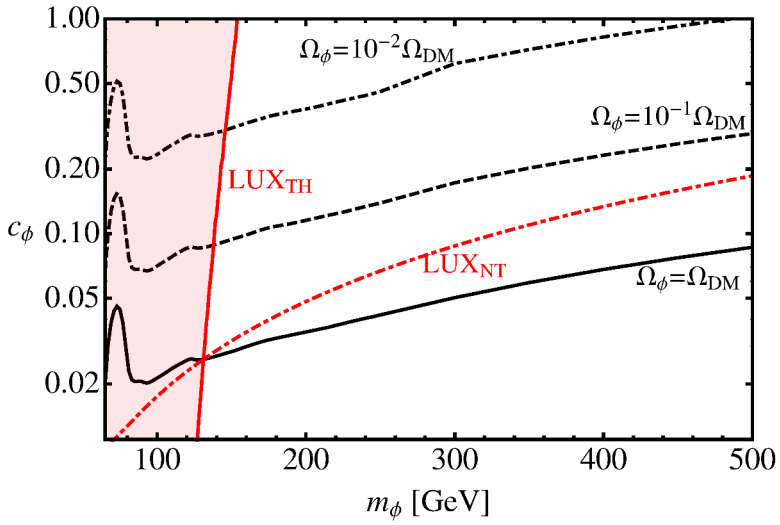

Figure 7.2: Contours of relic DM density from freeze-out through the Higgs Portal. Constraints on the parameter space from the LUX direct detection experiment [269] are shown in dotdashed red (labelled LUX_{NT}) where an additional assumption is made that in regions where thermal freeze-out over- or under-produces DM, additional fields and couplings lead to late-time DM dilution or production to realize the observed density. On the other hand, the solid red line (labelled LUX_{TH}) and shaded region show the parameter space which is excluded if one only takes the Lagrangian of Eq. (7.1) and the assumption of a standard thermal history. In this case $\Omega_\phi \propto c_\phi^{-2}$ and $\sigma_n \propto c_\phi^2$ thus the exclusion is almost independent of the coupling, and largely depends only on the mass.

Interestingly this implies that for the Higgs Portal with a thermal history, predicted direct detection rates in this mass range are almost independent of the Higgs Portal coupling, and the predicted rate essentially becomes a function of the mass only. This is demonstrated in Fig. 7.3 where the cross-section is weighted by the fractional density of Higgs Portal DM from a standard thermal history to give R_{DD} as a function of c_ϕ. The coupling c_ϕ is varied over two orders in magnitude, however the direct detection rate predicted by a standard thermal history only varies by $\mathcal{O}(10\text{'s}\%)$. This demonstrates that over the mass range 100 GeV $< m_\phi <$ 500 GeV direct detection exclusions stronger than $\mathcal{O}(1\times10^{-45}\text{cm}^2)$ actually exclude the Higgs portal with a standard thermal history independent of the Higgs portal coupling. It should be noted that non-standard thermal histories may significantly modify the constraint.

For $m_\phi > m_h$ annihilation can also proceed into two Higgs bosons, hence for large c_ϕ we

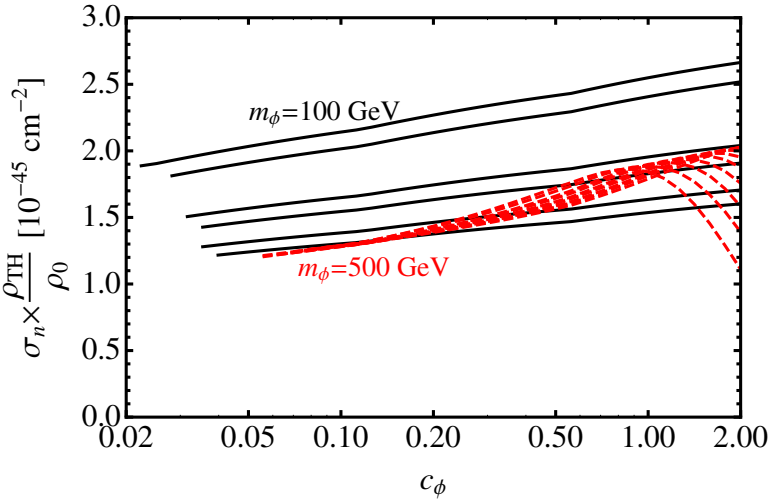

Figure 7.3: The DM-nucleon scattering cross section weighted by the fractional relic density predicted by a standard thermal history $R_{DD} = \sigma_n \times \rho_{TH}/\rho_0$ as a function of the Higgs portal coupling c_ϕ for a variety of masses from 100 GeV $< m_\phi <$ 500 GeV in steps of 25 GeV. Masses $m_\phi < 2m_h$ are shown in solid black and $m_\phi > 2m_h$ in dashed red. Regions where DM is over-produced are not shown. This demonstrates that direct detection predictions for the Higgs portal with a standard thermal history only depend very weakly on the coupling and exclusions stronger than $\sigma_n < \mathcal{O}(1\times10^{-45}\text{cm}^2)$ typically exclude the Higgs portal with a standard thermal history independent of the coupling. The suppression with large coupling is shown whenever the $\phi + \phi \to h + h$ starts to dominate when kinematically accessible.

have $\langle\sigma v\rangle \propto c_\phi^4$ in the limit of large c_ϕ. Now taking the product of thermal abundance and direct detection cross section we have $R_{DD} \propto c_\phi^{-2}$. Thus the suppression of relic density can overcome the enhancement of scattering cross section and a standard thermal history leads to smaller direct detection rates for larger couplings, as demonstrated in Fig. 7.3 . On the other hand, the collider cross sections scale as c_ϕ^2, with the exception of mono-Higgs signals which scale as a polynomial up to c_ϕ^4.

Thus we are led to a strong sense of complementarity between direct detection and collider probes of the Higgs Portal.

- If the Z_2 symmetry is exact and a saturation of the observed DM density is assumed (which may require a non-thermal history), then direct detection probes are likely to be most sensitive.

- If the Z_2 symmetry is exact and a standard thermal history is assumed then in regions

where $\Omega_\phi \leq \Omega_{DM}$ colliders and direct detection experiments are likely to be complementary probes, sensitive to different parameter regions due to a different scaling behavior with the portal coupling c_ϕ.

- If the Z_2 symmetry is approximate and only stabilizes ϕ on the timescale $\tau \gtrsim 10^{-8}$s but is allowed to decay in the early Universe, or if the Z_2 symmetry is exact but ϕ has hidden sector decays to other neutral states then colliders are the only probes of the Higgs Portal coupling, above or below threshold.

The Higgs Portal ties together aspects of cosmology and collider physics, allowing for very different probes of this coupling depending on the symmetry structure, mass, and thermal history of the Universe. This interplay strongly motivates exploring the Higgs Portal over the widest mass range achievable.

7.2.3 Neutral naturalness

Electroweak naturalness provides another motivation for the existence of neutral weak-scale scalars with large Higgs Portal couplings. Although most solutions to the hierarchy problem involve new states charged under the Standard Model, it is entirely possible that the weak scale is protected by additional degrees of freedom that are *neutral* under the Standard Model and couple exclusively through the Higgs Portal. Such states arise in the mirror twin Higgs [125] and orbifold Higgs [272] models, and more generally are consistent with a bottom-up approach to naturalness [239].

A concrete, UV-complete realization of a Higgs Portal scenario relating to electroweak naturalness arises in the supersymmetric completion of the twin Higgs [125, 273, 274]. Here the weak scale enjoys double protection from the approximate global symmetry of the twin Higgs mechanism as well as spontaneously broken supersymmetry. The role of the top partner is shared among the conventional supersymmetric partners of the top quark (the $\tilde{t}_L, \tilde{t}_R$), the SM-neutral fermionic top partners of the twin Higgs (the $t', \bar{t}'$), and the scalar superpartners of the t's (the $\tilde{t}'_L, \tilde{t}'_R$). Both the t' and the $\tilde{t}'$ are pure singlets under the Standard Model and couple uniquely through the Higgs Portal. In particular, the scalars $\tilde{t}'$

inherit a coupling to the physical SM-like Higgs h precisely of the form

$$\mathcal{L} \supset |y_t|^2 v h(|\tilde{t}'_L|^2 + |\tilde{t}'_R|^2) + \frac{1}{2}|y_t|^2 h^2(|\tilde{t}'_L|^2 + |\tilde{t}'_R|^2) + \mathcal{O}(v^2/f^2) \tag{7.5}$$

where $f \gg v$ is the order parameter of global symmetry breaking in the twin Higgs. Here the sign of the coupling corresponds to double protection; the $\tilde{t}'$ serve to compensate for radiative corrections coming from the $\tilde{t}$ and t'. The $\tilde{t}'_{L,R}$ comprise six complex scalars in total, each with $\mathcal{O}(y_t^2)$ Higgs Portal coupling. If these states are approximately degenerate, then from the perspective of collider phenomenology this is equivalent to one real scalar with $|c_\phi| = \sqrt{3}|y_t|^2 \sim 1.7$. Although the detailed naturalness of this scenario depends on the mass scales of the $\tilde{t}, t'$, and $\tilde{t}'$, in general naturalness favors the $\tilde{t}'$ as close to the weak scale as possible.

7.3 Searching for the Higgs Portal at pp colliders

Having motivated the parameter space for Higgs Portal interactions in a variety of scenarios, we now turn to pp-collider studies for the Higgs Portal model (7.1) in various channels of interest at $\sqrt{s} = 14$ & 100 TeV. In this section we describe our collider simulation for searches involving vector boson fusion, monojet, and $t\bar{t}$ associated production, reserving a discussion of the results for Section 7.4.

For the signal events, we implement the model in `FeynRules`, setting $m_h = 125$ GeV. Events are then generated at leading order using `MadGraph5 v1.5.8` [79], fixing $c_\phi = 1$ and varying values of m_ϕ. We infer results for $c_\phi \neq 1$ subsequently, by rescaling the signal cross section by $|c_\phi|^2$. We also simulate the primary backgrounds in `MadGraph5`. For both signal and backgrounds, the events are showered and hadronized using `Pythia 8.186` [154], tune 4C. Detector simulation is performed using `Delphes v3.1.2` with the default CMS detector card (for 14 TeV) and the Snowmass detector card [199] (for 100 TeV). Jets are clustered using the anti-k_T algorithm [11], as implemented in `FastJet v3.0.6` [85], with a cone size of $R = 0.5$. All jets are required to have $p_{Tj} > 30$ GeV. The lepton isolation criterion in `Delphes` is defined as `RelIso` $\equiv p_T^{\rm cone}/p_{T\ell} < 0.1$, where $p_T^{\rm cone}$ is the sum of hadronic p_T

within a cone of $R = 0.3$ of the lepton. A minimal p_T cut of 10 GeV is applied for all leptons.

7.3.1 The Higgs Portal in $\not{E}_T$ + vector boson fusion

We begin with vector boson fusion, which we expect will be the primary discovery channel for scalars coupling through the Higgs Portal. The topology for this process is identical to that of an invisibly-decaying Higgs produced via vector boson fusion, save that now the intermediate Higgs is pushed off-shell. The final state is $\phi\phi jj$ with forward jets, while the primary backgrounds to this process are Z+jets, W+jets, $t\bar{t}$ + jets, and QCD multijets. For this search we simulate Zjj and Wjj matched up to one additional jet and $t\bar{t}$ matched up to two additional jets. We do not simulate QCD multijets due to the usual challenges of reliably simulating multijet production, but we adopt a cut flow designed to minimize QCD multijet backgrounds.

After requiring at least two jets in the event, we apply the following baseline cuts

$$p_{Tj_{1(2)}} > 50\,\text{GeV} \qquad |\eta_{j_{1(2)}}| < 4.7 \tag{7.6}$$

$$\eta_{j_1}\eta_{j_2} < 0 \qquad |\eta_{j_1} - \eta_{j_2}| > 4.2 \tag{7.7}$$

In addition to these cuts, we veto events containing an isolated $e^{\pm}$ or $\mu^{\pm}$, using the isolation requirement as defined earlier. We also apply a central-jet veto by vetoing events containing a third jet with $p_{Tj} > 30$ GeV and $\min\eta_{j_{1,2}} < \eta_{j3} < \max\eta_{j_{1,2}}$. To isolate the signal, we apply both a dijet invariant mass cut and a $\not{E}_T$ cut:

$$\sqrt{(p_{j_1} + p_{j_1})^2} > M^*_{jj} \qquad \not{E}_T > \not{E}^*_T \tag{7.8}$$

Here, M^*_{jj} and $\not{E}^*_T$ are partially optimized values for the dijet invariant mass and $\not{E}_T$ cuts, chosen at each value of m_ϕ, so as to maximize $S/\sqrt{B}$. Finally, a cut on the azimuthal angle between $\not{E}_T$ and jets is imposed by demanding $|\Delta\phi_{\not{E}_T,j}| > 0.5$. This cut has negligible effects on the results in our case, but is included to ensure that QCD backgrounds are sufficiently suppressed in realistic scenarios.

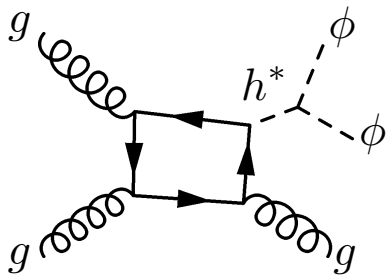

Figure 7.4: An example of the loop processes contributing to the $\not{E}_T + j$ signal from gluon associated production at hadron colliders.

For $\sqrt{s} = 14$ TeV we attempt to account for the anticipated effects of pileup. We simulate pile-up events by overlaying N_a soft-QCD events, drawn from a Poisson distribution with mean $\langle N \rangle_{\rm PU} = 100$, for each event a. The soft-QCD events are generated in `Pythia 8.186` [154]. We find that the inclusion of pileup in this manner roughly decreases the significance by a factor of $2-3$ across different values of m_ϕ. Given that the expected pileup and performance of jet-grooming algorithms is entirely unknown for future colliders, we do not estimate the effects of pileup at $\sqrt{s} = 100$ TeV.

7.3.2 The Higgs Portal in $\not{E}_T + j$ associated production

Next, we consider the sensitivity of searches for the Higgs Portal in the $j + \not{E}_T$ channel via gluon fusion with an associated jet. A sample diagram for this channel is depicted in Fig. 7.4. Although this channel sets a sub-leading limit at $\sqrt{s} = 8$ TeV [234], the increasing gluon partonic luminosity at higher center-of-mass energies makes it a promising channel for future colliders. The primary backgrounds for this process are again Z+jets, W+jets, $t\bar{t}$ + jets, and QCD multijets. Here we simulate Zj and Wj matched up to one additional jet and $t\bar{t}$ matched up to two additional jets, and again do not simulate QCD multijets but adopt a cut flow designed to minimize this background.

As $\sqrt{s} \gg 2m_t$ for the majority of signal events, the HEFT calculation of $gg \to gh^* \to g\phi\phi$ (which is accurate only to lowest order in $1/m_t^2$) is not valid. To correct for this we perform a p_T-dependent reweighting of signal events generated using the HEFT in `MadGraph5`.[6]

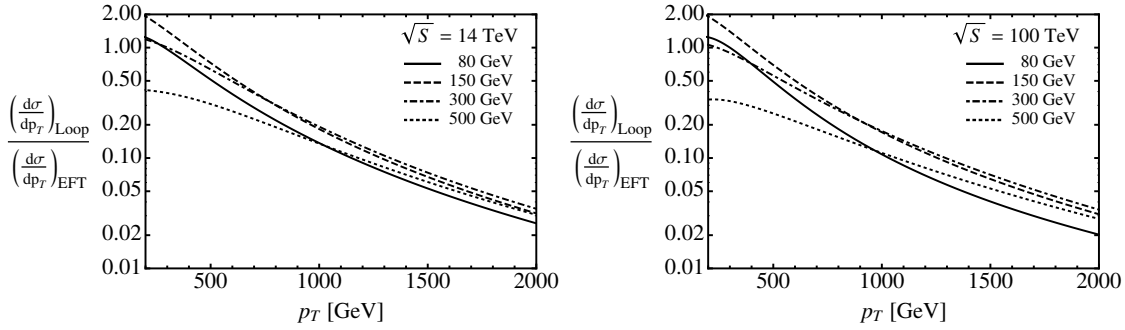

Figure 7.5: The ratio of the differential cross section for $j + \not{E}_T$ for the full one-loop result relative to the HEFT result at 14 and 100 TeV for a variety of singlet scalar masses. When $p_T \sim 2m_t$ there can be an $\mathcal{O}(1)$ enhancement due to the top mass threshold in the loop. At higher $p_T > 2m_T$ the HEFT calculation may overestimate the signal rate significantly.

For the reweighting factor the differential cross section for $gg \to g\phi\phi$ was calculated from the cross section for $gg \to gh^*$ using the factorization of phase space due to the scalar Higgs propagator

$$\frac{d\sigma^{L,EFT}_{gg\to g\phi\phi}(m_\phi)}{dp_T} = \int_{4m_\phi^2}^{\infty} \frac{c_\phi^2}{8\pi^2} \frac{v^2}{(\tilde{s} - m_h^2)^2} \sqrt{1 - \frac{4m_\phi^2}{\tilde{s}}} \frac{d\sigma^{L,EFT}_{gg\to gh^*}}{dp_T} d\sqrt{\tilde{s}} \quad , \tag{7.9}$$

where the superscripts 'L' and 'EFT' denote the one loop and EFT cross sections and $v = 246$ GeV. These parton-level cross sections were convoluted with the MSTW pdfs [8] to determine the proton-proton differential cross section. In a given p_T-bin the reweighting factor is defined as

$$R(p_T^{\rm min}, p_T^{\rm max}, m_\phi) = \frac{\int_{p_T^{\rm min}}^{p_T^{\rm max}} dp_T \frac{d\sigma^L_{pp\to g\phi\phi}(m_\phi)}{dp_T}}{\int_{p_T^{\rm min}}^{p_T^{\rm max}} dp_T \frac{d\sigma^{EFT}_{pp\to g\phi\phi}(m_\phi)}{dp_T}} \tag{7.10}$$

The EFT cross section $\sigma^{EFT}_{gg\to gh^*}$ was calculated using the results of [277, 278] and the cross section incorporating the full loop functions, $\sigma^L_{gg\to gh^*}$, was calculated using the FeynArts, FormCalc, and LoopTools suite of packages [279, 280]. The renormalization and factorization scales were set to the partonic CM energy. In the limit of small partonic CM energy it was checked that the partonic EFT and loop calculations match as expected. As demonstrated in Fig. 7.5, for high CM energies the EFT may overestimate the cross section

[6] For other recent approaches to this problem, see [275, 276].

significantly, thus the suppression factor is significant. Also, when processes at $\sqrt{s} \sim 2m_t$ contribute significantly to the signal phase space the EFT calculation may underestimate the signal by $\mathcal{O}(10\text{'s}\%)$.

To investigate the search sensitivity in this channel, we require at least one jet in the event and apply the following cuts to signal and background at $\sqrt{s} = 14, 100$ TeV:

$$p_{Tj_1} > 110\,\text{GeV} \qquad |\eta_{j_1}| < 2.4 \qquad \not{E}_T > 300\,\text{GeV} \tag{7.11}$$

The restrictive η_{j_1} cut is chosen pragmatically to expedite the calculation of re-weighting factors, and in practice could be relaxed. Since we do not have enough computational power for generating enough QCD background events, we include an additional jet veto analogous to the ones applied in CMS monojet searches [281]. A second jet with $p_{Tj_2} > 30$ GeV is allowed as long as $\Delta R_{j_1,j_2} < 2.4$, otherwise the event is vetoed. Events containing additional jets with $p_{Tj} > 30$ GeV are vetoed, as are events containing an isolated lepton candidate. It is possible that QCD multi-jet backgrounds at $\sqrt{s} = 100$ TeV will favor harder $\not{E}_T$ cuts than those applied here, but reliable simulation of such backgrounds is beyond the capacity of this study.

To compensate for inadequacies in the HEFT approximation in the event generation, we finally apply the appropriate re-weighting factors as defined in (7.10). Due to the relatively rapid fall-off of the jet p_T spectrum in the re-weighted signal events, no meaningful improvement of signal significance can be obtained from applying harder p_T and $\not{E}_T$ cuts to the simulated backgrounds as a function of m_ϕ.

7.3.3 The Higgs Portal in $\not{E}_T + t\bar{t}$ associated production

Finally, we consider the sensitivity of searches for the Higgs Portal in the $t\bar{t} + \not{E}_T$ channel. This channel sets a promising limit on invisible Higgs decays at $\sqrt{s} = 8$ TeV [237], suggesting it may potentially be interesting in future Higgs Portal searches at the LHC and beyond. The dominant backgrounds in this channel are expected to be $t\bar{t}$+jets and W+jets. To improve statistics, we separately simulate semi-leptonic and di-leptonic decays for the $t\bar{t}$ background matched up to two additional jets, while we simulate leptonic Wjj matched up

to two additional jets. To extract the sensitivity in this channel, we first apply the following requirements:

$$n_{\text{jet}} \geq 4 \qquad |\eta_{j_{1,2,3,4}}| < 2.4 \qquad \not{E}_T > 300 \text{ GeV} \tag{7.12}$$

In addition, we require exactly one isolated $e^{\pm}/\mu^{\pm}$ with

$$P_T^{\ell} > 10 \text{ GeV}$$

and at least one b-tag among the leading four jets. We also require that the transverse mass between the lepton and $\not{E}_T$ is constrained to $m_T > 200$ GeV and that $M_{T2}^W > 200\,\text{GeV}$ [282].

7.4 Results and Discussion

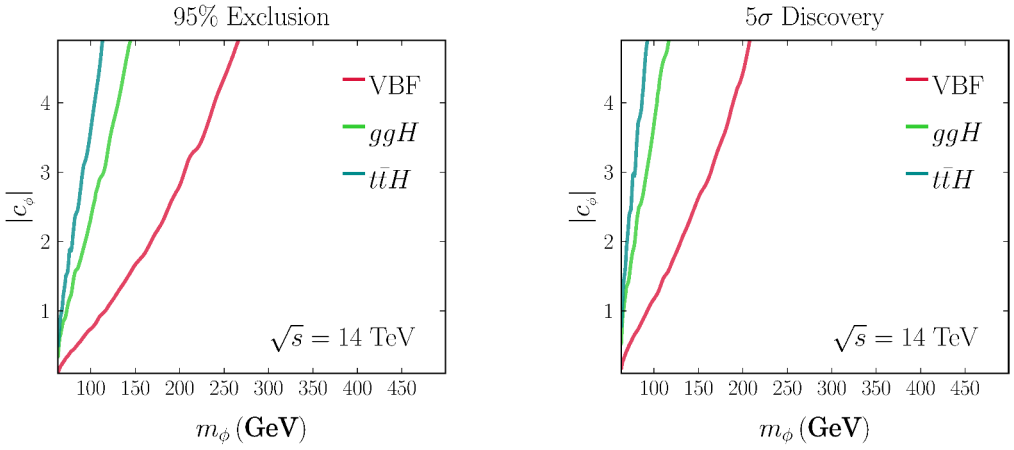

Figure 7.6: Left: 95% exclusion reach in all three channels at $\sqrt{s} = 14$ TeV determined from $S/\sqrt{S+B} = 1.96$, neglecting systematic errors. Right: 5σ discovery reach in the VBF and monojet channels at $\sqrt{s} = 14$ TeV determined from $S/\sqrt{B} = 5$, again neglecting systematic errors.

We have performed a simple cut and count analysis following the cut flows for the searches outlined in Sections 7.3.1, 7.3.2, and 7.3.3. For $\sqrt{s} = 14$ TeV we assume an integrated luminosity of 3 ab^{-1}. For $\sqrt{s} = 100$ TeV we consider scenarios with 3 ab^{-1} and 30 ab^{-1}, respectively. We compute the significance of a search in terms of signal events S

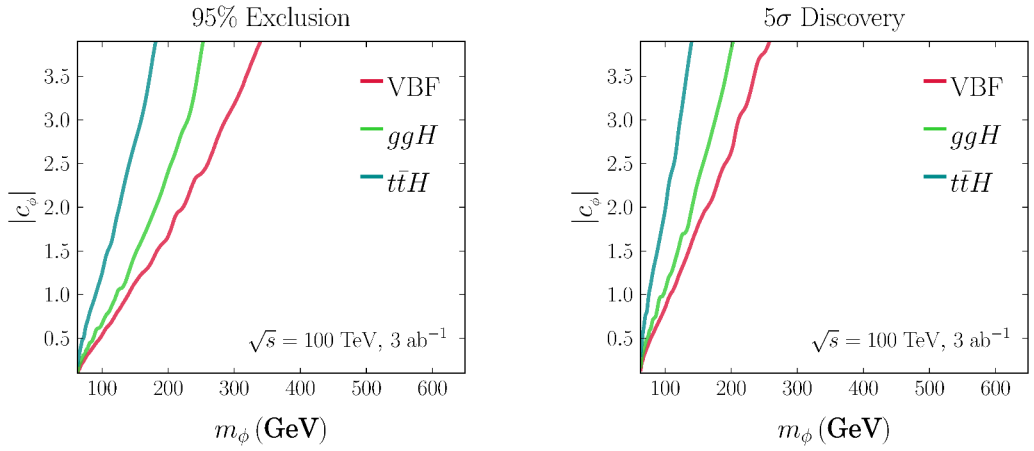

Figure 7.7: Left: 95% exclusion reach in all three channels with 3 ab^{-1} at $\sqrt{s} = 100$ TeV determined from $S/\sqrt{S+B} = 1.96$, neglecting systematic errors. Right: 5σ discovery reach in the VBF and monojet channels with 3 ab^{-1} at $\sqrt{s} = 100$ TeV determined from $S/\sqrt{B} = 5$, again neglecting systematic errors.

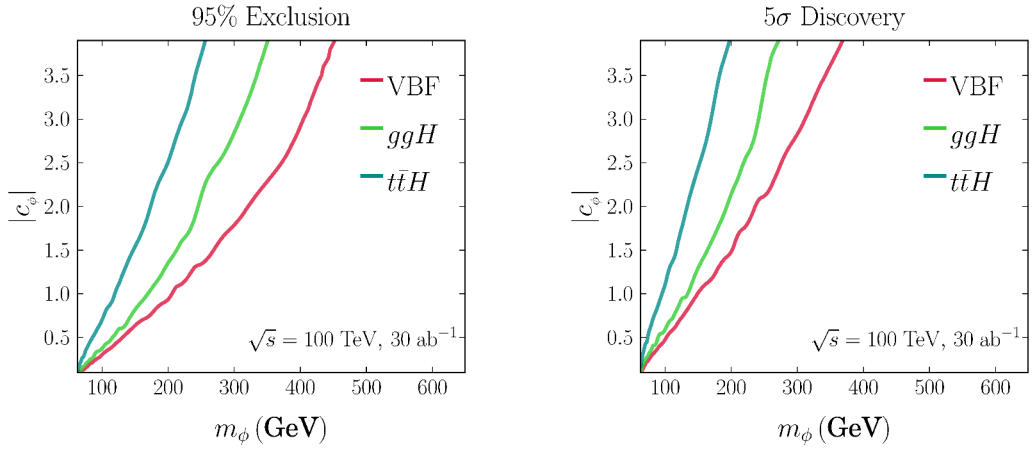

Figure 7.8: Left: 95% exclusion reach in all three channels with 30 ab^{-1} at $\sqrt{s} = 100$ TeV determined from $S/\sqrt{S+B} = 1.96$, neglecting systematic errors. Right: 5σ discovery reach in the VBF and monojet channels with 30 ab^{-1} at $\sqrt{s} = 100$ TeV determined from $S/\sqrt{B} = 5$, again neglecting systematic errors.

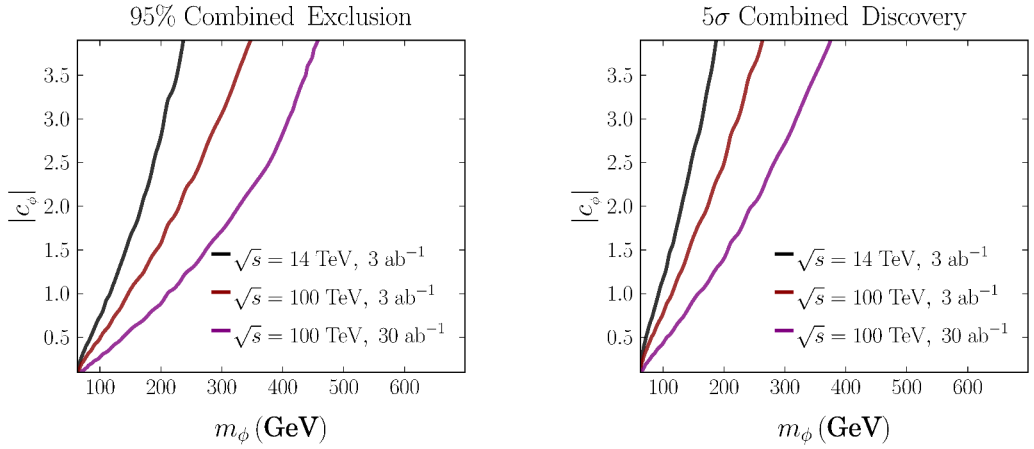

Figure 7.9: Left: Approximate 95% exclusion reach from the combination of VBF, ggH and $t\bar{t}H$ channels with 3 ab^{-1} at $\sqrt{s} = 14$ and 3, 30 ab^{-1} at $\sqrt{s} = 100$ TeV determined from $S/\sqrt{B} = 1.96$, neglecting systematic errors and correlations between channels. Right: Approximate 5σ discovery reach from the same combination at $\sqrt{s} = 14, 100$ TeV.

and background events B passing cuts as

$$\text{Exclusion Sign.} = \frac{S}{\sqrt{S+B}} \qquad \text{Discovery Sign.} = \frac{S}{\sqrt{B}} \tag{7.13}$$

neglecting systematic uncertainties in the signal and background estimates. In principle, systematic uncertainties in background determination could have a substantial impact at $\sqrt{s} = 100$ TeV since S/B is quite small. However, in practice one expects data-driven determination of Z+jets and other backgrounds to substantially lower systematic uncertainties by the 100 TeV era.

Results for the exclusion and discovery reach of the VBF, monojet, and $t\bar{t}$ searches at $\sqrt{s} = 14$ TeV are presented in Fig. 7.6. For the VBF channel at 14 TeV, our preliminary study of pileup effects indicates that $S/\sqrt{B}$ is reduced approximately by a factor of $2-3$ for $\langle N \rangle_{\text{PU}} \sim 100$. This may potentially be mitigated through the use of next-generation jet-grooming algorithms (see for example [283–285]). As expected, all three channels improve significantly over the $\sqrt{s} = 8$ TeV VBF reach, while the VBF channel substantially outperforms the monojet and $t\bar{t}$ channels at $\sqrt{s} = 14$ TeV.

The corresponding results for VBF, monojet, and $t\bar{t}$ searches at $\sqrt{s} = 100$ TeV are presented in Figs. 7.7 and 7.8 for the 3 ab^{-1} and 30 ab^{-1} scenarios, respectively. Here we

do not include pileup estimates, as the operating parameters and efficacy of jet-grooming algorithms are entirely unknown. The reach of the VBF search is in fairly good agreement with the simplified analysis in [236], with a modest reduction in sensitivity due to the additional backgrounds considered here. Surprisingly, at $\sqrt{s} = 100$ TeV the monojet search exhibits more comparable sensitivity to the VBF search for $m_\phi \lesssim 200$ GeV, due in part to the effects of increased gluon PDF luminosity and the relatively low jet p_T cuts relative to the center of mass energy. We caution that some of this sensitivity may be an artifact of our fixed-order calculation for the monojet signal, and furthermore neglects possible contributions from QCD multijet backgrounds that may be appreciable in this case. On the other hand, we have not included a K-factor for gluon fusion associated production, which would further enhance sensitivity. On the whole, our results suggest that the monojet + missing energy channel may be useful at $\sqrt{s} = 100$ TeV and warrants further study. In contrast, the $t\bar{t}$ associated production search demonstrates relatively poor sensitivity, though there is substantial room for improvement through the use of more sophisticated discriminating variables such as hadronic chi-square [195].

To estimate the reach of a concerted Higgs Portal search program, we present the approximate combined reach of VBF, monojet, and $t\bar{t}$ searches at $\sqrt{s} = 14$ and 100 TeV in Fig. 7.9. We obtain the combination by adding the significance of the VBF, monojet, and $t\bar{t}$ channels in quadrature, neglecting possible correlations between the two channels.

7.4.1 Implications for new physics

Although any reach in the Higgs Portal parameter space is valuable, it is useful to compare the exclusion and discovery reach of searches for Higgs Portal states at pp colliders to the range of masses and couplings motivated by the BSM scenarios discussed in Section 7.2. In Fig. 7.10 the combined reach at 100 TeV for both 3 and 30 ab^{-1} is shown relative to both the reach of Higgs coupling measurements at a circular e^+e^- collider and the motivated parameter space for electroweak baryogenesis, dark matter, and neutral naturalness.

In the case of singlet-assisted electroweak baryogenesis, the combined 2σ exclusion reach

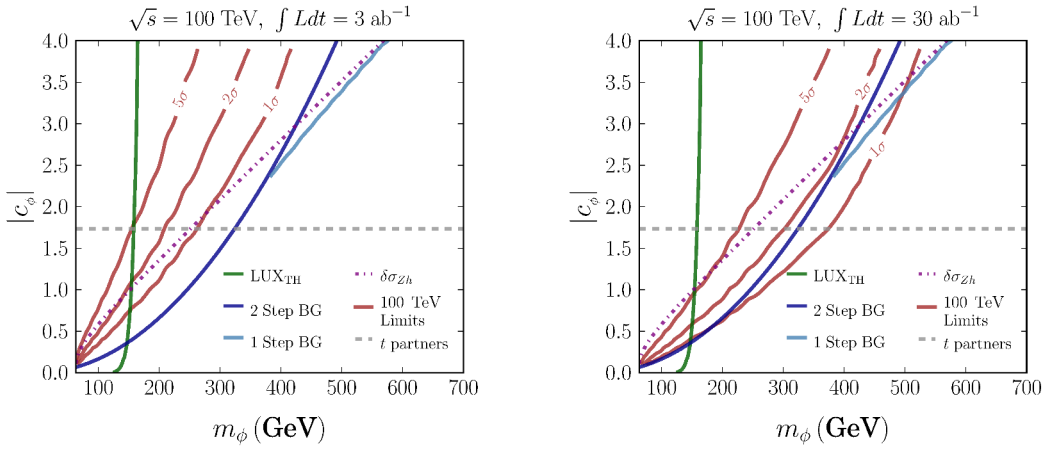

Figure 7.10: Combined reach of direct searches in VBF, ggH and $t\bar{t}H$ channels at $\sqrt{s} = 100$ TeV for 3 ab^{-1} (left) and 30 ab^{-1} (right) compared to select parameter spaces for motivated Higgs Portal scenarios. In each plot the red lines denotes the 1σ exclusion, 2σ exclusion, and 5σ discovery reach from direct searches at $\sqrt{s} = 100$ TeV. The region to the left of the green line denotes the LUX exclusion for Higgs Portal dark matter with thermal abundance given by c_ϕ, m_ϕ. The region to the left of the dark blue line denotes the possible parameter space for two-step baryogenesis, while the region between the light blue and dark blue lines denotes the possible parameter space for one-step baryogenesis (defined by $v_c/T_c \geq 0.6$). The purple line denotes the 2σ contour for $\delta\sigma_{Zh}$ at a future e^+e^- circular collider such as TLEP. The dashed gray line denotes the effective coupling of six complex scalar top partners.

at $\sqrt{s} = 100$ TeV with 30 ab^{-1} covers most of the region of the double-step phase transition. While we cannot decisively exclude some parts of the double-step phase transition or the single-step phase transition with our analysis, there is clearly some sensitivity throughout the region of viable EWBG as evidenced by the 1σ exclusion contour. Given this sensitivity, it may well be that optimized searches at 100 TeV can conclusively exclude (or possibly discover) the scenario. To the extent that this represents the most observationally-challenging scenario for a strongly first-order phase transition, a 100 TeV collider may be well-positioned to decisively settle the question of electroweak baryogenesis.

In the case of dark matter, collider searches for Higgs Portal states are not competitive with dark matter direct detection for small couplings, but at $c_\phi \gtrsim 1$ can exceed the exclusion and discovery reach of the LUX direct detection experiment when the Higgs portal state possesses its natural thermal abundance. In the event of a signal in future direct detection

experiments, this also suggests that direct evidence for Higgs Portal states may be obtained through searches at colliders.

In the case of neutral naturalness, the 2σ exclusion reach extends out to neutral top partners with $m_\phi \sim 300$ GeV with 30 ab^{-1} at $\sqrt{s} = 100$ TeV. This corresponds to a fine-tuning of the weak scale on the order of 30% from the neutral top partners alone [272], and in complete models with neutral top partners the fine-tuning is expected to be considerably worse. Considering that this scenario represents the worst-case scenario for electroweak naturalness (from the perspective of collider signatures), pushing naturalness to the 30% level in this case represents an impressive achievement.

Finally, we can compare the combined reach at 100 TeV to the sensitivity of indirect probes of the Higgs Portal via shifts in the Zh production cross section. The leading order shift due to (7.1) is [238, 239]

$$\delta\sigma_{Zh} = \frac{|c_\phi|^2}{8\pi^2}\frac{v^2}{m_h^2}\left(1 + \frac{1}{4\sqrt{\tau_\phi(\tau_\phi - 1)}}\log\left[\frac{1 - 2\tau_\phi - 2\sqrt{\tau_\phi(\tau_\phi - 1)}}{1 - 2\tau_\phi + 2\sqrt{\tau_\phi(\tau_\phi - 1)}}\right]\right) \tag{7.14}$$

where $\tau_\phi = m_h^2/4m_\phi^2$ and $\delta\sigma_{Zh} = (\sigma_{Zh} - \sigma_{Zh}^{\rm SM})/\sigma_{Zh}^{\rm SM}$. In Fig. 7.10 we compare the 2σ reach at a future $e + e-$ machine such as CEPC/TLEP to the 2σ exclusion reach and 5σ discovery reach at a 100 TeV pp machine, with an eye towards determining whether observed deviations in the Zh cross section may lead to the discovery of new singlet states. We use the Snowmass projections for TLEP sensitivity at $\sqrt{s} = 240$ GeV [240]. The 2σ exclusion reach of a 100 TeV machine is comparable to the equivalent reach at a circular e^+e^- throughout the parameter space under consideration, with direct searches performing better at small couplings and Zh precision performing better at larger coupings. Compellingly, we find that the 5σ discovery reach at a 100 TeV pp machine with 30 ab^{-1} also exceeds the 2σ reach at a circular e^+e^- collider up to $m_\phi \sim 200$ GeV, making a 100 TeV pp machine a powerful tool for direct discovery of a high-mass Higgs Portal in the event of suggestive hints in precision Higgs coupling measurements. Moreover, it implies that for $m_\phi \lesssim 200$ GeV, a 100 TeV machine is capable of discovering a high-mass Higgs Portal even in the absence of suggestive deviations in precision Higgs measurements.

7.5 Conclusions

The discovery of the Higgs boson brings forth qualitatively new opportunities in the search for physics beyond the Standard Model. The Higgs Portal is one of the most salient such opportunities. While efforts so far have focused on the production of Higgs Portal states through the decay of an on-shell Higgs, the complementary case of producing heavier states via an off-shell Higgs is relatively unexplored. In this chapter we have commenced the systematic study of sensitivity to Higgs Portal states above threshold at both the LHC and potential future 100 TeV colliders. We have considered optimized searches in a variety of associated production modes, including vector boson fusion, gluon associated production, and $t\bar{t}$ associated production. We have taken particular care to correctly treat the effects of departure from the EFT limit in gluon associated production by appropriately re-weighting the results of leading-order HEFT Monte Carlo simulation.

Although the reach at 14 TeV is necessarily limited, there is nonetheless sufficient sensitivity to warrant optimized searches for heavy Higgs Portal states at Run 2. Searches at 100 TeV have the potential to substantially explore the Higgs Portal in regions of parameter space strongly motivated by physics beyond the Standard Model. In particular, regions motivated by dark matter, electroweak baryogenesis, and neutral naturalness can be effectively covered by searches for off-shell associated production of the Higgs. At the level of our analysis, the most promising channel appears to be vector boson fusion, but gluon- and $t\bar{t}$-associated production may also contribute substantial significance. The performance of mono-Higgs searches at 100 TeV, which we have omitted here, warrants further study. Searches in these channels also have the potential to directly discover or exclude Higgs Portal explanations of possible deviations in precision Higgs coupling measurements.

7.6 Electroweak Baryogenesis

In this Section we sketch the details of our calculation of the viable parameter space for singlet-assisted electroweak baryogenesis. We work in the Lorentz gauge, where the gauge

fixing parameter is $\xi = 1$. The one-loop potential will include physical particles as well as goldstone bosons. The thermal potential is given by

$$V(h,T) = V_{\text{tree}} + V_{\text{CW}} + V_{\text{thermal}} + V_{\text{resum}} \tag{7.15}$$

where $V_{\text{tree}} = -\mu^2 h^2/2 + \lambda h^2/4$. V_{CW} is the one-loop zero temperature Coleman-Weinberg potential given by

$$V_{\text{CW}} = \sum_i \frac{(-1)^F}{64\pi^2} m_i^4(h) \left(\log \frac{m_i^2(h)}{m_i^2(v)} - \frac{3}{2} + \frac{2m_i^2(v)}{m_i^2(h)} \right) \tag{7.16}$$

where the sum is over all degrees of freedom. The thermal potential is given by

$$V_{\text{thermal}} = T^4 \sum_i J_{F,B}(m_i(h)/T) = T^4 \sum_i \frac{(-1)^F}{2\pi^2} \int_0^\infty dx\, x^2 \log \left[1 - (-1)^F e^{\sqrt{x^2 + m_i^2(h)/T^2}} \right] \tag{7.17}$$

In practical calculations, we expand the thermal integral $J_{F,B}(x)$ up to order x^6 in the small x limit matched to bessel functions at large x. At larger temperature, there are infrared divergences that need to be resummed. The leading order resummed term is given by

$$V_{\text{resum}}(h,T) = \sum_{i \in \text{Boson}} \frac{T}{2\pi} \text{Tr} \left[m_i^3(h) + \Pi_i^{3/2} - (m_i^2(h) + \Pi_i)^{3/2} \right] \tag{7.18}$$

where Π_i are the thermal masses. They are non-zero only for the higgs boson, goldstone, longitudinal gauge bosons and the ϕ scalar. The Π_i are given by

$$\begin{aligned} \Pi_h = \Pi_{\text{Goldstone}} &= T^2 \left(\frac{3}{16} g^2 + \frac{1}{16} g'^2 + \frac{1}{4} y_t^2 + \frac{1}{2} \lambda + \frac{1}{12} c_\phi \right) \\ \Pi_S = \frac{T^2}{3} c_\phi \qquad \Pi_{W_L} &= T^2 \frac{11}{6} g^2 \qquad \Pi_{B_L} = T^2 \frac{11}{6} g'^2 \,. \end{aligned} \tag{7.19}$$

Part IV

Final Conclusion

In this thesis, we have reviewed the Standard Model and covered many topics in collider physics. In Part I, we reviewed the basics of the SM and collider physics at the LHC. We saw how the SM describes all the matter we see and its electroweak and strong interactions. We also saw how the theory has an unnatural tuning, which leads us to suspect that there may be new physics discoverable by collider experiments. The Large Hadron Collider is the machine that has been charged with the task of discovering such new physics. In Part II, we studied many scenarios that could lead to new physics hidden under traditional search strategies. We saw how new physics can defy conventional assumptions. For example, the $\vec{\not{E}}_T$ may be absent in supersymmetry. New physics in the Higgs sector could lead to displaced vertices. Dark matter could lead to $\vec{\not{E}}_T$ correlated with jet momentum. In all of these cases, new effective search strategies can be developed. Finally, in Part III, we studied the performance of future 100 TeV colliders in stops and higgs portal searches. In both cases, 100 TeV results offer significant improvements over projected 14 TeV LHC performances. With the starting of the 14 TeV LHC run, there is great potential for physics discoveries. Nature may once again surprise us with unexpected signals, and it is imperative that we seize all the available opportunities to find these signals. There may still be physics undercover at the LHC, awaiting the right analysis and proper interpretation.

References

[1] **Particle Data Group** Collaboration, K. Olive *et al.*, "Review of Particle Physics," *Chin.Phys.* **C38** (2014) 090001.

[2] **CMS** Collaboration, S. Chatrchyan *et al.*, "Observation of a new boson with mass near 125 GeV in pp collisions at $\sqrt{s} = 7$ and 8 TeV," *JHEP* **1306** (2013) 081, arXiv:1303.4571 [hep-ex].

[3] **ATLAS** Collaboration, G. Aad *et al.*, "Observation of a new particle in the search for the Standard Model Higgs boson with the ATLAS detector at the LHC," *Phys.Lett.* **B716** (2012) 1–29, arXiv:1207.7214 [hep-ex].

[4] **ATLAS, CMS** Collaboration, G. Aad *et al.*, "Combined Measurement of the Higgs Boson Mass in *pp* Collisions at $\sqrt{s} = 7$ and 8 TeV with the ATLAS and CMS Experiments," *Phys.Rev.Lett.* **114** (2015) 191803, arXiv:1503.07589 [hep-ex].

[5] S. R. Coleman and E. J. Weinberg, "Radiative Corrections as the Origin of Spontaneous Symmetry Breaking," *Phys.Rev.* **D7** (1973) 1888–1910.

[6] S. P. Martin, "A Supersymmetry primer," *Adv.Ser.Direct.High Energy Phys.* **21** (2010) 1–153, arXiv:hep-ph/9709356 [hep-ph].

[7] M. Schmaltz and D. Tucker-Smith, "Little Higgs review," *Ann.Rev.Nucl.Part.Sci.* **55** (2005) 229–270, arXiv:hep-ph/0502182 [hep-ph].

[8] A. Martin, W. Stirling, R. Thorne, and G. Watt, "Parton distributions for the LHC," *Eur.Phys.J.* **C63** (2009) 189–285, arXiv:0901.0002 [hep-ph].

[9] A. L. Read, "Presentation of search results: the cl s technique," *Journal of Physics G: Nuclear and Particle Physics* **28** (2002) no. 10, 2693. http://stacks.iop.org/0954-3899/28/i=10/a=313.

[10] **CMS** Collaboration, G. Bayatian *et al.*, "CMS physics: Technical design report,".

[11] M. Cacciari, G. P. Salam, and G. Soyez, "The Anti-k(t) jet clustering algorithm," *JHEP* **0804** (2008) 063, arXiv:0802.1189 [hep-ph].

[12] S. Bentvelsen and I. Meyer, "The Cambridge jet algorithm: Features and applications," *Eur.Phys.J.* **C4** (1998) 623–629, arXiv:hep-ph/9803322 [hep-ph].

[13] T. Sjostrand, P. Eden, C. Friberg, L. Lonnblad, G. Miu, *et al.*, "High-energy physics event generation with PYTHIA 6.1," *Comput.Phys.Commun.* **135** (2001) 238–259, arXiv:hep-ph/0010017 [hep-ph].

[14] T. Gleisberg, S. Hoeche, F. Krauss, M. Schonherr, S. Schumann, *et al.*, "Event generation with SHERPA 1.1," *JHEP* **0902** (2009) 007, arXiv:0811.4622 [hep-ph].

[15] P. Z. Skands, "QCD for Collider Physics," arXiv:1104.2863 [hep-ph].

[16] T. Cohen, E. Izaguirre, M. Lisanti, and H. K. Lou, "Jet Substructure by Accident," *JHEP* **1303** (2013) 161, arXiv:1212.1456 [hep-ph].

[17] V. Halyo, H. K. Lou, P. Lujan, and W. Zhu, "Data driven search in the displaced $b\bar{b}$ pair channel for a Higgs boson decaying to long-lived neutral particles," *JHEP* **1401** (2014) 140, arXiv:1308.6213 [hep-ph].

[18] T. Cohen, M. Lisanti, and H. K. Lou, "Semi-visible Jets: Dark Matter Undercover at the LHC," arXiv:1503.00009 [hep-ph].

[19] G. P. Salam, "Towards Jetography," *Eur.Phys.J.* **C67** (2010) 637–686, arXiv:0906.1833 [hep-ph].

[20] A. Abdesselam, E. B. Kuutmann, U. Bitenc, G. Brooijmans, J. Butterworth, *et al.*, "Boosted objects: A Probe of beyond the Standard Model physics," *Eur.Phys.J.* **C71** (2011) 1661, arXiv:1012.5412 [hep-ph].

[21] A. Altheimer, S. Arora, L. Asquith, G. Brooijmans, J. Butterworth, *et al.*, "Jet Substructure at the Tevatron and LHC: New results, new tools, new benchmarks," *J.Phys.* **G39** (2012) 063001, arXiv:1201.0008 [hep-ph].

[22] J. M. Butterworth, A. R. Davison, M. Rubin, and G. P. Salam, "Jet substructure as a new Higgs search channel at the LHC," *Phys.Rev.Lett.* **100** (2008) 242001, arXiv:0802.2470 [hep-ph].

[23] J. Butterworth, J. R. Ellis, and A. Raklev, "Reconstructing sparticle mass spectra using hadronic decays," *JHEP* **0705** (2007) 033, arXiv:hep-ph/0702150 [HEP-PH].

[24] J. Thaler and L.-T. Wang, "Strategies to Identify Boosted Tops," *JHEP* **0807** (2008) 092, arXiv:0806.0023 [hep-ph].

[25] L. G. Almeida, S. J. Lee, G. Perez, I. Sung, and J. Virzi, "Top Jets at the LHC," *Phys.Rev.* **D79** (2009) 074012, arXiv:0810.0934 [hep-ph].

[26] D. E. Kaplan, K. Rehermann, M. D. Schwartz, and B. Tweedie, "Top Tagging: A Method for Identifying Boosted Hadronically Decaying Top Quarks," *Phys.Rev.Lett.* **101** (2008) 142001, arXiv:0806.0848 [hep-ph].

[27] S. D. Ellis, C. K. Vermilion, and J. R. Walsh, "Techniques for improved heavy particle searches with jet substructure," *Phys.Rev.* **D80** (2009) 051501, arXiv:0903.5081 [hep-ph].

[28] T. Plehn, G. P. Salam, and M. Spannowsky, "Fat Jets for a Light Higgs," *Phys.Rev.Lett.* **104** (2010) 111801, arXiv:0910.5472 [hep-ph].

[29] D. Krohn, J. Thaler, and L.-T. Wang, "Jet Trimming," *JHEP* **1002** (2010) 084, arXiv:0912.1342 [hep-ph].

[30] G. D. Kribs, A. Martin, T. S. Roy, and M. Spannowsky, "Discovering the Higgs Boson in New Physics Events using Jet Substructure," *Phys.Rev.* **D81** (2010) 111501, arXiv:0912.4731 [hep-ph].

[31] T. Plehn and M. Spannowsky, "Top Tagging," *J.Phys.* **G39** (2012) 083001, arXiv:1112.4441 [hep-ph].

[32] J. Thaler and K. Van Tilburg, "Identifying Boosted Objects with N-subjettiness," *JHEP* **1103** (2011) 015, arXiv:1011.2268 [hep-ph].

[33] J. Gallicchio and M. D. Schwartz, "Seeing in Color: Jet Superstructure," *Phys.Rev.Lett.* **105** (2010) 022001, arXiv:1001.5027 [hep-ph].

[34] J. Gallicchio, J. Huth, M. Kagan, M. D. Schwartz, K. Black, *et al.*, "Multivariate discrimination and the Higgs + W/Z search," *JHEP* **1104** (2011) 069, arXiv:1010.3698 [hep-ph].

[35] Y. Cui, Z. Han, and M. D. Schwartz, "W-jet Tagging: Optimizing the Identification of Boosted Hadronically-Decaying W Bosons," *Phys.Rev.* **D83** (2011) 074023, arXiv:1012.2077 [hep-ph].

[36] L. G. Almeida, S. J. Lee, G. Perez, G. Sterman, and I. Sung, "Template Overlap Method for Massive Jets," *Phys.Rev.* **D82** (2010) 054034, arXiv:1006.2035 [hep-ph].

[37] J. Thaler and K. Van Tilburg, "Maximizing Boosted Top Identification by Minimizing N-subjettiness," *JHEP* **1202** (2012) 093, arXiv:1108.2701 [hep-ph].

[38] A. Hook, M. Jankowiak, and J. G. Wacker, "Jet Dipolarity: Top Tagging with Color Flow," *JHEP* **1204** (2012) 007, arXiv:1102.1012 [hep-ph].

[39] J. Gallicchio and M. D. Schwartz, "Quark and Gluon Tagging at the LHC," *Phys.Rev.Lett.* **107** (2011) 172001, arXiv:1106.3076 [hep-ph].

[40] D. E. Soper and M. Spannowsky, "Finding physics signals with shower deconstruction," *Phys.Rev.* **D84** (2011) 074002, arXiv:1102.3480 [hep-ph].

[41] M. Jankowiak and A. J. Larkoski, "Jet Substructure Without Trees," *JHEP* **1106** (2011) 057, arXiv:1104.1646 [hep-ph].

[42] S. D. Ellis, A. Hornig, T. S. Roy, D. Krohn, and M. D. Schwartz, "Qjets: A Non-Deterministic Approach to Tree-Based Jet Substructure," *Phys.Rev.Lett.* **108** (2012) 182003, arXiv:1201.1914 [hep-ph].

[43] M. Jankowiak and A. J. Larkoski, "Angular Scaling in Jets," *JHEP* **1204** (2012) 039, arXiv:1201.2688 [hep-ph].

[44] Z. Han, A. Katz, M. Son, and B. Tweedie, "Boosting searches for natural supersymmetry with R-parity violation via gluino cascades," *Phys.Rev.* **D87** (2013) no. 7, 075003, arXiv:1211.4025 [hep-ph].

[45] D. E. Soper and M. Spannowsky, "Finding top quarks with shower deconstruction," *Phys.Rev.* **D87** (2013) 054012, arXiv:1211.3140 [hep-ph].

[46] **D0** Collaboration, V. M. Abazov *et al.*, "Measurement of color flow in $\mathbf{t\bar{t}}$ events from $\mathbf{p\bar{p}}$ collisions at $\sqrt{\mathbf{s}} = \mathbf{1.96}$ TeV," *Phys.Rev.* **D83** (2011) 092002, arXiv:1101.0648 [hep-ex].

[47] **CDF** Collaboration, T. Aaltonen *et al.*, "Study of Substructure of High Transverse Momentum Jets Produced in Proton-Antiproton Collisions at $\sqrt{s} = 1.96$ TeV," *Phys.Rev.* **D85** (2012) 091101, arXiv:1106.5952 [hep-ex].

[48]

[49] **ATLAS** Collaboration, "Measurement of Jet Mass and Substructure for Inclusive Jets in s = 7 TeV pp Collisions with the ATLAS Experiment,".

[50] **ATLAS** Collaboration, "Performance of large-R jets and jet substructure reconstruction with the ATLAS detector,".

[51] **ATLAS** Collaboration, G. Aad *et al.*, "Jet mass and substructure of inclusive jets in $\sqrt{s} = 7$ TeV pp collisions with the ATLAS experiment," *JHEP* **1205** (2012) 128, arXiv:1203.4606 [hep-ex].

[52] **ATLAS** Collaboration, G. Aad *et al.*, "Study of Jet Shapes in Inclusive Jet Production in pp Collisions at $\sqrt{s} = 7$ TeV using the ATLAS Detector," *Phys.Rev.* **D83** (2011) 052003, arXiv:1101.0070 [hep-ex].

[53] **ATLAS** Collaboration, G. Aad *et al.*, "ATLAS measurements of the properties of jets for boosted particle searches," *Phys.Rev.* **D86** (2012) 072006, arXiv:1206.5369 [hep-ex].

[54] **CMS** Collaboration, S. Chatrchyan *et al.*, "Shape, Transverse Size, and Charged Hadron Multiplicity of Jets in pp Collisions at 7 TeV," *JHEP* **1206** (2012) 160, arXiv:1204.3170 [hep-ex].

[55] **ATLAS** Collaboration, G. Aad *et al.*, "Search for pair production of massive particles decaying into three quarks with the ATLAS detector in $\sqrt{s} = 7$ TeV pp collisions at the LHC," *JHEP* **1212** (2012) 086, arXiv:1210.4813 [hep-ex].

[56] D. Curtin, R. Essig, and B. Shuve, "Boosted Multijet Resonances and New Color-Flow Variables," *Phys.Rev.* **D88** (2013) 034019, arXiv:1210.5523 [hep-ph].

[57]

[58] **CMS** Collaboration, C. Collaboration, "Search for Multijet Resonances in the 8-jet Final State,".

[59] E. Gerwick, T. Plehn, S. Schumann, and P. Schichtel, "Scaling Patterns for QCD Jets," *JHEP* **1210** (2012) 162, arXiv:1208.3676 [hep-ph].

[60] E. Gerwick, S. Schumann, B. Gripaios, and B. Webber, "QCD Jet Rates with the Inclusive Generalized kt Algorithms," *JHEP* **1304** (2013) 089, arXiv:1212.5235.

[61] J. Fan, M. Reece, and J. T. Ruderman, "Stealth Supersymmetry," *JHEP* **1111** (2011) 012, arXiv:1105.5135 [hep-ph].

[62] J. Fan, M. Reece, and J. T. Ruderman, "A Stealth Supersymmetry Sampler," *JHEP* **1207** (2012) 196, arXiv:1201.4875 [hep-ph].

[63] C. Kilic, T. Okui, and R. Sundrum, "Vectorlike Confinement at the LHC," *JHEP* **1002** (2010) 018, arXiv:0906.0577 [hep-ph].

[64] C. Gross, G. Marques Tavares, M. Schmaltz, and C. Spethmann, "Light axigluon explanation of the Tevatron $t\bar{t}$ asymmetry and multijet signals at the LHC," *Phys.Rev.* **D87** (2013) no. 1, 014004, arXiv:1209.6375 [hep-ph].

[65] J. Kang and M. A. Luty, "Macroscopic Strings and 'Quirks' at Colliders," *JHEP* **0911** (2009) 065, arXiv:0805.4642 [hep-ph].

[66] K. Cheung, W.-Y. Keung, and T.-C. Yuan, "Phenomenology of iquarkonium," *Nucl.Phys.* **B811** (2009) 274–287, arXiv:0810.1524 [hep-ph].

[67] R. Barbier, C. Berat, M. Besancon, M. Chemtob, A. Deandrea, *et al.*, "R-parity violating supersymmetry," *Phys.Rept.* **420** (2005) 1–202, arXiv:hep-ph/0406039 [hep-ph].

[68] C. Brust, A. Katz, and R. Sundrum, "SUSY Stops at a Bump," *JHEP* **1208** (2012) 059, arXiv:1206.2353 [hep-ph].

[69] **CMS** Collaboration, C. Collaboration, "A search for the decays of a new heavy particle in multijet events with the razor variables at CMS in pp collisions at sqrt(s)=7 TeV,".

[70] A. Hook, E. Izaguirre, M. Lisanti, and J. G. Wacker, "High Multiplicity Searches at the LHC Using Jet Masses," *Phys.Rev.* **D85** (2012) 055029, arXiv:1202.0558 [hep-ph].

[71] I. W. Stewart, F. J. Tackmann, and W. J. Waalewijn, "N-Jettiness: An Inclusive Event Shape to Veto Jets," *Phys.Rev.Lett.* **105** (2010) 092002, arXiv:1004.2489 [hep-ph].

[72] G. Soyez, G. P. Salam, J. Kim, S. Dutta, and M. Cacciari, "Pileup subtraction for jet shapes," *Phys.Rev.Lett.* **110** (2013) no. 16, 162001, arXiv:1211.2811 [hep-ph].

[73] F. Krauss, R. Kuhn, and G. Soff, "AMEGIC++ 1.0: A Matrix element generator in C++," *JHEP* **0202** (2002) 044, arXiv:hep-ph/0109036 [hep-ph].

[74] S. Schumann and F. Krauss, "A Parton shower algorithm based on Catani-Seymour dipole factorisation," *JHEP* **0803** (2008) 038, arXiv:0709.1027 [hep-ph].

[75] T. Gleisberg and S. Hoeche, "Comix, a new matrix element generator," *JHEP* **0812** (2008) 039, arXiv:0808.3674 [hep-ph].

[76] S. Hoeche, F. Krauss, S. Schumann, and F. Siegert, "QCD matrix elements and truncated showers," *JHEP* **0905** (2009) 053, arXiv:0903.1219 [hep-ph].

[77] S. Catani, F. Krauss, R. Kuhn, and B. Webber, "QCD matrix elements + parton showers," *JHEP* **0111** (2001) 063, arXiv:hep-ph/0109231 [hep-ph].

[78] P. M. Nadolsky, H.-L. Lai, Q.-H. Cao, J. Huston, J. Pumplin, *et al.*, "Implications of CTEQ global analysis for collider observables," *Phys.Rev.* **D78** (2008) 013004, arXiv:0802.0007 [hep-ph].

[79] J. Alwall, M. Herquet, F. Maltoni, O. Mattelaer, and T. Stelzer, "MadGraph 5 : Going Beyond," *JHEP* **1106** (2011) 128, arXiv:1106.0522 [hep-ph].

[80] T. Sjostrand and P. Z. Skands, "Baryon number violation and string topologies," *Nucl.Phys.* **B659** (2003) 243, arXiv:hep-ph/0212264 [hep-ph].

[81] N. Desai and P. Z. Skands, "Supersymmetry and Generic BSM Models in PYTHIA 8," *Eur.Phys.J.* **C72** (2012) 2238, arXiv:1109.5852 [hep-ph].

[82] J. Pumplin, D. Stump, J. Huston, H. Lai, P. M. Nadolsky, *et al.*, "New generation of parton distributions with uncertainties from global QCD analysis," *JHEP* **0207** (2002) 012, arXiv:hep-ph/0201195 [hep-ph].

[83] D. Stump, J. Huston, J. Pumplin, W.-K. Tung, H. Lai, *et al.*, "Inclusive jet production, parton distributions, and the search for new physics," *JHEP* **0310** (2003) 046, arXiv:hep-ph/0303013 [hep-ph].

[84] M. Cacciari and G. P. Salam, "Dispelling the N^3 myth for the k_t jet-finder," *Phys.Lett.* **B641** (2006) 57–61, arXiv:hep-ph/0512210 [hep-ph].

[85] M. Cacciari, G. P. Salam, and G. Soyez, "FastJet User Manual," *Eur.Phys.J.* **C72** (2012) 1896, arXiv:1111.6097 [hep-ph].

[86] W. Beenakker, R. Hopker, M. Spira, and P. Zerwas, "Squark and gluino production at hadron colliders," *Nucl.Phys.* **B492** (1997) 51–103, arXiv:hep-ph/9610490 [hep-ph].

[87] **ATLAS** Collaboration, G. Aad *et al.*, "Measurement of multi-jet cross sections in proton-proton collisions at a 7 TeV center-of-mass energy," *Eur.Phys.J.* **C71** (2011) 1763, arXiv:1107.2092 [hep-ex].

[88] **CMS** Collaboration, S. Chatrchyan *et al.*, "Search for heavy quarks decaying into a top quark and a W or Z boson using lepton + jets events in pp collisions at $\sqrt{s} = 7$ TeV," *JHEP* **1301** (2013) 154, arXiv:1210.7471 [hep-ex].

[89]

[90] **CMS** Collaboration, S. Chatrchyan *et al.*, "Search for microscopic black holes in pp collisions at $\sqrt{s} = 7$ TeV," *JHEP* **1204** (2012) 061, arXiv:1202.6396 [hep-ex].

[91] **ATLAS** Collaboration, G. Aad *et al.*, "Search for TeV-scale gravity signatures in final states with leptons and jets with the ATLAS detector at $\sqrt{s} = 7$ TeV," *Phys.Lett.* **B716** (2012) 122–141, arXiv:1204.4646 [hep-ex].

[92] M. Lisanti, P. Schuster, M. Strassler, and N. Toro, "Study of LHC Searches for a Lepton and Many Jets," *JHEP* **1211** (2012) 081, arXiv:1107.5055 [hep-ph].

[93] **CMS** Collaboration, S. Chatrchyan *et al.*, "Observation of a new boson at a mass of 125 GeV with the CMS experiment at the LHC," *Phys.Lett.* **B716** (2012) 30–61, arXiv:1207.7235 [hep-ex].

[94] **CMS Collaboration** Collaboration, "Combination of standard model Higgs boson searches and measurements of the properties of the new boson with a mass near 125 GeV," Tech. Rep. CMS-PAS-HIG-12-045, CERN, Geneva, 2012. https://cds.cern.ch/record/1494149.

[95] **ATLAS** Collaboration, "Combined coupling measurements of the Higgs-like boson with the ATLAS detector using up to 25 fb^{-1} of proton-proton collision data,".

[96] G. Belanger, B. Dumont, U. Ellwanger, J. Gunion, and S. Kraml, "Status of invisible Higgs decays," *Phys.Lett.* **B723** (2013) 340–347, arXiv:1302.5694 [hep-ph].

[97] J. Ellis and T. You, "Updated Global Analysis of Higgs Couplings," *JHEP* **1306** (2013) 103, arXiv:1303.3879 [hep-ph].

[98] M. J. Strassler and K. M. Zurek, "Discovering the Higgs through highly-displaced vertices," *Phys.Lett.* **B661** (2008) 263–267, arXiv:hep-ph/0605193 [hep-ph].

[99] S. Chang, P. J. Fox, and N. Weiner, "Naturalness and Higgs decays in the MSSM with a singlet," *JHEP* **0608** (2006) 068, arXiv:hep-ph/0511250 [hep-ph].

[100] L. M. Carpenter, D. E. Kaplan, and E.-J. Rhee, "Reduced fine-tuning in supersymmetry with R-parity violation," *Phys.Rev.Lett.* **99** (2007) 211801, arXiv:hep-ph/0607204 [hep-ph].

[101] **D0** Collaboration, V. Abazov *et al.*, "Search for Resonant Pair Production of long-lived particles decaying to b anti-b in p anti-p collisions at s**(1/2) = 1.96-TeV," *Phys.Rev.Lett.* **103** (2009) 071801, arXiv:0906.1787 [hep-ex].

[102] **ATLAS** Collaboration, G. Aad *et al.*, "Search for long-lived, heavy particles in final states with a muon and multi-track displaced vertex in proton-proton collisions at $\sqrt{s} = 7$ TeV with the ATLAS detector," *Phys.Lett.* **B719** (2013) 280–298, arXiv:1210.7451 [hep-ex].

[103] R. Dermisek and J. F. Gunion, "Escaping the large fine tuning and little hierarchy problems in the next to minimal supersymmetric model and h —¿ aa decays," *Phys.Rev.Lett.* **95** (2005) 041801, arXiv:hep-ph/0502105 [hep-ph].

[104] D. Aristizabal Sierra, W. Porod, D. Restrepo, and C. E. Yaguna, "Novel Higgs decay signals in R-parity violating models," *Phys.Rev.* **D78** (2008) 015015, arXiv:0804.1907 [hep-ph].

[105] B. Bellazzini, C. Csaki, A. Falkowski, and A. Weiler, "Buried Higgs," *Phys.Rev.* **D80** (2009) 075008, arXiv:0906.3026 [hep-ph].

[106] J. E. Juknevich, D. Melnikov, and M. J. Strassler, "A Pure-Glue Hidden Valley I. States and Decays," *JHEP* **0907** (2009) 055, arXiv:0903.0883 [hep-ph].

[107] A. Falkowski, J. T. Ruderman, T. Volansky, and J. Zupan, "Hidden Higgs Decaying to Lepton Jets," *JHEP* **1005** (2010) 077, arXiv:1002.2952 [hep-ph].

[108] C. Englert, J. Jaeckel, E. Re, and M. Spannowsky, "Evasive Higgs Maneuvers at the LHC," *Phys.Rev.* **D85** (2012) 035008, arXiv:1111.1719 [hep-ph].

[109] P. W. Graham, D. E. Kaplan, S. Rajendran, and P. Saraswat, "Displaced Supersymmetry," *JHEP* **1207** (2012) 149, arXiv:1204.6038 [hep-ph].

[110] M. J. Strassler and K. M. Zurek, "Echoes of a hidden valley at hadron colliders," *Phys.Lett.* **B651** (2007) 374–379, arXiv:hep-ph/0604261 [hep-ph].

[111] K. T. Matchev and S. D. Thomas, "Higgs and Z boson signatures of supersymmetry," *Phys.Rev.* **D62** (2000) 077702, arXiv:hep-ph/9908482 [hep-ph].

[112] T. Sjostrand, S. Mrenna, and P. Z. Skands, "PYTHIA 6.4 Physics and Manual," *JHEP* **0605** (2006) 026, arXiv:hep-ph/0603175 [hep-ph].

[113] **LHC Higgs Cross Section Working Group** Collaboration, S. Heinemeyer *et al.*, "Handbook of LHC Higgs Cross Sections: 3. Higgs Properties," arXiv:1307.1347 [hep-ph].

[114] M. L. Mangano, M. Moretti, F. Piccinini, and M. Treccani, "Matching matrix elements and shower evolution for top-quark production in hadronic collisions," *JHEP* **0701** (2007) 013, arXiv:hep-ph/0611129 [hep-ph].

[115] **CMS** Collaboration, S. Chatrchyan *et al.*, "Search for a Higgs boson decaying into a b-quark pair and produced in association with b quarks in proton-proton collisions at 7 TeV," *Phys.Lett.* **B722** (2013) 207–232, arXiv:1302.2892 [hep-ex].

[116] **CMS** Collaboration, "Particle-Flow Event Reconstruction in CMS and Performance for Jets, Taus, and MET,".

[117] **CMS** Collaboration, "Tracking and Primary Vertex Results in First 7 TeV Collisions,".

[118] A. Rizzi, F. Palla, and G. Segneri, "Track impact parameter based b-tagging with CMS,".

[119] **CMS** Collaboration, S. Chatrchyan *et al.*, "Identification of b-quark jets with the CMS experiment," *JINST* **8** (2013) P04013, arXiv:1211.4462 [hep-ex].

[120] V. Halyo, A. Hunt, P. Jindal, P. LeGresley, and P. Lujan, "GPU Enhancement of the Trigger to Extend Physics Reach at the LHC," *JINST* **8** (2013) P10005, arXiv:1305.4855 [physics.ins-det].

[121] V. A. Mitsou, "Shedding Light on Dark Matter at Colliders," *Int.J.Mod.Phys.* **A28** (2013) 1330052, arXiv:1310.1072 [hep-ex].

[122] **LHC New Physics Working Group** Collaboration, D. Alves *et al.*, "Simplified Models for LHC New Physics Searches," *J.Phys.* **G39** (2012) 105005, arXiv:1105.2838 [hep-ph].

[123] J. Goodman, M. Ibe, A. Rajaraman, W. Shepherd, T. M. Tait, *et al.*, "Constraints on Light Majorana dark Matter from Colliders," *Phys.Lett.* **B695** (2011) 185–188, arXiv:1005.1286 [hep-ph].

[124] P. J. Fox, R. Harnik, J. Kopp, and Y. Tsai, "Missing Energy Signatures of Dark Matter at the LHC," *Phys.Rev.* **D85** (2012) 056011, arXiv:1109.4398 [hep-ph].

[125] Z. Chacko, H.-S. Goh, and R. Harnik, "The Twin Higgs: Natural electroweak breaking from mirror symmetry," *Phys.Rev.Lett.* **96** (2006) 231802, arXiv:hep-ph/0506256 [hep-ph].

[126] R. Schabinger and J. D. Wells, "A Minimal spontaneously broken hidden sector and its impact on Higgs boson physics at the large hadron collider," *Phys.Rev.* **D72** (2005) 093007, arXiv:hep-ph/0509209 [hep-ph].

[127] G. Burdman, Z. Chacko, H.-S. Goh, and R. Harnik, "Folded supersymmetry and the LEP paradox," *JHEP* **0702** (2007) 009, arXiv:hep-ph/0609152 [hep-ph].

[128] J. March-Russell, S. M. West, D. Cumberbatch, and D. Hooper, "Heavy Dark Matter Through the Higgs Portal," *JHEP* **0807** (2008) 058, arXiv:0801.3440 [hep-ph].

[129] N. Arkani-Hamed, D. P. Finkbeiner, T. R. Slatyer, and N. Weiner, "A Theory of Dark Matter," *Phys.Rev.* **D79** (2009) 015014, arXiv:0810.0713 [hep-ph].

[130] D. E. Kaplan, M. A. Luty, and K. M. Zurek, "Asymmetric Dark Matter," *Phys.Rev.* **D79** (2009) 115016, arXiv:0901.4117 [hep-ph].

[131] G. D. Kribs, T. S. Roy, J. Terning, and K. M. Zurek, "Quirky Composite Dark Matter," *Phys.Rev.* **D81** (2010) 095001, arXiv:0909.2034 [hep-ph].

[132] J. McDonald, "Thermally generated gauge singlet scalars as selfinteracting dark matter," *Phys.Rev.Lett.* **88** (2002) 091304, arXiv:hep-ph/0106249 [hep-ph].

[133] V. Barger, P. Langacker, M. McCaskey, M. J. Ramsey-Musolf, and G. Shaughnessy, "LHC Phenomenology of an Extended Standard Model with a Real Scalar Singlet," *Phys.Rev.* **D77** (2008) 035005, arXiv:0706.4311 [hep-ph].

[134] R. A. Porto and A. Zee, "The Private Higgs," *Phys.Lett.* **B666** (2008) 491–495, arXiv:0712.0448 [hep-ph].

[135] O. Bertolami and R. Rosenfeld, "The Higgs portal and an unified model for dark energy and dark matter," *Int.J.Mod.Phys.* **A23** (2008) 4817–4827, arXiv:0708.1784 [hep-ph].

[136] Y. Hochberg, E. Kuflik, T. Volansky, and J. G. Wacker, "Mechanism for Thermal Relic Dark Matter of Strongly Interacting Massive Particles," *Phys.Rev.Lett.* **113** (2014) 171301, arXiv:1402.5143 [hep-ph].

[137] A. Alves, S. Profumo, and F. S. Queiroz, "The dark $Z^{'}$ portal: direct, indirect and collider searches," *JHEP* **1404** (2014) 063, arXiv:1312.5281 [hep-ph].

[138] M. J. Strassler, "Possible effects of a hidden valley on supersymmetric phenomenology," arXiv:hep-ph/0607160 [hep-ph].

[139] T. Han, Z. Si, K. M. Zurek, and M. J. Strassler, "Phenomenology of hidden valleys at hadron colliders," *JHEP* **0807** (2008) 008, arXiv:0712.2041 [hep-ph].

[140] M. J. Strassler, "On the Phenomenology of Hidden Valleys with Heavy Flavor," arXiv:0806.2385 [hep-ph].

[141] N. Arkani-Hamed and N. Weiner, "LHC Signals for a SuperUnified Theory of Dark Matter," *JHEP* **0812** (2008) 104, arXiv:0810.0714 [hep-ph].

[142] M. Baumgart, C. Cheung, J. T. Ruderman, L.-T. Wang, and I. Yavin, "Non-Abelian Dark Sectors and Their Collider Signatures," *JHEP* **0904** (2009) 014, arXiv:0901.0283 [hep-ph].

[143] S. Chang and M. A. Luty, "Displaced Dark Matter at Colliders," arXiv:0906.5013 [hep-ph].

[144] L. Carloni and T. Sjostrand, "Visible Effects of Invisible Hidden Valley Radiation," *JHEP* **1009** (2010) 105, arXiv:1006.2911 [hep-ph].

[145] L. Carloni, J. Rathsman, and T. Sjostrand, "Discerning Secluded Sector gauge structures," *JHEP* **1104** (2011) 091, arXiv:1102.3795 [hep-ph].

[146] Y. F. Chan, M. Low, D. E. Morrissey, and A. P. Spray, "LHC Signatures of a Minimal Supersymmetric Hidden Valley," *JHEP* **1205** (2012) 155, arXiv:1112.2705 [hep-ph].

[147] **CMS Collaboration** Collaboration, S. Chatrchyan *et al.*, "Search for microscopic black holes in pp collisions at sqrt(s) = 8 TeV," *JHEP* **1307** (2013) 178, arXiv:1303.5338 [hep-ex].

[148] **ATLAS Collaboration** Collaboration, G. Aad *et al.*, "Search for pair-produced third-generation squarks decaying via charm quarks or in compressed supersymmetric scenarios in pp collisions at $\sqrt{s} = 8$ TeV with the ATLAS detector," *Phys.Rev.* **D90** (2014) 052008, arXiv:1407.0608 [hep-ex].

[149] P. Schwaller, D. Stolarski, and A. Weiler, "Emerging Jets," arXiv:1502.05409 [hep-ph].

[150] **CMS Collaboration** Collaboration, S. Chatrchyan *et al.*, "Search for new physics in the multijet and missing transverse momentum final state in proton-proton collisions at $\sqrt{s}$= 8 TeV," *JHEP* **1406** (2014) 055, arXiv:1402.4770 [hep-ex].

[151] **ATLAS Collaboration** Collaboration, G. Aad *et al.*, "Search for squarks and gluinos with the ATLAS detector in final states with jets and missing transverse momentum using $\sqrt{s} = 8$ TeV proton–proton collision data," *JHEP* **1409** (2014) 176, arXiv:1405.7875 [hep-ex].

[152] C. Englert, M. Spannowsky, and C. Wymant, "Partially (in)visible Higgs decays at the LHC," *Phys.Lett.* **B718** (2012) 538–544, arXiv:1209.0494 [hep-ph].

[153] B. Andersson, G. Gustafson, G. Ingelman, and T. Sjostrand, "Parton Fragmentation and String Dynamics," *Phys.Rept.* **97** (1983) 31–145.

[154] T. Sjostrand, S. Mrenna, and P. Z. Skands, "A Brief Introduction to PYTHIA 8.1," *Comput.Phys.Commun.* **178** (2008) 852–867, arXiv:0710.3820 [hep-ph].

[155] **DELPHES 3** Collaboration, J. de Favereau *et al.*, "DELPHES 3, A modular framework for fast simulation of a generic collider experiment," *JHEP* **1402** (2014) 057, arXiv:1307.6346 [hep-ex].

[156] B. Nachman, P. Nef, A. Schwartzman, M. Swiatlowski, and C. Wanotayaroj, "Jets from Jets: Re-clustering as a tool for large radius jet reconstruction and grooming at the LHC," *JHEP* **1502** (2015) 075, arXiv:1407.2922 [hep-ph].

[157] A. Avetisyan, J. M. Campbell, T. Cohen, N. Dhingra, J. Hirschauer, *et al.*, "Methods and Results for Standard Model Event Generation at $\sqrt{s} = 14$ TeV, 33 TeV and 100 TeV Proton Colliders (A Snowmass Whitepaper)," arXiv:1308.1636 [hep-ex].

[158] J. Alwall, R. Frederix, S. Frixione, V. Hirschi, F. Maltoni, *et al.*, "The automated computation of tree-level and next-to-leading order differential cross sections, and their matching to parton shower simulations," *JHEP* **1407** (2014) 079, arXiv:1405.0301 [hep-ph].

[159] G. Cowan, K. Cranmer, E. Gross, and O. Vitells, "Asymptotic formulae for likelihood-based tests of new physics," *Eur.Phys.J.* **C71** (2011) 1554, arXiv:1007.1727 [physics.data-an].

[160] **CMS Collaboration** Collaboration, V. Khachatryan *et al.*, "Search for Narrow Resonances using the Dijet Mass Spectrum with 19.6fb^{-1} of pp Collisions at $\sqrt{s} = 8$ TeV," Tech. Rep. CMS-PAS-EXO-12-059, CERN, Geneva, 2013.

[161] **CMS Collaboration** Collaboration, "MET performance in 8 TeV data," Tech. Rep. CMS-PAS-JME-12-002, CERN, Geneva, 2013.

[162] **ATLAS Collaboration** Collaboration, G. Aad *et al.*, "Search for new phenomena in the dijet mass distribution using pp collision data at $\sqrt{s} = 8$ TeV with the ATLAS detector," arXiv:1407.1376 [hep-ex].

[163] J. Fan, D. Krohn, P. Mosteiro, A. M. Thalapillil, and L.-T. Wang, "Heavy Squarks at the LHC," *JHEP* **1103** (2011) 077, arXiv:1102.0302 [hep-ph].

[164] T. Cohen, R. T. D'Agnolo, M. Hance, H. K. Lou, and J. G. Wacker, "Boosting Stop Searches with a 100 TeV Proton Collider," *JHEP* **1411** (2014) 021, arXiv:1406.4512 [hep-ph].

[165] N. Craig, H. K. Lou, M. McCullough, and A. Thalapillil, "The Higgs Portal Above Threshold," arXiv:1412.0258 [hep-ph].

[166] Y. Gershtein, M. Luty, M. Narain, L. T. Wang, D. Whiteson, *et al.*, "New Particles Working Group Report of the Snowmass 2013 Community Summer Study," arXiv:1311.0299 [hep-ex].

[167] https://indico.cern.ch/event/282344/. Future Circular Collider Study Kick-Off meeting.

[168] http://indico.ihep.ac.cn/conferenceDisplay.py?confId=3813. Workshop on Future High Energy Circular Colliders.

[169] T. Cohen, T. Golling, M. Hance, A. Henrichs, K. Howe, *et al.*, "SUSY Simplified Models at 14, 33, and 100 TeV Proton Colliders," arXiv:1311.6480 [hep-ph].

[170] T. Andeen, C. Bernard, K. Black, T. Childres, L. Dell'Asta, *et al.*, "Sensitivity to the Single Production of Vector-Like Quarks at an Upgraded Large Hadron Collider," arXiv:1309.1888 [hep-ph].

[171] L. Apanasevich, S. Upadhyay, N. Varelas, D. Whiteson, and F. Yu, "Sensitivity of potential future *pp* colliders to quark compositeness," arXiv:1307.7149 [hep-ex].

[172] C. Degrande, J. Holzbauer, S. C. Hsu, A. Kotwal, S. Li, *et al.*, "Studies of Vector Boson Scattering And Triboson Production with DELPHES Parametrized Fast Simulation for Snowmass 2013," arXiv:1309.7452 [physics.comp-ph].

[173] D. Stolarski, "Reach in All Hadronic Stop Decays: A Snowmass White Paper," arXiv:1309.1514 [hep-ph].

[174] F. Yu, "Di-jet resonances at future hadron colliders: A Snowmass whitepaper," arXiv:1308.1077 [hep-ph].

[175] N. Zhou, D. Berge, L. Wang, D. Whiteson, and T. Tait, "Sensitivity of future collider facilities to WIMP pair production via effective operators and light mediators," arXiv:1307.5327 [hep-ex].

[176] M. Low and L.-T. Wang, "Neutralino Dark Matter at 100 TeV," arXiv:1404.0682 [hep-ph].

[177] N. Craig, "The State of Supersymmetry after Run I of the LHC," arXiv:1309.0528 [hep-ph].

[178] S. Dimopoulos and G. Giudice, "Naturalness constraints in supersymmetric theories with nonuniversal soft terms," *Phys.Lett.* **B357** (1995) 573–578, arXiv:hep-ph/9507282 [hep-ph].

[179] A. G. Cohen, D. Kaplan, and A. Nelson, "The More minimal supersymmetric standard model," *Phys.Lett.* **B388** (1996) 588–598, arXiv:hep-ph/9607394 [hep-ph].

[180] N. Arkani-Hamed, M. A. Luty, and J. Terning, "Composite quarks and leptons from dynamical supersymmetry breaking without messengers," *Phys.Rev.* **D58** (1998) 015004, arXiv:hep-ph/9712389 [hep-ph].

[181] N. Craig, D. Green, and A. Katz, "(De)Constructing a Natural and Flavorful Supersymmetric Standard Model," *JHEP* **1107** (2011) 045, arXiv:1103.3708 [hep-ph].

[182] C. Csaki, L. Randall, and J. Terning, "Light Stops from Seiberg Duality," *Phys.Rev.* **D86** (2012) 075009, arXiv:1201.1293 [hep-ph].

[183] G. Larsen, Y. Nomura, and H. L. Roberts, "Supersymmetry with Light Stops," *JHEP* **1206** (2012) 032, arXiv:1202.6339 [hep-ph].

[184] N. Craig, S. Dimopoulos, and T. Gherghetta, "Split families unified," *JHEP* **1204** (2012) 116, arXiv:1203.0572 [hep-ph].

[185] T. Cohen, A. Hook, and G. Torroba, "An Attractor for Natural Supersymmetry," *Phys.Rev.* **D86** (2012) 115005, arXiv:1204.1337 [hep-ph].

[186] L. Randall and M. Reece, "Single-Scale Natural SUSY," *JHEP* **1308** (2013) 088, arXiv:1206.6540 [hep-ph].

[187] R. Essig, E. Izaguirre, J. Kaplan, and J. G. Wacker, "Heavy Flavor Simplified Models at the LHC," *JHEP* **1201** (2012) 074, arXiv:1110.6443 [hep-ph].

[188] M. Papucci, J. T. Ruderman, and A. Weiler, "Natural SUSY Endures," *JHEP* **1209** (2012) 035, arXiv:1110.6926 [hep-ph].

[189] C. Brust, A. Katz, S. Lawrence, and R. Sundrum, "SUSY, the Third Generation and the LHC," *JHEP* **1203** (2012) 103, arXiv:1110.6670 [hep-ph].

[190] G. D. Kribs, A. Martin, and A. Menon, "Natural Supersymmetry and Implications for Higgs physics," *Phys.Rev.* **D88** (2013) 035025, arXiv:1305.1313 [hep-ph].

[191] M. Papucci, K. Sakurai, A. Weiler, and L. Zeune, "Fastlim: a fast LHC limit calculator," arXiv:1402.0492 [hep-ph].

[192] **ATLAS** Collaboration, "Search for direct production of the top squark in the all-hadronic ttbar + etmiss final state in 21 fb-1 of p-pcollisions at sqrt(s)=8 TeV with the ATLAS detector," Tech. Rep. ATLAS-CONF-2013-024, CERN, Geneva, Mar, 2013.

[193] **ATLAS** Collaboration, "Search for direct top squark pair production in final states with one isolated lepton, jets, and missing transverse momentum in $\sqrt{s} = 8$,TeV *pp* collisions using 21 fb^{-1} of ATLAS data," Tech. Rep. ATLAS-CONF-2013-037, CERN, Geneva, Mar, 2013.

[194] **ATLAS** Collaboration, "Searches for direct scalar top pair production in final states with two leptons using the stransverse mass variable and a multivariate analysis technique in $\sqrt{s} = 8$ TeV pp collisions using 20.3 fb^{-1} of ATLAS data," Tech. Rep. ATLAS-CONF-2013-065, CERN, Geneva, Jul, 2013.

[195] **CMS** Collaboration, S. Chatrchyan *et al.*, "Search for top-squark pair production in the single-lepton final state in pp collisions at $\sqrt{s} = 8$ TeV," *Eur.Phys.J.* **C73** (2013) 2677, arXiv:1308.1586 [hep-ex].

[196] **CMS** Collaboration, "Search for supersymmetry using razor variables in events with b-jets in pp collisions at 8 TeV," Tech. Rep. CMS-PAS-SUS-13-004, CERN, Geneva, 2013.

[197] **ATLAS** Collaboration, "Physics at a High-Luminosity LHC with ATLAS," arXiv:1307.7292 [hep-ex].

[198] **CMS** Collaboration, "Projected Performance of an Upgraded CMS Detector at the LHC and HL-LHC: Contribution to the Snowmass Process," arXiv:1307.7135.

[199] J. Anderson, A. Avetisyan, R. Brock, S. Chekanov, T. Cohen, *et al.*, "Snowmass Energy Frontier Simulations," arXiv:1309.1057 [hep-ex].

[200] C. Borschensky, M. Krmer, A. Kulesza, M. Mangano, S. Padhi, *et al.*, "Squark and gluino production cross sections in pp collisions at $\sqrt{s}$ = 13, 14, 33 and 100 TeV," arXiv:1407.5066 [hep-ph].

[201] T. Plehn, M. Spannowsky, M. Takeuchi, and D. Zerwas, "Stop Reconstruction with Tagged Tops," *JHEP* **1010** (2010) 078, arXiv:1006.2833 [hep-ph].

[202] ATLAS, "ATLAS: Detector and physics performance technical design report. Volume 1,".

[203] Y. L. Dokshitzer, G. Leder, S. Moretti, and B. Webber, "Better jet clustering algorithms," *JHEP* **9708** (1997) 001, arXiv:hep-ph/9707323 [hep-ph].

[204] M. Wobisch and T. Wengler, "Hadronization corrections to jet cross-sections in deep inelastic scattering," arXiv:hep-ph/9907280 [hep-ph].

[205] **CDF** Collaboration, D. Acosta *et al.*, "Measurement of the $t\bar{t}$ production cross section in $p\bar{p}$ collisions at $\sqrt{s} = 1.96$ TeV using lepton plus jets events with semileptonic B decays to muons," *Phys.Rev.* **D72** (2005) 032002, arXiv:hep-ex/0506001 [hep-ex].

[206] **D0** Collaboration, V. Abazov *et al.*, "A Search for anomalous heavy-flavor quark production in association with W bosons," *Phys.Rev.Lett.* **94** (2005) 152002, arXiv:hep-ex/0411084 [hep-ex].

[207] **CDF** Collaboration, A. Abulencia *et al.*, "Search for anomalous semileptonic decay of heavy flavor hadrons produced in association with a W boson at CDF II," *Phys.Rev.* **D73** (2006) 051101, arXiv:hep-ex/0512065 [hep-ex].

[208] **CDF** Collaboration, T. Aaltonen *et al.*, "First measurement of the production of a W boson in association with a single charm quark in $p\bar{p}$ collisions at $\sqrt{s} =$ 1.96-TeV," *Phys.Rev.Lett.* **100** (2008) 091803, arXiv:0711.2901 [hep-ex].

[209] **CDF** Collaboration, T. Aaltonen *et al.*, "Measurement of the $t\bar{t}$ Production Cross Section in 2 fb^{-1} of $p\bar{p}$ Collisions at $\sqrt{s} = 1.96$ TeV Using Lepton Plus Jets Events with Soft Muon b-Tagging," *Phys.Rev.* **D79** (2009) 052007, arXiv:0901.4142 [hep-ex].

[210] **CDF** Collaboration, T. Aaltonen *et al.*, "Measurement of the $t\bar{t}$ Production Cross Section in $p\bar{p}$ Collisions at sqrt(s)=1.96 TeV using Soft Electron b-Tagging," *Phys.Rev.* **D81** (2010) 092002, arXiv:1002.3783 [hep-ex].

[211] **ATLAS** Collaboration, G. Aad *et al.*, "Expected Performance of the ATLAS Experiment - Detector, Trigger and Physics," arXiv:0901.0512 [hep-ex].

[212] **ATLAS** Collaboration, "Soft muon tagging and Dstar/mu correlations in 7 TeV collisions with ATLAS,".

[213] "Search for pair-produced top squarks decaying into a charm quark and the lightest neutralinos with 20.3 fb^{-1} of pp collisions at $\sqrt{s} = 8$ TeV with the ATLAS detector at the LHC," Tech. Rep. ATLAS-CONF-2013-068, CERN, Geneva, Jul, 2013.

[214] W. Barletta, M. Battaglia, M. Klute, M. Mangano, S. Prestemon, *et al.*, "Working Group Report: Hadron Colliders," arXiv:1310.0290 [physics.acc-ph].

[215] P. Z. Skands, "Soft-QCD and UE spectra in pp collisions at very high CM energies (a Snowmass white paper)," arXiv:1308.2813 [hep-ph].

[216] J. R. Christiansen and T. Sjstrand, "Weak Gauge Boson Radiation in Parton Showers," arXiv:1401.5238 [hep-ph].

[217] L. Moneta, K. Belasco, K. S. Cranmer, S. Kreiss, A. Lazzaro, *et al.*, "The RooStats Project," *PoS* **ACAT2010** (2010) 057, arXiv:1009.1003 [physics.data-an].

[218] G. Salam and A. Weiler. http://collider-reach.web.cern.ch.

[219] G. Giudice and R. Rattazzi, "Theories with gauge mediated supersymmetry breaking," *Phys.Rept.* **322** (1999) 419–499, arXiv:hep-ph/9801271 [hep-ph].

[220] G. F. Giudice, M. A. Luty, H. Murayama, and R. Rattazzi, "Gaugino mass without singlets," *JHEP* **9812** (1998) 027, arXiv:hep-ph/9810442 [hep-ph].

[221] L. Randall and R. Sundrum, "Out of this world supersymmetry breaking," *Nucl.Phys.* **B557** (1999) 79–118, arXiv:hep-th/9810155 [hep-th].

[222] Z. Chacko, M. A. Luty, A. E. Nelson, and E. Ponton, "Gaugino mediated supersymmetry breaking," *JHEP* **0001** (2000) 003, arXiv:hep-ph/9911323 [hep-ph].

[223] P. Draper, G. Lee, and C. E. M. Wagner, "Precise Estimates of the Higgs Mass in Heavy SUSY," *Phys.Rev.* **D89** (2014) 055023, arXiv:1312.5743 [hep-ph].

[224] V. Silveira and A. Zee, "SCALAR PHANTOMS," *Phys.Lett.* **B161** (1985) 136.

[225] J. McDonald, "Gauge singlet scalars as cold dark matter," *Phys.Rev.* **D50** (1994) 3637–3649, arXiv:hep-ph/0702143 [HEP-PH].

[226] C. Burgess, M. Pospelov, and T. ter Veldhuis, "The Minimal model of nonbaryonic dark matter: A Singlet scalar," *Nucl.Phys.* **B619** (2001) 709–728, arXiv:hep-ph/0011335 [hep-ph].

[227] B. Patt and F. Wilczek, "Higgs-field portal into hidden sectors," arXiv:hep-ph/0605188 [hep-ph].

[228] A. Djouadi, O. Lebedev, Y. Mambrini, and J. Quevillon, "Implications of LHC searches for Higgs–portal dark matter," *Phys.Lett.* **B709** (2012) 65–69, arXiv:1112.3299 [hep-ph].

[229] A. Djouadi, A. Falkowski, Y. Mambrini, and J. Quevillon, "Direct Detection of Higgs-Portal Dark Matter at the LHC," *Eur.Phys.J.* **C73** (2013) 2455, arXiv:1205.3169 [hep-ph].

[230] C. Englert, J. Jaeckel, V. Khoze, and M. Spannowsky, "Emergence of the Electroweak Scale through the Higgs Portal," *JHEP* **1304** (2013) 060, arXiv:1301.4224 [hep-ph].

[231] **ATLAS** Collaboration, G. Aad *et al.*, "Search for Invisible Decays of a Higgs Boson Produced in Association with a Z Boson in ATLAS," *Phys.Rev.Lett.* **112** (2014) 201802, arXiv:1402.3244 [hep-ex].

[232] **CMS** Collaboration, S. Chatrchyan *et al.*, "Search for invisible decays of Higgs bosons in the vector boson fusion and associated ZH production modes," *Eur.Phys.J.* **C74** (2014) no. 8, 2980, arXiv:1404.1344 [hep-ex].

[233] Z. Chacko, Y. Cui, and S. Hong, "Exploring a Dark Sector Through the Higgs Portal at a Lepton Collider," *Phys.Lett.* **B732** (2014) 75–80, arXiv:1311.3306 [hep-ph].

[234] M. Endo and Y. Takaesu, "Heavy WIMP through Higgs portal at the LHC," arXiv:1407.6882 [hep-ph].

[235] L. Carpenter, A. DiFranzo, M. Mulhearn, C. Shimmin, S. Tulin, *et al.*, "Mono-Higgs-boson: A new collider probe of dark matter," *Phys.Rev.* **D89** (2014) no. 7, 075017, arXiv:1312.2592 [hep-ph].

[236] D. Curtin, P. Meade, and C.-T. Yu, "Testing Electroweak Baryogenesis with Future Colliders," arXiv:1409.0005 [hep-ph].

[237] N. Zhou, Z. Khechadoorian, D. Whiteson, and T. M. Tait, "Bounds on Invisible Higgs boson Decays from $t\bar{t}H$ Production," arXiv:1408.0011 [hep-ph].

[238] C. Englert and M. McCullough, "Modified Higgs Sectors and NLO Associated Production," *JHEP* **1307** (2013) 168, arXiv:1303.1526 [hep-ph].

[239] N. Craig, C. Englert, and M. McCullough, "New Probe of Naturalness," *Phys.Rev.Lett.* **111** (2013) no. 12, 121803, arXiv:1305.5251 [hep-ph].

[240] S. Dawson, A. Gritsan, H. Logan, J. Qian, C. Tully, *et al.*, "Working Group Report: Higgs Boson," arXiv:1310.8361 [hep-ex].

[241] V. Kuzmin, V. Rubakov, and M. Shaposhnikov, "On the Anomalous Electroweak Baryon Number Nonconservation in the Early Universe," *Phys.Lett.* **B155** (1985) 36.

[242] S. Weinberg, "Gauge and Global Symmetries at High Temperature," *Phys.Rev.* **D9** (1974) 3357–3378.

[243] M. Quiros, "Finite temperature field theory and phase transitions," arXiv:hep-ph/9901312 [hep-ph].

[244] M. Dine, P. Huet, J. Singleton, Robert L., and L. Susskind, "Creating the baryon asymmetry at the electroweak phase transition," *Phys.Lett.* **B257** (1991) 351–356.

[245] G. W. Anderson and L. J. Hall, "The Electroweak phase transition and baryogenesis," *Phys.Rev.* **D45** (1992) 2685–2698.

[246] M. Dine, R. G. Leigh, P. Y. Huet, A. D. Linde, and D. A. Linde, "Towards the theory of the electroweak phase transition," *Phys.Rev.* **D46** (1992) 550–571, arXiv:hep-ph/9203203 [hep-ph].

[247] A. G. Cohen, D. Kaplan, and A. Nelson, "Progress in electroweak baryogenesis," *Ann.Rev.Nucl.Part.Sci.* **43** (1993) 27–70, arXiv:hep-ph/9302210 [hep-ph].

[248] V. Rubakov and M. Shaposhnikov, "Electroweak baryon number nonconservation in the early universe and in high-energy collisions," *Usp.Fiz.Nauk* **166** (1996) 493–537, arXiv:hep-ph/9603208 [hep-ph].

[249] M. Trodden, "Electroweak baryogenesis," *Rev.Mod.Phys.* **71** (1999) 1463–1500, arXiv:hep-ph/9803479 [hep-ph].

[250] H. H. Patel and M. J. Ramsey-Musolf, "Baryon Washout, Electroweak Phase Transition, and Perturbation Theory," *JHEP* **1107** (2011) 029, arXiv:1101.4665 [hep-ph].

[251] J. Espinosa and M. Quiros, "The Electroweak phase transition with a singlet," *Phys.Lett.* **B305** (1993) 98–105, arXiv:hep-ph/9301285 [hep-ph].

[252] M. S. Carena, A. Megevand, M. Quiros, and C. E. Wagner, "Electroweak baryogenesis and new TeV fermions," *Nucl.Phys.* **B716** (2005) 319–351, arXiv:hep-ph/0410352 [hep-ph].

[253] S. Ham and S. Oh, "Electroweak phase transition and Higgs self-couplings in the two-Higgs-doublet model," arXiv:hep-ph/0502116 [hep-ph].

[254] S. Profumo, M. J. Ramsey-Musolf, and G. Shaughnessy, "Singlet Higgs phenomenology and the electroweak phase transition," *JHEP* **0708** (2007) 010, arXiv:0705.2425 [hep-ph].

[255] M. Carena, G. Nardini, M. Quiros, and C. Wagner, "The Baryogenesis Window in the MSSM," *Nucl.Phys.* **B812** (2009) 243–263, arXiv:0809.3760 [hep-ph].

[256] T. Cohen and A. Pierce, "Electroweak Baryogenesis and Colored Scalars," *Phys.Rev.* **D85** (2012) 033006, arXiv:1110.0482 [hep-ph].

[257] D. Curtin, P. Jaiswal, and P. Meade, "Excluding Electroweak Baryogenesis in the MSSM," *JHEP* **1208** (2012) 005, arXiv:1203.2932 [hep-ph].

[258] C. Grojean, G. Servant, and J. D. Wells, "First-order electroweak phase transition in the standard model with a low cutoff," *Phys.Rev.* **D71** (2005) 036001, arXiv:hep-ph/0407019 [hep-ph].

[259] S. Profumo, M. J. Ramsey-Musolf, C. L. Wainwright, and P. Winslow, "Singlet-Catalyzed Electroweak Phase Transitions and Precision Higgs Studies," arXiv:1407.5342 [hep-ph].

[260] A. Katz and M. Perelstein, "Higgs Couplings and Electroweak Phase Transition," *JHEP* **1407** (2014) 108, arXiv:1401.1827 [hep-ph].

[261] J. R. Espinosa and M. Quiros, "Novel Effects in Electroweak Breaking from a Hidden Sector," *Phys.Rev.* **D76** (2007) 076004, arXiv:hep-ph/0701145 [hep-ph].

[262] A. Noble and M. Perelstein, "Higgs self-coupling as a probe of electroweak phase transition," *Phys.Rev.* **D78** (2008) 063518, arXiv:0711.3018 [hep-ph].

[263] J. R. Espinosa, T. Konstandin, and F. Riva, "Strong Electroweak Phase Transitions in the Standard Model with a Singlet," *Nucl.Phys.* **B854** (2012) 592–630, arXiv:1107.5441 [hep-ph].

[264] J. M. Cline and K. Kainulainen, "Electroweak baryogenesis and dark matter from a singlet Higgs," *JCAP* **1301** (2013) 012, arXiv:1210.4196 [hep-ph].

[265] D. J. Chung, A. J. Long, and L.-T. Wang, "125 GeV Higgs boson and electroweak phase transition model classes," *Phys.Rev.* **D87** (2013) no. 2, 023509, arXiv:1209.1819 [hep-ph].

[266] J. M. Cline, K. Kainulainen, P. Scott, and C. Weniger, "Update on scalar singlet dark matter," *Phys.Rev.* **D88** (2013) 055025, arXiv:1306.4710 [hep-ph].

[267] K. Fuyuto and E. Senaha, "Improved sphaleron decoupling condition and the Higgs coupling constants in the real singlet-extended standard model," *Phys.Rev.* **D90** (2014) no. 1, 015015, arXiv:1406.0433 [hep-ph].

[268] H. Davoudiasl, R. Kitano, T. Li, and H. Murayama, "The New minimal standard model," *Phys.Lett.* **B609** (2005) 117–123, arXiv:hep-ph/0405097 [hep-ph].

[269] **LUX Collaboration** Collaboration, D. Akerib *et al.*, "First results from the LUX dark matter experiment at the Sanford Underground Research Facility," *Phys.Rev.Lett.* **112** (2014) no. 9, 091303, arXiv:1310.8214 [astro-ph.CO].

[270] P. Junnarkar and A. Walker-Loud, "Scalar strange content of the nucleon from lattice QCD," *Phys.Rev.* **D87** (2013) no. 11, 114510, arXiv:1301.1114 [hep-lat].

[271] P. Agrawal, B. Batell, P. J. Fox, and R. Harnik, "WIMPs at the Galactic Center," arXiv:1411.2592 [hep-ph].

[272] N. Craig, S. Knapen, and P. Longhi, "Neutral Naturalness from the Orbifold Higgs," arXiv:1410.6808 [hep-ph].

[273] S. Chang, L. J. Hall, and N. Weiner, "A Supersymmetric twin Higgs," *Phys.Rev.* **D75** (2007) 035009, arXiv:hep-ph/0604076 [hep-ph].

[274] N. Craig and K. Howe, "Doubling down on naturalness with a supersymmetric twin Higgs," *JHEP* **1403** (2014) 140, arXiv:1312.1341 [hep-ph].

[275] M. R. Buckley, D. Feld, and D. Goncalves, "Scalar Simplified Models for Dark Matter," arXiv:1410.6497 [hep-ph].

[276] P. Harris, V. V. Khoze, M. Spannowsky, and C. Williams, "Constraining Dark Sectors at Colliders: Beyond the Effective Theory Approach," arXiv:1411.0535 [hep-ph].

[277] R. K. Ellis, I. Hinchliffe, M. Soldate, and J. van der Bij, "Higgs Decay to tau+ tau-: A Possible Signature of Intermediate Mass Higgs Bosons at the SSC," *Nucl.Phys.* **B297** (1988) 221.

[278] S. Dawson, "Radiative corrections to Higgs boson production," *Nucl.Phys.* **B359** (1991) 283–300.

[279] T. Hahn, "Generating Feynman diagrams and amplitudes with FeynArts 3," *Comput.Phys.Commun.* **140** (2001) 418–431, arXiv:hep-ph/0012260 [hep-ph].

[280] T. Hahn and M. Perez-Victoria, "Automatized one loop calculations in four-dimensions and D-dimensions," *Comput.Phys.Commun.* **118** (1999) 153–165, arXiv:hep-ph/9807565 [hep-ph].

[281] **CMS Collaboration** Collaboration, V. Khachatryan *et al.*, "Search for dark matter, extra dimensions, and unparticles in monojet events in proton-proton collisions at $\sqrt{s} = 8$ TeV," arXiv:1408.3583 [hep-ex].

[282] Y. Bai, H.-C. Cheng, J. Gallicchio, and J. Gu, "Stop the Top Background of the Stop Search," *JHEP* **1207** (2012) 110, arXiv:1203.4813 [hep-ph].

[283] M. Cacciari and G. P. Salam, "Pileup subtraction using jet areas," *Phys.Lett.* **B659** (2008) 119–126, arXiv:0707.1378 [hep-ph].

[284] D. Krohn, M. D. Schwartz, M. Low, and L.-T. Wang, "Jet Cleansing: Pileup Removal at High Luminosity," *Phys.Rev.* **D90** (2014) 065020, arXiv:1309.4777 [hep-ph].

[285] P. Berta, M. Spousta, D. W. Miller, and R. Leitner, "Particle-level pileup subtraction for jets and jet shapes," *JHEP* **1406** (2014) 092, arXiv:1403.3108 [hep-ex].